UNIVERSIDADE FEDERAL DE MINAS GERAIS
INSTITUTO DE GEOCIÊNCIAS
PROGRAMA DE PÓS-GRADUAÇÃO EM GEOLOGIA

Daniel Andrade Miranda

GRAPHITE SCHISTS, KHONDALITES, METAGRANITES AND META-OPHIOLITES FROM ITAPECERICA (MG-BRAZIL): RECORDS OF RHYACIAN-OROSIRIAN OROGENY IN SOUTHERN SÃO FRANCISCO CRATON

Nº 49

BELO HORIZONTE
DATA (07/07/2020)

UNIVERSIDADE FEDERAL DE MINAS GERAIS
INSTITUTO DE GEOCIÊNCIAS
PROGRAMA DE PÓS-GRADUAÇÃO EM GEOLOGIA

GRAPHITE SCHISTS, KHONDALITES, METAGRANITES AND META-OPHIOLITES FROM ITAPECERICA (MG-BRAZIL): RECORDS OF RHYACIAN-OROSIRIAN OROGENY IN SOUTHERN SÃO FRANCISCO CRATON

DANIEL ANDRADE MIRANDA

Programa de Pós-Graduação em Geologia

Versão final

BELO HORIZONTE
2020

UNIVERSIDADE FEDERAL DE MINAS GERAIS
INSTITUTO DE GEOCIÊNCIAS
PROGRAMA DE PÓS-GRADUAÇÃO EM GEOLOGIA

GRAPHITE SCHISTS, KHONDALITES, METAGRANITES AND META-OPHIOLITES FROM ITAPECERICA (MG-BRAZIL): RECORDS OF RHYACIAN-OROSIRIAN OROGENY IN SOUTHERN SÃO FRANCISCO CRATON

DANIEL ANDRADE MIRANDA

Orientador: Prof. Dr. Alexandre de Oliveira Chaves

Tese ampresentada ao Programa de Pós-Graduação em Geologia do Instituto de Geociências da Universidade Federal de Minas Gerais como requisito parcial à obtenção do título de Doutor em Geociências.

BELO HORIZONTE
2020

M672g 2020

Miranda, Daniel Andrade.
Graphite schists, khondalites, metagranites and meta-ophiolites from Itapecerica (MG-Brazil) [manuscrito] : records of rhyacian-orosirian orogeny in Southern São Francisco Craton / Daniel Andrade Miranda. – 2020.
120 f., enc.: il. (principalmente color.)

Orientador: Alexandre de Oliveira Chaves.
Tese (doutorado) – Universidade Federal de Minas Gerais, Instituto de Geociências, 2020.
Área de concentração: Geologia Regional.
Inclui bibliografias.
Inclui apêndices.

1. Petrologia – Itapecerica (MG) – Teses. 2. Geoquímica – Itapecerica (MG) – Teses. 3. Metamorfismo (Geologia) – Teses. 4. Alteração hidrotermal – Teses. 5. Tempo geológico – Teses. I. Chaves, Alexandre de Oliveira. II. Universidade Federal de Minas Gerais. Instituto de Geociências. III. Título.

CDU: 552(815.1)

Ficha catalográfica elaborada por Graciane Aparecida de Paula – CRB6 3404

UNIVERSIDADE FEDERAL DE MINAS GERAIS

PROGRAMA DE PÓS-GRADUAÇÃO EM GEOLOGIA

FOLHA DE APROVAÇÃO

GRAPHITE SCHISTS, KHONDALITES, METAGRANITES AND META-OPHIOLITES FROM ITAPECERICA (MG-BRAZIL): RECORDS OF RHYACIAN-OROSIRIAN OROGENY IN SOUTHERN SÃO FRANCISCO CRATON

DANIEL ANDRADE MIRANDA

Tese submetida à Banca Examinadora designada pelo Colegiado do Programa de Pós-Graduação em GEOLOGIA, como requisito para obtenção do grau de Doutor em GEOLOGIA, área de concentração GEOLOGIA REGIONAL.

Aprovada em 07 de julho de 2020, pela banca constituída pelos membros:

Prof. Alexandre de Oliveira Chaves - Orientador
UFMG

Prof. Edgar Batista de Medeiros Júnior
UFOP

Prof. Jorge Geraldo Roncato Júnior
UFMG

Profa. Rubia Ribeiro Viana
UFVJM

Prof. Stefano Albino Zincone
UFOP

Belo Horizonte, 7 de julho de 2020.

AGRADECIMENTOS

Gostaria de agradecer a Universidade Federal de Minas Gerais e ao Programa de Pós-Graduação em Geologia, pela oportunidade e pelos estudos.

À CAPES pela bolsa de estudos, a FAPEMIG pelo suporte através do projeto APQ-00654-16 e ao projeto de pesquisa do orientador: Registros de Subducção e Colisão Paleoproterozóica no interior do Cráton São Francisco Meridional. Que contribuiram para a realização desta tese.

Ao meu orientador Alexandre de Oliveira Chaves, por me aturar mais quarto anos após o mestrado e continuar com a mesma dedicação e empenho em ensinar e pesquisar.

A minha família e aos familiares que sempre me incentivaram e me apoiaram. As minhas avós, Zina e Rita, temos um doutor na familha.

A minha esposa Maritza pelo incondicional apoio e companheirismo por mais de 14 anos. Eu te amo.

Aos amigos da Geologia, em especial ao grupo da pós-graduação, que ajudaram a tornar esta etapa mais divertida. Em especial ao Marcinho, Salomão e Zangão os forasteiros…

Aos professores do curso, pelos ensinamentos e experiências passadas que contribuíram para a minha formação profissional e pessoal.

Ao pessoal da Nacional de Grafite, em especial ao Hamilton, Lairton e Gilson que nos receberam muito bem e disponibilizaram parte do tempo para nos acompanhar em campo.

Enfim, a todos aqueles que contribuíram de maneira direta ou indiretamente para que esse trabalho fosse realizado, meus sinceros agradecimentos.

RESUMO

A sucessão supracrustal de Itapecerica no Sul do Cráton São Francisco, ao redor de Itapecerica (MG), revela-se em anomalias geofísicas elípticas contendo, nas suas porções internas, sillimanita-cordierita-granada-biotita gnaisse (khondalito) com registro anatético, quartzito, grafita xisto e formação ferrífera bandada, cujos protólitos são de bacia oceânica com idades no contexto da orogenia Riaciano-Orosiriana. Com composições mistas de pelito a grauvaca e acúmulo de matéria orgânica, parte dos sedimentos originais são proveniente da erosão de diferentes fontes de ambiente de margem continental ativa. Rochas metaultramáficas e anfibolitos com afinidade toleítica e assinatura E-MORB ocorrem associados a esta sucessão, sugerindo se tratarem de fragmentos meta-ofiolíticos. Durante o pico do metamorfismo, a matéria orgânica se transformou em grafita ($\delta^{13}C$ -21,23 a -27,89 ‰) em torno de 729 ºC e os sedimentos aluminosos se transformaram em khondalito a 715-772 ºC e 5,5-7,5 kbar há 2090 ± 26 Ma (U-Th-Pb_T em monazita). Essas condições representam a transição da fácies anfibolito para granulito, nas quais o khondalito e o anfibolito sofreram anatexia durante colisão continental com espessamento crustal seguido de exumação tectônica e geraram o metagranito Água Rasa da parte externa das anomalias ($\varepsilon Nd_{(t)}$ -0,5 a -2,7 e $^{87}Sr/^{86}Sr_{(t)}$ 1,04 a 1,08) há 2077 ± 24 Ma (U-Th-Pb_T em monazita). O estágio descompressivo pós-pico decorrente do colapso do orógeno disparou processos hidrotermais com percolação de fluidos C-O-H, recristalizando a grafita em torno de 611 ºC. O processo de descompressão continuou gerando o metagranito Água Rasa entre 1941 ± 23 Ma (U-Th-Pb_T em monazita) e 1934 ± 74 Ma (zircão U-Pb), processo este também detectado no khondalito há 1937 ± 32 Ma (U-Th-Pb_T em monazita) a partir do *reset* do sistema U-Th-Pb da monazita durante o colapso orogênico. Uma possível zona de sutura na região de Itapecerica/Cláudio formada pela colisão entre os complexos Divinópolis e Campo Belo/Bonfim durante a orogenia Riaciano-Orosiriana, envolvendo a bacia oceânica de Itapecerica com prolongamento pela Zona de Cisalhamento de Cláudio em direçãoàBacia Minas, é um cenário geológico sugestivo para a região investigada. As semelhanças entre as rochas khondalíticas deste estudo e as do Norte da China sugerem que o Cráton São Francisco-Congo estava próximo ao Cráton do Norte da China no supercontinente Columbia durante o período de 2.1-1.9 Ga.

Palavras-chave: Grafita; Khondalito; Metagranito; Anfibolito; Metaperidotito; Ofiolito; Petrologia; Geoquímica; Geocronologia; trajetória P-T-t; Metamorfismo; Hidrotermalismo; Proveniência; Anatexia; Cráton São Francisco.

ABSTRACT

The Itapecerica supracrustal succession in the southern São Francisco Craton, around Itapecerica (MG), appear as elliptical geophysical anomalies containing, in their internal portions, sillimanite-cordierite-garnet-biotite gneiss (khondalite) with anatectic record, quartzite, graphite schist and banded iron formation, whose protoliths from oceanic basin have ages in the context of the Rhyacian-Orosirian orogeny. With mixed pelite to wacke compositions and organic matter accumulation, part of the original sediments comes from the erosion of different sources of an active continental margin setting. Metaultramafic rocks and amphibolites wtih tholeiitic affinity and E-MORB signature occur associated to this succession, suggesting to be meta-ophiolitic fragments. During metamorphic peak, the organic matter became graphite ($\delta^{13}C$ -21.23 to -27.89 ‰) around 729 ºC and the aluminous sediments became khondalite at 715–772 ºC and 5.5–7.5 kbar around 2090 ± 26 Ma (monazite U-Th-Pb_T). These conditions represent the transition of amphibolite to granulite facies in which the khondalite and amphibolite underwent anatexis during continental collision with crustal thickning followed by tectonic exgumation to generated the Água Rasa metagranite of the external part of the anomalies ($\varepsilon Nd_{(t)}$ -0.5 to -2.7 and $^{87}Sr/^{86}Sr_{(t)}$ 1.04 to 1.08) at 2077 ± 24 Ma (monazite U-Th-Pb_T). The post-peak decompressional stage due to orogen collapse triggered hydrothermal processes with percolation of C-O-H fluids, leading to the graphite recrystallization around 611 ºC. The decompression process proceeded generating the Água Rasa metagranite between 1941±23 Ma (monazite U-Th-Pb_T) and 1934±74 Ma (zircon U-Pb). This process is also recorded in the khondalite at 1937 ± 32 Ma (monazite U-Th-Pb_T) from the resetting of the monazite U-Th-Pb system during the orogenic collapse. A possible suture zone in the Itapecerica/Cláudio region formed by the collision between Divinópolis and Campo Belo/Bonfim complexes during the Rhyacian-Orosirian orogeny, involving the Itapecerica oceanic basin alongside Cláudio Shear Zoneand forward to Minas Basin, is a suggestive geological setting of the investigated region. Similarities between the khondalite rocks of this study and of the North China suggest that the São Francisco-Congo Craton was near the North China Craton in the supercontinent Columbia for the 2.1–1.9 Ga period.

Keywords: Graphite; Khondalite; Metagranite; Amphibolite; Metaperidotite; Ophiolite; Petrology; Geochemistry; Geochronology; P-T-t path; Metamorphism; Hydrothermalism; Provenance; Anatexis; São Francisco Craton.

SUMMARY

INTRODUCTION

The southern part of São Francisco Craton (SFC) (Fig. 1) consists of Archean crust (3.2–2.6 Ga) composed mainly of granite-gneisses (Farina et al. 2015; Teixeira et al. 2017), greenstone belts (Rio das Velhas Supergroup), Paleoproterozoic clastic-chemical metasedimentary rocks (including the banded iron formations of the Quadrilatero Ferrifero (QF) mining district from Minas Supergroup), and Neoproterozoic pelitic-carbonate sedimentary rocks from Bambuí Group (Teixeira et al. 2017).

The study area is located in the southern SFC, where Archean metamorphic complexes occur (Fig. 1). The Divinópolis complex is composed predominantly of greyish TTG (tonalitic-trondhjemitic-granodioritic) orthogneisses with variable migmatization and Campo Belo/Bonfim complex has tonalitic-granodioritic composition with instrusions of 2790–2610 Ma granitoids and minor occurrence of metaultramafic-mafic rocks (Fernandes and Carneiro 2000; Oliveira 2004; Romano et al. 2013; Campello et al. 2015; Farina et al. 2015). The Archean Candeias Gneiss is part of the Campo Belo complex and is essentially greenish granulitic gneisses with granodioritic (charnoenderbites) to granitic (charnockites) composition and variable migmatization (Oliveira 2004; Carneiro et al. 2007).

The Paleoproterozoic Itapecerica Gneiss is here interpreted as formed by crustal reworking of the Divinópolis complex and Paleoproterozoic supracrustal sequences during Rhyacian-Orosirian Orogeny. According to Carneiro et al. (2007), it is a locally migmatized pinkish gneiss with peraluminous affinity and shows granitic to granodioritic composition. The 2.04 Ga Kinawa migmatite of the Itapecerica Metamorphic Complex (Carvalho et al. 2017) is an example of reworked crust, in which ~2.7 Ga metagranodiorites of the Campo Belo/Bonfim Metamorphic Complex were partially melted in the Cláudio Shear Zone (CSZ) during the Paleoproterozoic.

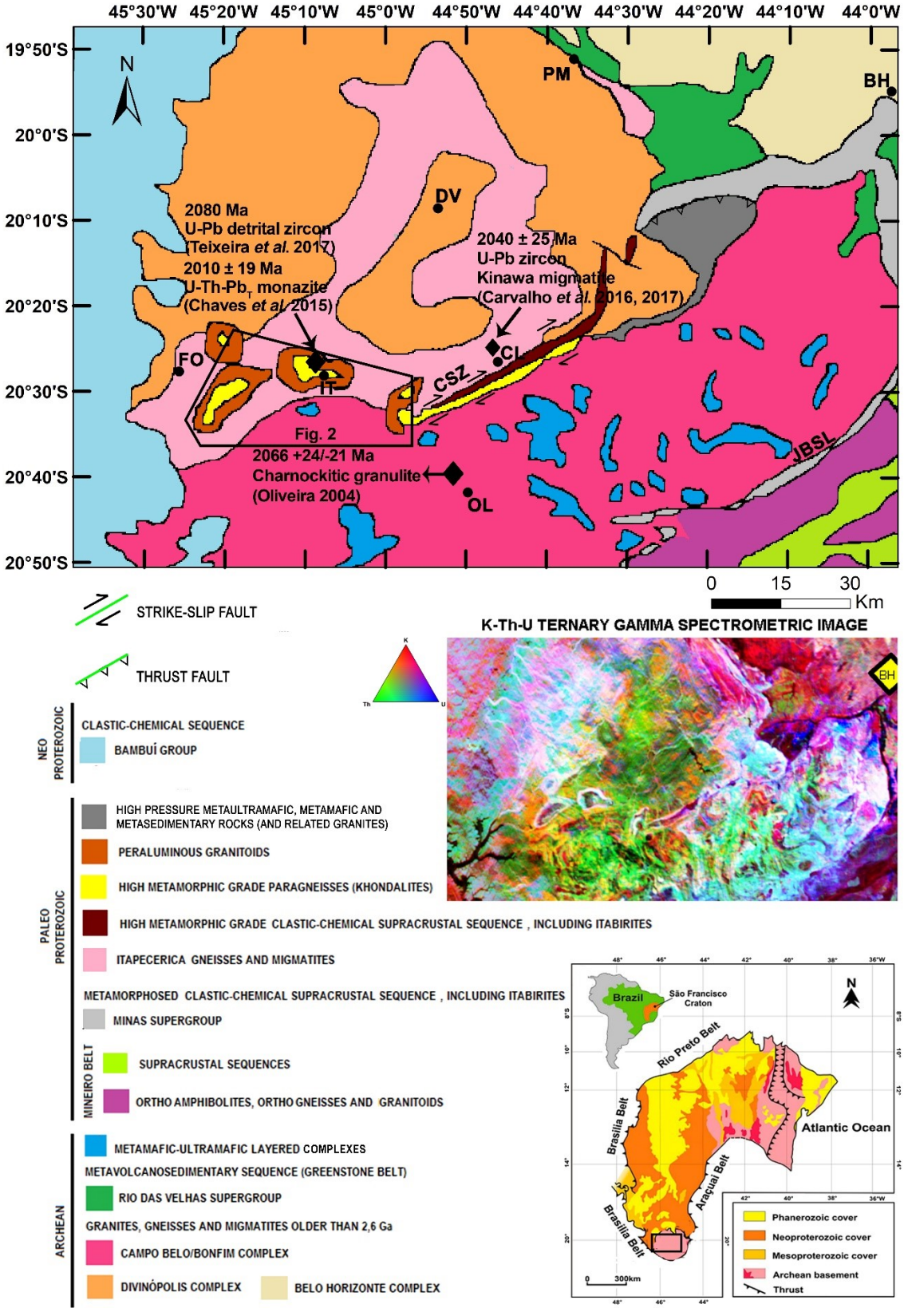

Figure 1. Simplified geological map of the southern portion of the São Francisco Craton. Keys: CSZ = Cláudio Shear Zone; JBSL = Jeceaba-Bom Sucesso Lineament. Towns: BH (Belo Horizonte), CL (Cláudio), DV (Divinópolis), FO (Formiga), IT (Itapecerica), OL (Oliveira), PM (Pará de Minas). K-Th-U ternary gamma spectrometric image of the southern São Francisco Craton from CPRM-CODEMIG (2014). Black polygon marks the location of the studied area (Fig. 2).

The Rhyacian-Orosirian orogeny amalgamated arquean nucleus and different continental to oceanic arcs that collided to form the proto-SFC (Aguilar et al. 2017; Moreira et al. 2018). It is related to the deformation of the Minas Supergroup, to the accretion of juvenile crust that formed the Mineiro Belt to the southeast (Noce et al. 1998; Ávila et al. 2014; Teixeira et al. 2015) and was responsible for extensive reworking of terranes located at the margins of the craton (Noce et al. 2007).

From the data generated by the Aerogeophysical Survey Program of the Minas Gerais Government (Lasa 2001), elliptical geophysical anomalies were observed in the region of Itapecerica (MG) (Fig. 2A), as indicated by Ruy et al. (2006) and Zacchi et al. (2007). Campello et al. (2015) carried out the geological mapping of the region and became possible to associate the geophysical anomalies to the Itapecerica unit, described by the authors at NW of the homonymous city. This unit was divided by these authors in the subunits Supracrustal Sequence and Metagranite, structured as follows: the outer part of the anomaly corresponds to the Metagranite and the internal portions correspond to the supracrustal sequence, with graphite occurrences. Representing the second largest graphite mine in Brazil, the *Nacional de Grafite* Company has mined high-quality natural flake graphite ores in the region since 1939.

The Itapecerica metasedimentary rocks essentially consist of khondalite paragneiss and minor lenticular graphite schist that is interlayered with quartzite bands (partly ferruginous with laminar graphite) and locally marble rocks. In particular, the khondalite exhibits compositional layering and local anatexis and may contain thin graphite films (Carneiro et al. 2007; Campello et al. 2015). The Itapecerica metasedimentary rocks went through of amphibolite to granulite facies metamorphic conditions (Chaves et al. 2015) and are strongly deformed (Teixeira et al. 2017). In the surroundings are reported the occurrence of banded iron formation (BIF). Teixeira et al. (2017) conducted isotopic studies on the Itapecerica graphite-rich supracrustal succession and the detrital zircon analyses in paragneiss indicated a maximum deposition age of 2080 Ma and a metamorphic overprint on granulite facies of 2069 ± 84 Ma (Fig. 2). Chaves et al. (2015) previously reported monazite electron microprobe chemical data in the paragneisses that yielded a U-Th-Pb_T mean age of 2010 ± 19 Ma.

The outer part of the elliptical geophysical anomalies corresponds to the The Água

Rasa Metagranite (Miranda et al. 2020) while the internal portion is the Itapecerica graphite-rich supracrustal succession. Amphibolite (metamafic) and meta-ultramafic bodies occur together with the metasedimentary rocks inside the elliptical geophysical anomalies (Fig. 2B).

The lack of published data on the origin of graphite deposits in the region, due to their economical importance, the lack of data about the metamorphism conditions and age of these rocks, and doubts on the origin of the metagranite surrounding the elliptical geophysical anomalies have motivated the development of this thesis.

This thesis is composed, in addition to the introduction and final comments, of three scientific articles.

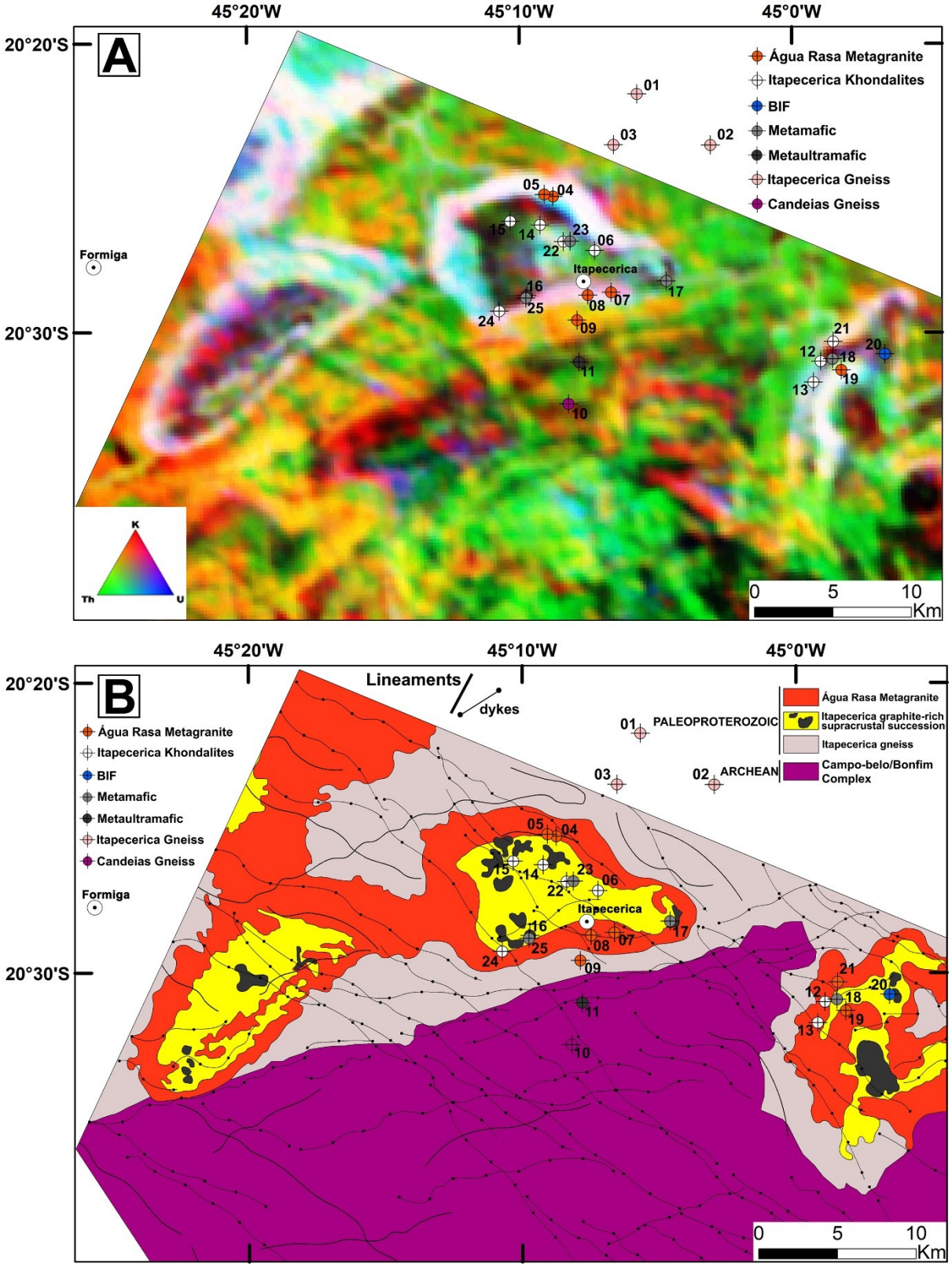

Figure 2. (A) Gammaespectrometry K-Th-U map map showing the elliptical anomalies that guided sampling sites. (B) Simplified geological map of the study area with sampling sites. Map adapted from Ruy et al. (2006) and Zacchi et al. (2007) over high-density magnetic and gamma ray spectrometric data. Amphibolite bodies are shown in black.

The first paper - ***Origin and thermometry of graphites from Itapecerica supracrustal succession of the southern Sao Francisco Craton by C isotopes, X-ray diffraction and Raman spectroscopy*** – is published in the International Geology Review with DOI: https://doi.org/10.1080/00206814.2018.1564073, the second paper - ***Paleoproterozoic khondalites in Brazil: a case study of metamorphism and anatexis in khondalites from Itapecerica supracrustal succession of the southern São Francisco Craton*** – is published in the International Geology Review with DOI: https://doi.org/10.1080/00206814.2020.1716273, and the third paper - ***Itapecerica metamafic-ultramafic rocks with E-MORB signature: ophiolitic remnants of the Rhyacian-Orosirian orogeny in southern São Francisco craton?*** – will be submitted to a scientific journal.

The three articles, in accordance with the requirements of the respective scientific journals, have formatting, numbering of items and independent figures, and they do not follow the general order of this volume.

The first article discusses the origin of the organic matter that formed the graphite, the types of graphite ore found, and an attempt to find the temperature formation of types of graphite. It also suggests the tectonic model that includes the formation of the supracrustal sequence.

In the second article, geochemistry, dating and geothermobarometry techniques were used in the khondalitic unit of the supracrustal sequence in order to find the conditions of temperature, pressure and the age of metamorphism of this sequence. And geochemistry and dating were also used to find the age of crystallization/metamorphism of the metagranite and its relationship with the supracrustal sequence.

And in the third article, the occurrence of metaultramafic bodies and amphibolites with E-MORB affinity associated with the supracrustal sequence indicates that this sequence was an oceanic basin and these metamafic-ultramafic rocks may represent ophiolitic remnants.

ARTICLE I - Origin and thermometry of graphites from Itapecerica supracrustal succession of the southern Sao Francisco Craton by C isotopes, X-ray diffraction and Raman spectroscopy

Daniel Andrade Miranda[a,*], Alexandre de Oliveira Chaves[a], Marcos Santos Campello[a], Sérgio Luís Lima de Moraes Ramos[b].

a Geology Department –Institute of Geosciences – Federal University of Minas Gerais (IGC-UFMG). Av. Antônio Carlos, 6627, Belo Horizonte – MG, CEP 31270-901.

b Technological Center of Nanomaterials - Federal University of Minas Gerais (CTnano-UFMG).

Published in periodic International Geology Review.

DOI: https://doi.org/10.1080/00206814.2018.1564073

ABSTRACT

In the mines of the Nacional de Grafite Company around Itapecerica (MG), located in the southern Sao Francisco Craton, occurs a supracrustal succession of high-grade metamorphic rocks including quartzite, garnet-biotite gneiss and graphite schist formed in the Paleoproterozoic (2.0 Ga). During metamorphic processes, organic matter was progressively transformed into graphite. From four graphite samples of three different mines (two samples from high-grade metamorphic graphite schist and two generated by hydrothermal recrystallization of the graphite schist), the origin and formation temperature of this mineral was obtained by C isotopes, X-ray diffraction (XRD) and Raman spectroscopy. The values of $\delta^{13}C$ range between −21.23 and −27.89 ‰, indicating that the source of the graphite was a primitive biogenic carbon material. High-grade metamorphic graphites show average temperatures around 729 ºC, while hydrothermal recrystallizated graphites (vein-graphites) show temperatures around 611 ºC by XRD, which correspond to granulite- to amphibolite facies conditions. The hydrothermal process with percolation of C-O-H fluids lead to a decreasing in the crystal size along stacking direction ($Lc_{(002)}$) when compared with the previously formed high-grade metamorphism graphites. An update of the current tectonic model about the collisional process during Rhyacian-Orosirian orogeny in the Sao Francisco Craton is proposed to insert the formation of the Itapecerica graphite-rich metasedimentary sequence.

Keywords: Graphite; X-ray diffraction; Raman spectroscopy; Carbon isotopes; Southern Sao Francisco Craton; Metamorphism; Hydrothermalism.

Introduction

The stable form of carbon at the earth's surface and in the crust is graphite, however well crystallized graphite is considered relatively rare. Instead, a poorly crystallized, disordered material commonly called “graphitic carbon” occurs in other geological settings (Buseck and Beyssac 2014).

Graphite occurs in metamorphic rocks although it can appear also in other geological

settings. Luque et al. (1998) and Gálvez et al. (2013) distinguish four types of naturally occurring graphite: (i) graphite formed through metamorphism of biogenic carbonaceous material, (ii) mantle-derived graphite, (iii) graphite formed as precipitates from aqueous fluids, (iv) graphite formed through reduction of carbonates.

According to Kwiecińska and Petersen (2004), the metamorphism transforms natural carbonaceous materials (CM) to anthracite, meta-anthracite, semi-graphite and graphite. Graphitization describes the transformation of disordered or partly ordered, non-crystalline carbon-bearing material into pure-carbon, end-member crystalline graphite. It occurs in a variety of terrestrial and extraterrestrial settings. Incomplete graphitization, which is common, results in materials having different degrees of crystallographic order arising from various combinations of temperature, pressure, kinetics, and, in some cases, fluid activity. Beyssac et al. (2002) and Buseck and Beyssac (2014) argue that the process of graphitization is progressive and irreversible.

Graphitic carbon occurs mainly in rocks from orogenic belts and in metasedimentary rocks in old cratons, although it occurs in rocks of all ages. Some graphite deposits in the world are listed on table 1.

Table 1. Graphite deposits in the world.

Graphite deposits	Age	T/P estimates	References
Wanni, Sri Lanka (Vein Graphite)	Neoproterozoic	~1.100ºC / ~12 kbar	Luque et al. (2014)
Runds, Austria	Paleozoic	~700-800ºC / ~7-9 kbar	Petrakakis (1986, 1997)
Hubei, China	Meso-Neoarchean	~700ºC / ~4 kbar	Geng (2015)
Skaland, Norway	Archaean–Proterozoic	~750ºC / ~4 kbar	Bergh et al. (2010, 2012); Henderson and Kendrick (2003)
Balama, Mozambique	Neoproterozoic	~600-850ºC / ~6-10 kbar	Feneyrol et al. (2013)
Southern Madagaskar	Archean-Proterozoic	~700-800ºC / ~8-11 kbar	Jöns and Schenk, (2011), Parthasarathy et al. (2006)
Zavalje, Ukraine	Archean	-	Dagelaysky (1997), Zagnitko et al. (2013)
Toledo, Spain	Paleozoic	~800ºC / ~4-6 kbar	Martín-Méndez et al. (2016)
Thodupuzha-Kanjirappally, India	Neoproterozoic	~700ºC / ~6-9 kbar	Baiju et al. (2005)
Kasuga, Japan	Mesozoic	~650ºC / ~3-4 kbar	Wada et al. (1994)
Sao Francisco Craton, Brazil	Paleoproterozoic	~750ºC/ ~4 kbar	Chaves et al (2015); Miranda et al (This paper)
Ribeira Orogen, Brazil	Neoproterozoic	~750ºC/ ~4 kbar	Pereira et al (2016)

Graphite usually has a biogenic origin and is formed by the change of organic CM in sediments due to metamorphic processes. The $\delta^{13}C$ isotopic composition of graphitic carbon

falls in the range of –35 to –20‰, largely inherited from its biological precursors (Buseck and Beyssac 2014).

Wintsch et al. (1981) demonstrated that the temperature, duration of metamorphism and presence of metamorphic fluids, with some influence from the lithology and original texture of organic tissues, mainly controls the graphitization process of CM. Tagiri and Oba (1986) suggested that graphitization depends on metamorphic temperature and oxygen fugacity, but not on metamorphic pressure to a great extent. The transformation process of CM to graphite offers an opportunity to use Raman spectroscopy geothermometry to quantify metamorphic temperatures from low-grade metamorphism (~330 °C) to high-grade metamorphism (~600 °C) (Beyssac et al. 2002). In order to investigate metamorphic conditions higher than 600 ºC, it's also possible to use X-ray diffraction (XRD) geothermometry (Wada et al. 1994) based on graphitization degree (Tagiri 1981) as the upper limit of temperature previewed by the equation for pelitic rocks of Wada et al. (1994), as well as in Baiju et al. (2005), is around 700ºC. Both methods can provide valuable information on the physical (metamorphic) conditions of graphite formation (Luque et al. 1998).

The aim of this study is to characterize two different forms of graphite found in mines of Itapecerica (Minas Gerais - MG), from which two samples are from high-grade metamorphic graphite schist and two generated by hydrothermal recrystallization of the graphite schist. The characterization has been made by investigating the graphite crystallinity using X-ray diffractometry (XRD) and Raman spectroscopy, while the study of the carbon source have been performed by C isotope analysis. The differences between the forms of graphite are discussed and the crystallization temperature found for graphite is compared to the temperature estimated by mineral paragenesis of host rocks. In addition, an update of the current tectonic model about the collisional process during Rhyacian-Orosirian orogeny in the Sao Francisco Craton is proposed to insert the formation of the Itapecerica graphite-rich metasedimentary sequence.

Geological Setting

The southern part of Sao Francisco Craton (Fig. 1) comprises Meso- to Neoarchean granite-greenstone terrains, Paleoproterozoic clastic-chemical metasedimentary rocks (including Itabirites of Quadrilatero Ferrifero) from Minas Supergroup, and Neoproterozoic pelitic-carbonate sedimentary rocks from Bambuí Group (Teixeira et al. 2017a).

The Archean portion is characterized by TTG (tonalite-trondhjemite-granodiorite) suites, greenstone belts formed between 3.20-2.90 Ga, granitoid plutons generated by partial melting of older material (2.79–2.70 Ga) (Teixeira et al. 2017a), mafic-ultramafic intrusions (Noce et al. 1998) and granitoid rocks emplaced later at 2.61 Ga (Farina et al. 2015). The two main distinctive supracrustal units of the region are the Neoarchean greenstone belt sequence (Rio das Velhas Supergroup, 2.77–2.73 Ga) and the Early Paleoproterozoic Minas Supergroup (Moreira et al. 2016; Teixeira et al. 2017a). The topmost unit of the Minas Supergroup, the Sabará Group, contains detrital zircons as young as 2125 ± 4 Ma (Machado et al. 1996). This youngest grains reflect the tectonic inversion and closure of passive margin basins (Alkmim and Noce 2006). Locally, the Itacolomi molasse-type sediments (1.96 Ga) cover the continental crust of the Quadrilatero Ferrifero (QF) (Machado et al. 1996). The Minas Supergroup extends to the SW of the QF, as portrayed by the correlative strata along the Jeceaba-Bom Sucesso lineament (Neri et al. 2013).

The Claudio Shear Zone (CSZ) is a NE-trending Paleoproterozoic structure that transects the country rocks to the north of the Jeceaba-Bom Sucesso lineament. The CSZ records high deformation strain with dextral strike-slip motion (Carvalho et al. 2016, 2017). Crustal reworking along CSZ produced partial melting at ~730 ºC and 5-6 kbar, generating the Kinawa migmatite that have U-Pb zircon ages of 2048 ± 25 and 2034 ± 32 Ma (Carvalho et al. 2016, 2017). These ages are identical to that of nearby charnockitic granulite (2066 +24/-18Ma) that defines the peak of prograde granulite facies metamorphism over the Archean crust (Oliveira 2004) (Fig 1). Nearby ~2.05 Ga quartz ± plagioclase ± sillimanite ± garnet schist and quartz ± sillimanite ± garnet ± biotite quartzite also confirms the regional high-grade metamorphic conditions (Teixeira et al. 2017b).

To the south of the Jeceaba-Bom Sucesso lineament, there is an extensive NE-trending orogenic domain, referred to as Mineiro belt (Fig. 1) (Teixeira and Figueiredo 1991; Ávila et al. 2014; Barbosa et al. 2015). The Mineiro belt (Teixeira et al. 2015) resulted from long-term arc development, represented by progressively younger plutonic complexes and coeval metavolcanic-sedimentary successions (Seixas et al. 2012, 2013; Ávila et al. 2014; Teixeira et al. 2015; Barbosa et al. 2015).

The collisional process also triggered deformation and NNW-verging thrusting over the Minas Supergroup strata in the Jeceaba-Bom Sucesso lineament, along with the

aforementioned fold-and-thrust belt in the crustal section of the QF. Teixeira et al. (2017b) consider that the ~2.05 Ga high-grade metamorphism and partial melting of the Archean basement are also collisional markers of the Mineiro belt. In a broader scale, all these overprinting features highlight the tectonic expression of the Minas orogeny well inward from the ancient foreland.

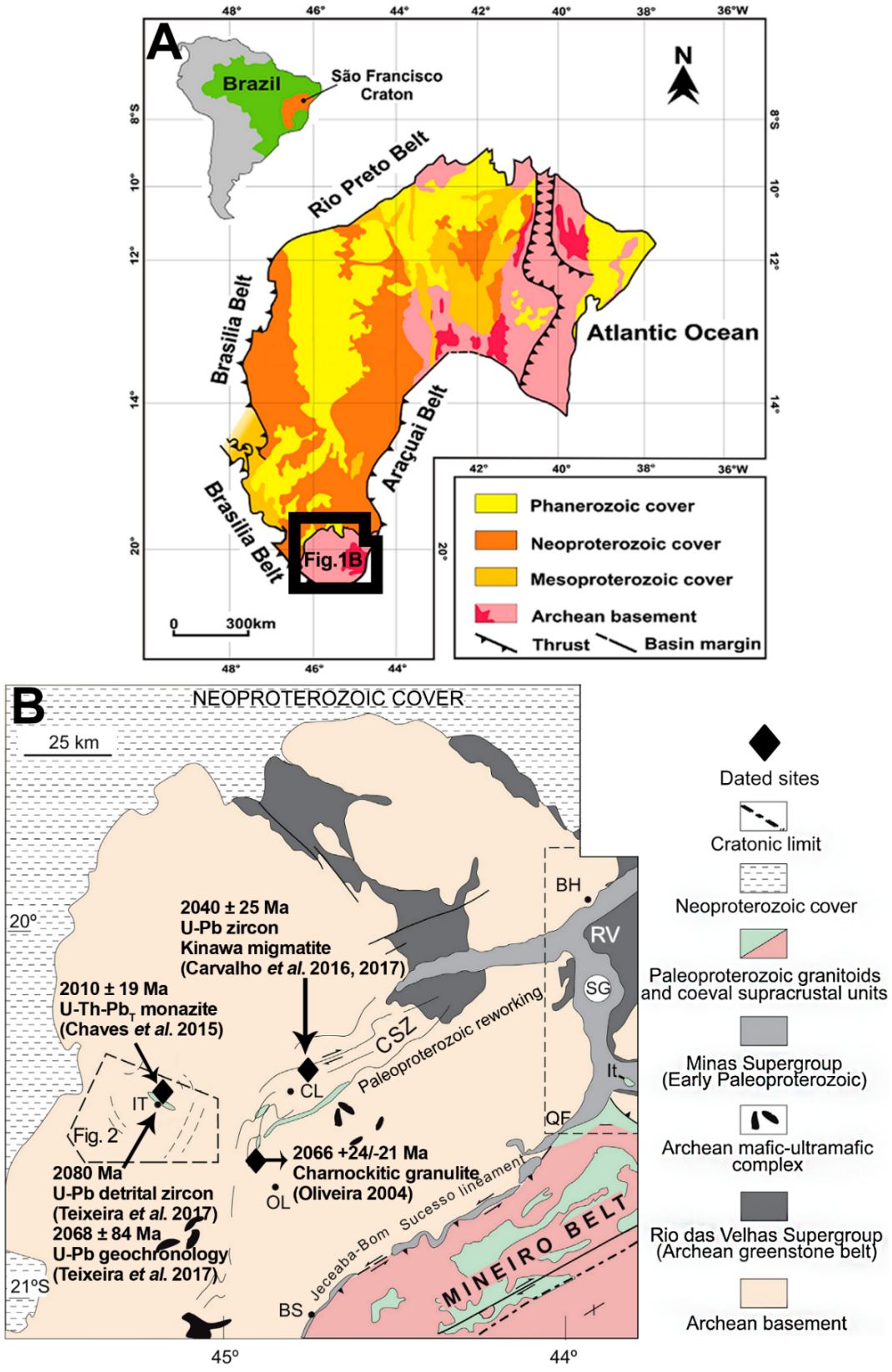

Figure 1. (A) Sao Francisco Craton location . Modified from Drummond et al. (2015). (B) Geological map of the southern portion of the Sao Francisco Craton. Keys: RV = Neoarchean Rio das Velhas Supergroup; SG = Sabará Group (Early Paleoproterozoic Minas Supergroup); It = Itacolomi Group (<1.96 Ga); CSZ = Cláudio Shear Zone; QF = Quadrilátero Ferrifero. Towns: *IT (Itapecerica), CL (Cláudio), OL (Oliveira), BS (Bom Sucesso), BH (Belo Horizonte).* Modified from Teixeira et al. (2017b). Location of the figure 2 is highlighted on (B).

Local Geological Setting

The study area is located at the crystalline basement of the Itapecerica region (Fig. 1). According to Carneiro and Barbosa (2008), the area feature gneiss, granitoids, amphibolites, mafic, ultramafic and charnockitic rocks formed in Mesoarchean. Locally, supracrustal remnants could be correspondent to Archean and/or Paleoproterozoic greenstone belts related to QF. Those rocks were recrystallized under high amphibolite- to granulite facies conditions (Fernandes and Carneiro 2000). Mafic dykes (diabase and amphibolite) of several generation crosscuts these rocks (Chaves 2013) (Fig. 2)*.

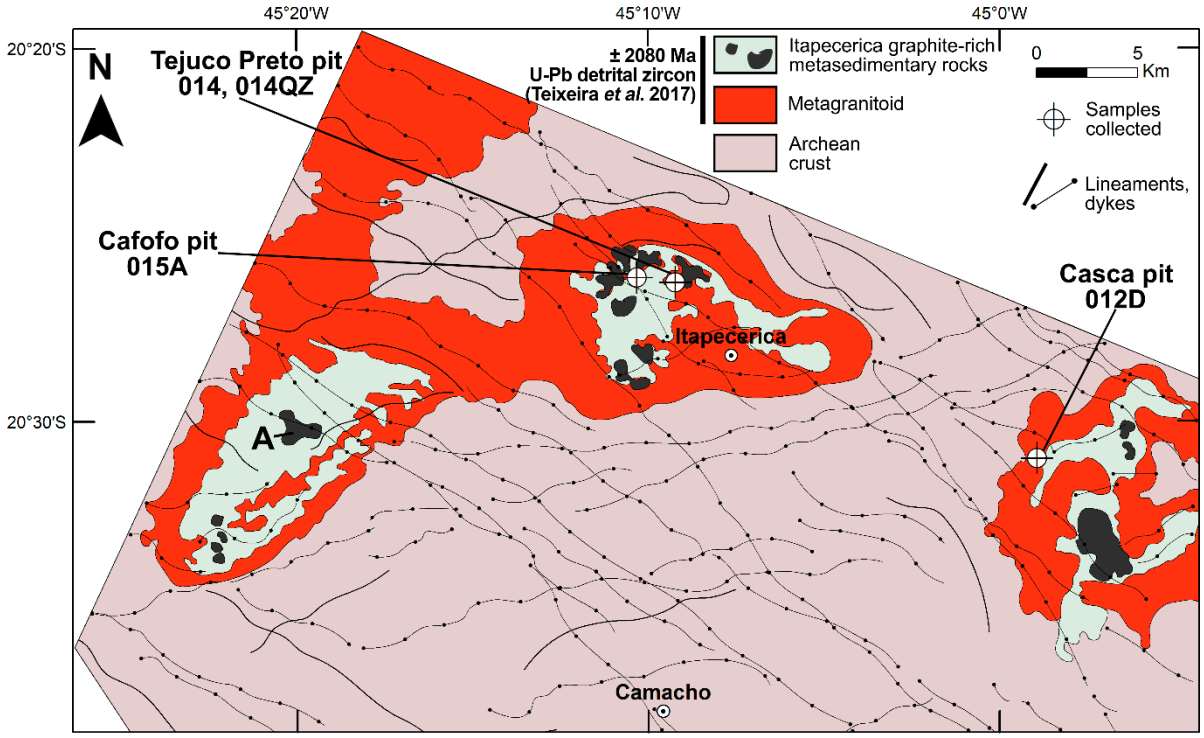

Figure 2. Geological map showing the elliptical shapes, which host the graphite-rich metasedimentary rocks, encircled by the Archean basement. Map built by Ruy et al. (2006) and Zacchi et al. (2007) over high-density magnetic and gamma ray spectrometric data; A = amphibolite. Samples were collected on the three mine pits (Casca, Cafofo and Tejuco Preto). *See explanatory note after Acknowledgments.

Geology of the Itapecerica graphite-rich metasedimentary rocks

From a global geodynamic perspective, khondalite belts represent precursor basins that underwent granulite facies metamorphism because of subduction-collision process, which culminated with the amalgamation of continental fragments (Condie et al. 1992; Faure et al. 1997). The Itapecerica graphite-rich metasedimentary rocks keep a high-grade, khondalite-like mineral paragenesis with cordierite ± sillimanite ± mesopertitic K-feldspar ± garnet ±

graphite (Campello et al. 2015; Chaves et al. 2015; Teixeira et al. 2017b).

The Itapecerica graphite-rich metasedimentary rocks is characterized by garnet- and sillimanite-bearing aluminous gneisses and schists with or without spinel, cordierite and graphite, mainly derived from sedimentary protoliths (Chaves et al. 2015). According to these authors, the garnet-sillimanite-cordierite-K-feldspar paragenesis indicates that these rocks formed under high amphibolite- to granulite facies conditions with temperatures in order of 750-800ºC.

Teixeira et al. (2017b) conducted isotopic studies on the Itapecerica graphite-rich supracrustal succession and the detrital zircon analyses in paragneiss indicated a maximum deposition age of 2080 Ma and a metamorphic overprint on granulite facies of 2069 ± 84 Ma (Fig. 1). Chaves et al. (2015) reported electron microprobe chemical analyses on monazite in paragneisses that yielded a U-Th-Pb_T mean age of 2010 ± 19 Ma (Fig. 1); these ages overlap within error and they can be interpreted as the timing of the conversion of carbonaceous material into graphite in the Itapecerica mines during the high-grade metamorphism.

The elliptical geophysical anomalies (Fig. 2) host the second largest graphite mine in Brazil, is located 20 km west of the Claudio Shear Zone in the town of Itapecerica. The *Nacional de Grafite* Company has mined high-quality natural flake graphite ores since 1939. Flake graphite occurs in high-grade metamorphic rocks worldwide, where it was generated by either fluid deposition or graphitization. Flake-type graphite is found as crystals generally larger than 100 μm and is disseminated in rocks with bulk carbon contents generally in the range 5-40 wt% for commercial viability (Beyssac and Rumble 2014).

The Itapecerica graphite schist is composed of fine- to medium grained graphite, quartz and sillimanite showing granolepidoblastic texture. Graphite is the main component and mark the rock's foliation. Quartz is the second main component, with elongated (ribbons) crystals, which matches the foliation. Sillimanite occurs in variable proportions as fibrous or prismatic habit. In the samples 012D and 015A the graphite films are smaller and scattered in the rock (Fig. 3A, B, C and D), than in the samples 014 and 014QZ, in which the graphite forms larger aggregates (Fig. 3E, F).

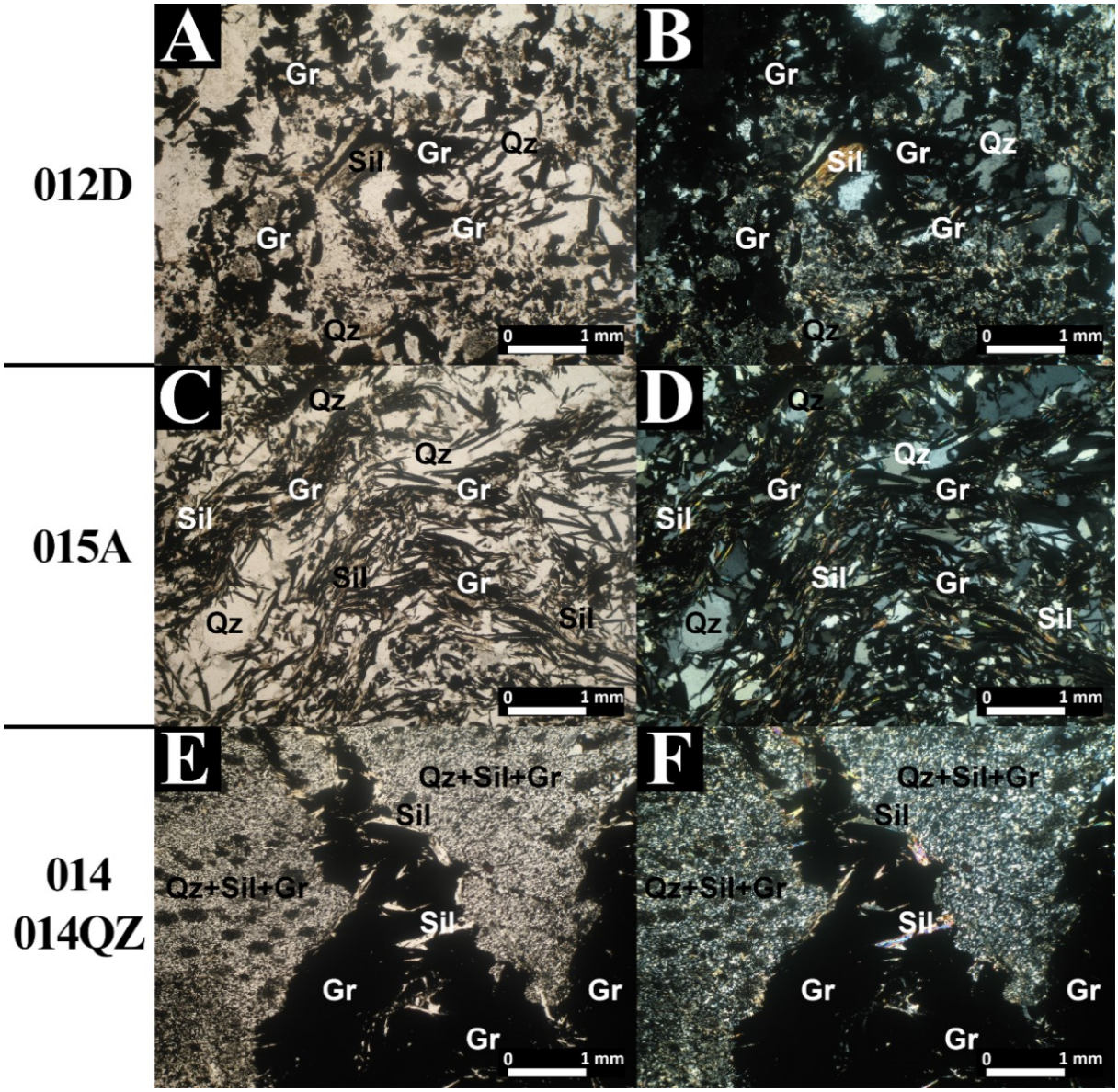

Figure 3. Photomicrographs illustrating graphite textures: (A, C, E) on PPL – Plane Polarized Light; (B, D, F) on XPL – Crossed Polarized Light. Samples 012D and 015A showing the scattered aspect of the graphite inside schist. Samples 014, 014QZ showing large aggregates of graphite. Mineral abbreviations according to Whitney and Evans (2010), Gr - graphite, Sil - sillimanite, Qz - quartz.

Methods and Results

Four samples of graphite from three different mine pits were collected: sample 012D from Casca pit (Fig. 4A, 4B), sample 015A from Cafofo pit (Fig. 4C, 4D) and samples 014 and 014QZ from Tejuco Preto pit (Fig. 4E, 4F). It is important to note that the 014 and 014QZ samples derive from a quartz vein - in this case the graphite is different from the other samples and has the shape of large graphite sheets related to the hydrothermal process that generate the quartz vein (Fig. 4F). Field observations show that the quartz veins are younger than the graphite schist. Consequently, at the moment of emplacement of these veins, the

graphite present in the schist was mobilized by a hydrothermal fluid and precipitated in the form of vein-graphite. Consequently, two samples from high-grade metamorphic graphite schist and two generated by hydrothermal recrystallization of the graphite schist (vein-graphite) were investigated. Raman spectroscopy and XRD analysis were done on all samples and the isotopic ratios $^{13}C/^{12}C$ on the samples 012D, 014 and 015A. Supplementary Table 1 shows the results for XRD and carbon isotope data.

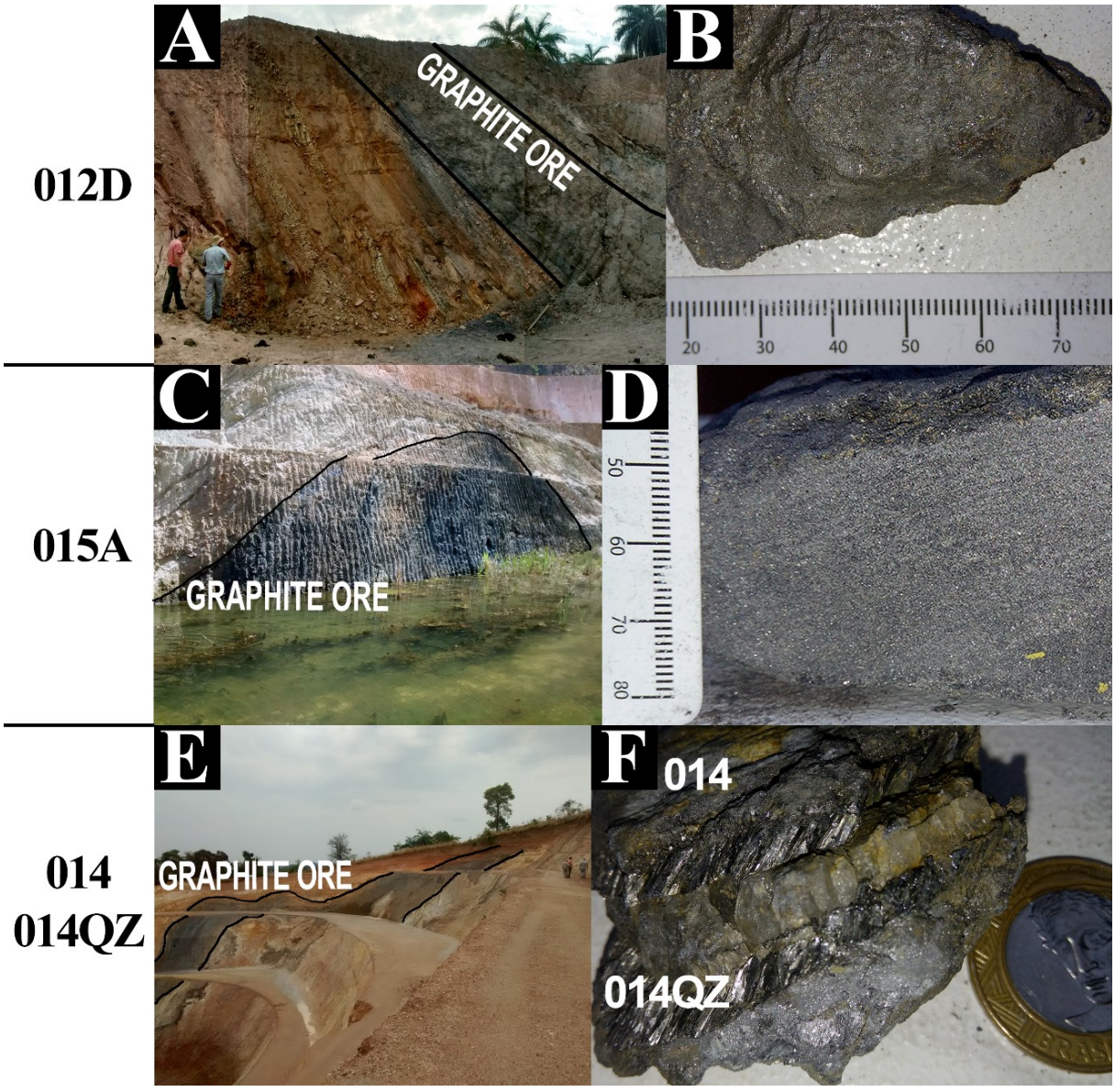

Figure 4. General view of the outcrops where the samples were collected (A, C, E). Macroscopic view of the samples (B, D, F) showing the similarity between samples 012D and 015A and the difference in relation to samples 014 and 014QZ.

Based on Tagiri (1981) the standard deviation of the error of $d_{(002)}$ is ~0.02 over 3.53Å, ~0.01 between 3.53 and 3.36Å and ~0.005 between 3.36 and 3.35Å. The experimental

error of $Lc_{(002)}$ is about 4 percent below 30Å and about 10 percent over 500Å (Tagiri 1981).

Raman spectroscopy

The Raman data were obtained in the Technological Center of Nanomaterials (CTnano) at technological park of Belo Horizonte (MG) – BHTec, using the same methodology proposed in Rantitsch et al. (2016) and the same equipment, a confocal microscope Alpha 300R WITEC (Wissenschaftliche Instrumente und Technologie GmbH®, Ulm, Germany) equipped with a Nd-YAG laser with double frequency (2.49 mW, λ = 532.2 nm). Raman spectra were collected with 50× lens objective, where five scans in the 1000-3200 cm^{-1} spectra (first order = 1000-2000 cm^{-1}; second order = 2200-3200 cm^{-1}) were performed with an acquisition time of 30s.

In each sample five major fields (red, green, blue, white and black) were randomly selected (Fig. 5A). Figure 5B show the analyzed spots (red, green, blue). Figure 5C show the Raman spectra of the three previous spots. The analysis of the spectra focused on the first-order peaks at ~1350 cm^{-1} (D1 band), ~1500 cm^{-1} (D3 band), ~1580 cm^{-1} (G band) and ~1610 cm^{-1} (D2 band) (Fig. 5C).

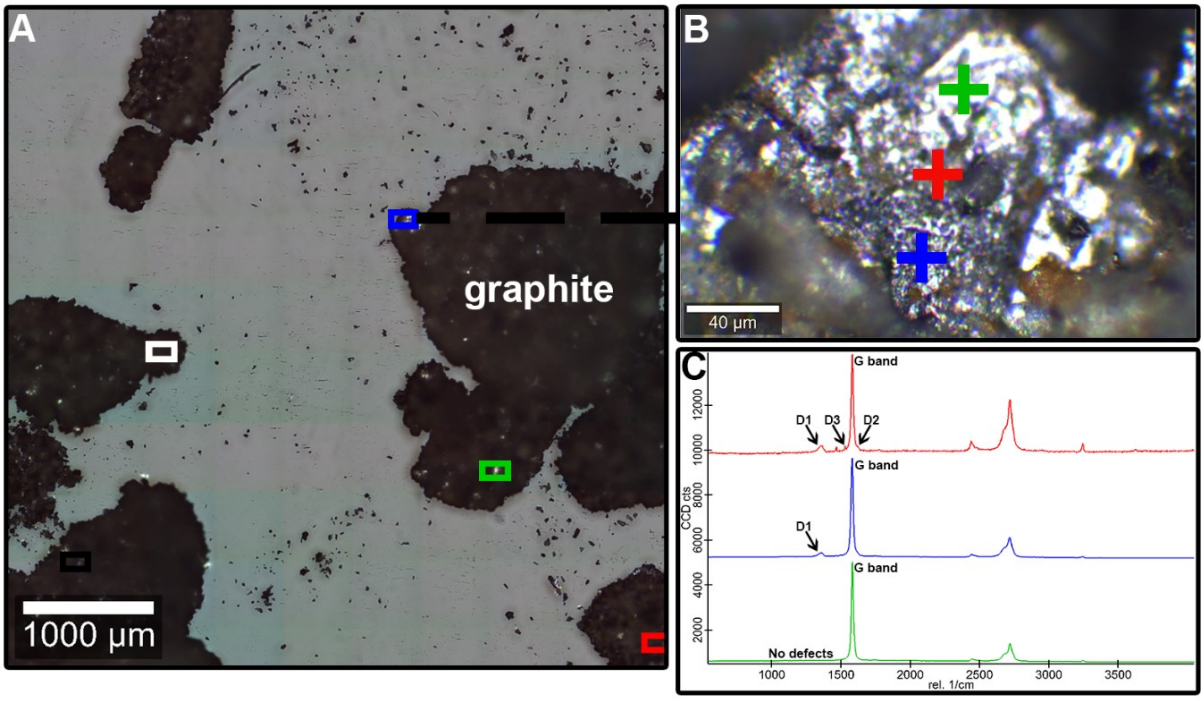

Figure 5. (A) View of a sample in the microscope with five major fields: red; green; blue; white; black. Photomicrograph taken in PPL (B) Zoom of the blue major field with three spots of analysis: red; green; blue. (C) Raman spectra of the spots. Photomicrograph taken in PPL.

The supplementary Table 2 show the results of Raman spectroscopy, R2 ratio and the temperature calculations by the IFORS method (Lünsdorf and Lünsdorf, 2016).

X-ray diffraction

XRD analyzes were performed at the Manoel Teixeira da Costa Research Center (CPMTC-IGC-UFMG, at Belo Horizonte-MG) X-ray Laboratory. X-ray diffraction spectra were recorded with a PANalytical X´Pert PRO diffraction instrument with theta-theta geometry, using a Cu Kα X-ray source (40 kV and 45 mA). The diffraction data were collected with a step size of 0.02° 2θ and a scan step of 0.5 s. To obtain lattice parameters of high accuracy, the diffraction data were fitted by Rietveld methods (Young 1993). The starting parameters for the refinement were identical for each sample and chosen to be as close as possible to realistic values.

The crystal size ($Lc_{(002)}$) along stacking direction (supplementary Table 1) is estimated from the equation below (Baiju et al. 2005):

$$Lc_{(002)} = k\lambda / \beta_{(002)}\cos\theta$$

Where k is the shape constant (0.9), $\beta_{(002)}$ is the full width at half maximum of the peak in radian, λ is the X-ray wavelength in angstroms (1.5406), and θ is the angle of diffraction in radians. Further, the graphitization degree (GD) has been calculated from the equation (Tagiri 1981):

$$GD = \{[d_{(002)} - 3.7]/[\text{Log}\ (Lc_{(002)}/1000)]\}*100$$

In addition, the metamorphism temperature is calculated by the equation for pelitic rocks (Wada et al. 1994):

$$T\ (^{o}C) = 3.2 \times GD + 280$$

The binary plot of $Lc_{(002)}$ vs $d_{(002)}$ shows that samples 014 and 014QZ are on the threshold between “graphite” and “fully ordered graphite” fields while the samples 012D and 015A plot on “fully-ordered graphite” field (Fig. 6A). The plot of temperature vs GD (Fig. 6B) shows higher metamorphic temperature and GD to samples 012D and 015A (related to

high-grade metamorphism) and lower formation temperature and GD to samples 014 and 014QZ (related to hydrothermal recrystallization of the previously formed graphite).

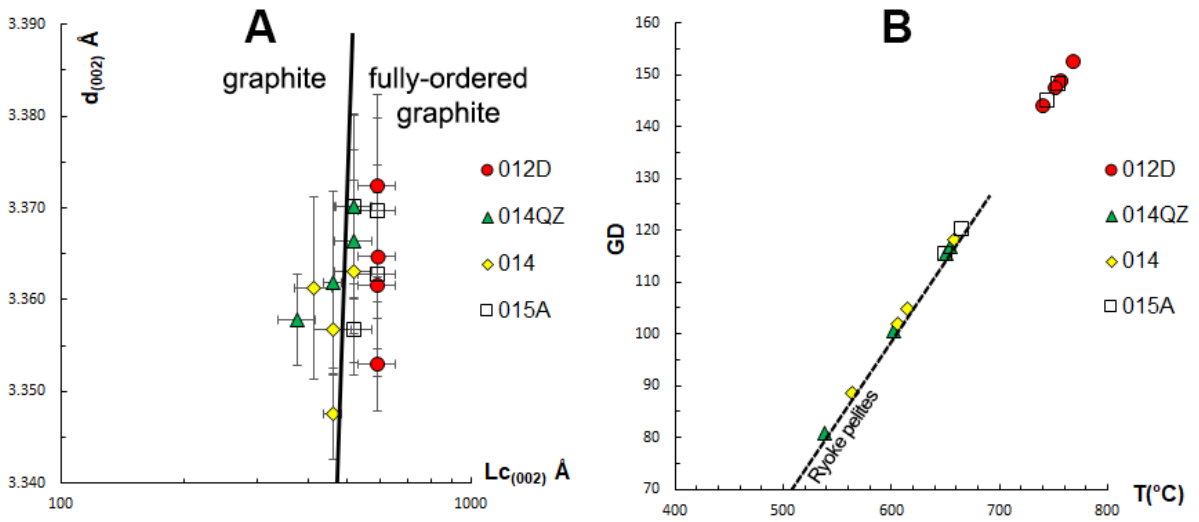

Figure 6. (A) Interplanar spacing $d_{(002)}$ vs crystallite size $Lc_{(002)}$ (Tagiri and Oba 1986). (B) Graphitization degree vs XRD data temperature compared to the linear relationship for Ryoke pelites of Wada et al. (1994).

Carbon isotope analyses

The isotopic ratios of C were obtained on the Stable Isotope Laboratory of Institute of Geosciences (LAIS) of UnB at Brasília in a mass spectrometer DELTA V Plus with auto-sampler. The samples are inserted on tin capsules that are taken to the furnace with O_2 and He flows, the CO_2 released is analyzed using the Flash EA system. The results are exposed on the conventional notation per mil (‰) related to the pattern V-PDB (Vienna-Pee Dee Belemnites). The associated error is 0.05 ‰ for $\delta^{13}C$.

The negative values of the $\delta^{13}C$ range between −21.23 and −27.89 ‰ indicate that the source of the CM was a primitive biogenic carbon material. Therefore, all samples are from group (i) from Luque et al. (1998); Gálvez et al. (2013). However, samples 014 and 014QZ are inserted in the group (iii) after hydrothermal recrystallization of the previously formed graphite.

Discussions

Following Rantitsch et al. (2016), which tried to correlate XRD and Raman data, the supplementary Table 3 show the mean values of these data for further comparison by using studied samples in order to find the formation temperature of the graphite from Itapecerica

supracrustal succession. In these case, by the mineral paragenesis presented in the Itapecerica graphite-rich metasedimentary rocks like garnet, sillimanite, cordierite, K-feldspar and spinel these rocks formed, at least, under high amphibolite- to granulite facies conditions with temperatures in order of 750-800ºC as Chaves et al. (2015).

A significant correlation between the $d_{(002)}$ lattice distance and the width of the Raman G band (Fig. 7A) and also the D1/(G + D1 + D2) area ratio (R2 ratio of Beyssac et al. 2002) (Fig. 7B) are exposed. Metamorphic facies (Beyssac et al. 2002; Rantitsch et al. 2016) and the semi-graphite/graphite separation (Kwiecińska and Petersen 2004; Rantitsch et al. 2016) in the figures 7A and 7B indicate that the graphite from Itapecerica mines was formed during high-grade metamorphism, between amphibolite and granulite facies.

Although G HWHM values put all samples in high amphibolite facies, the figure 7A seems to reveal lower metamorphic conditions acting in the samples 014 and 014QZ, which have the highest G HWHM values (8.77 to 8.81, supplementary Table 3), than in samples 012D and 015A (8.04 to 8.25, supplementary Table 3). These lower metamorphic conditions could be interpreted as a later hydrothermal process responsible to generate samples 014 and 014QZ. The R2 ratio in figure 7B places all the samples in the low granulite facies. This indicates a good relation of the R2 parameter with the graphite formation temperature, as seen on Beyssac et al. (2002); Lünsdorf (2015) and Rantitsch et al. (2016).

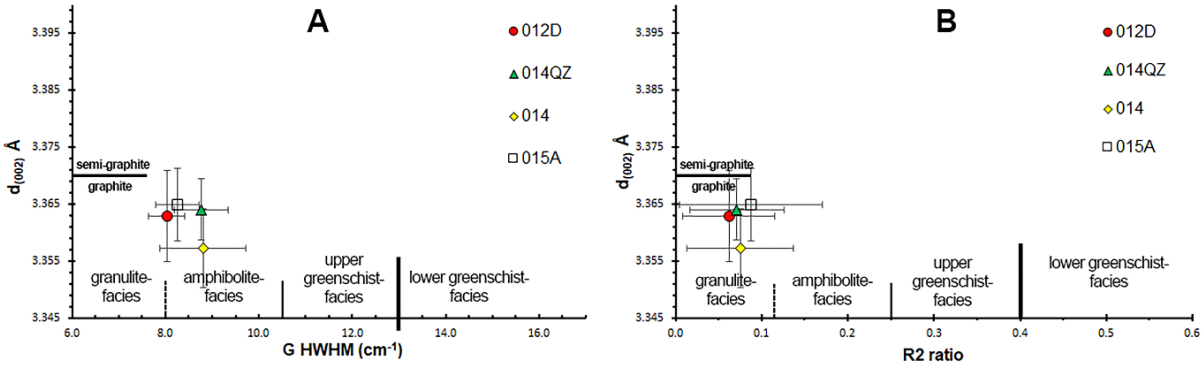

Figure 7. Itapecerica graphites plotted in diagrams from Rantitsch et al. (2016). (A) Half width at half maximum (HWHM) of the G-band versus $d_{(002)}$ lattice distance (Graphite/Semi-graphite at – G HWHM ~ 13.0 and $d_{(002)}$ ~ 3.370). (B) R2 ratio (Beyssac et al. 2002; D1/(G+D1+D2) area ratio) versus $d_{(002)}$ lattice distance (Graphite/Semi-graphite at – R2 ~ 0.4 and $d_{(002)}$ ~ 3.370).

When the average temperature obtained from the Raman data (590 ºC, Supplementary Table 2) and the temperature obtained by the XRD data (Supplementary Table 1) are compared, it becomes clear that the temperature obtained by IFORS method does not

correspond to the metamorphism in granulite facies estimated for the region. This is because the graphite reaches the maximum crystallinity at 600 ºC, forming flake-type graphites. According to Beyssac et al. (2002) and Lünsdorf (2015), around 600 °C all graphite becomes fully ordered and the IFORS method cannot calculate higher temperatures. Yet, if temperatures obtained by Raman and XRD only for the samples 014 and 014QZ are compared, they are relatively similar (584 °C by Raman and 611 °C by XRD). Owing to the similarity between temperature found by Raman and XRD for vein-graphite (014 and 014QZ) samples, the use of the equation for pelitic rocks (Wada et al. 1994) becomes reliable even to vein-graphite samples.

The studied samples represent high-grade metamorphic graphite schist (012D and 015A) and hydrothermal recrystallization of the graphite schist (014 and 014QZ). The XRD data (Supplementary Table 3) for high-grade metamorphism samples show average temperatures around 729 ºC. Although this average matches with that of the metamorphism in granulite facies estimated for the region by the mineral paragenesis of rocks associated with graphite (Chaves et al., 2015), it is important to mention that the value of 729ºC overcome the superior limit around 700ºC previewed by the equation for pelitic rocks of Wada et al. (1994). Samples of high-grade metamorphic conditions in Baiju et al. (2005) support an extrapolation of temperatures above 700 ºC on the equation for pelitic rocks of Wada et al. (1994). The temperatures around 611 ºC for the samples 014 and 014QZ related to hydrothermal process point to a recrystallization of graphite during the percolation by C-O-H fluids. The cooling of the fluid lead to graphite precipitation in the form of vein-graphite. Therefore, the hydrothermal process apparently lead to a decreasing in the crystal size along stacking direction ($Lc_{(002)}$) when compared with the regional metamorphism samples 012D and 015A (Fig. 6A, 6B and Supplementary Table 1).

Regarding tectonic regional activity, Carvalho et al. (2017) have proposed a scenario in which the Archean block is the lower plate and the Mineiro belt is the upper plate. This scenario shows crustal reworking restricted to places where faults were developed or re-activated. These deep faults act as pathways for fluids to access the rocks and cause local partial melting responsible to generate the Kinawa migmatite at collisional stage. The tectonic model of Carvalho et al. (2017) for the collision of the Mineiro belt against the Neoarchean foreland did not include the generation of Itapecerica graphite-rich metasedimentary sequence. Chaves et al. (2015) and Teixeira et al. (2017b) were the first to suggest the

possibility of including this sequence in the tectonic discussion.

During the pre-collisional stage, beyond the Minas Basin, another basin with conditions to accumulate a great amount of organic matter would have been metamorphosed/deformed in the collisional stage. Figure 8 proposes a tectonic model modified from Carvalho et al. (2017) for the formation of the Itapecerica graphite-rich metasedimentary sequence around 2.05 Ga, involving the Paleoproterozoic NE-trending Mineiro orogenic belt and the Claudio Shear Zone. During the pre-collisional stage (2.35 to 2.08 Ga) the carbonaceous materials (CM)-rich sedimentary sequence was deposited over the Sao Francisco paleoplate. Such sequence was involved during the collision stage (2.07 to 2.01 Ga) and the CM transformed into graphite under high-grade metamorphism. Finally, at the post-collisional stage (after 2.01 Ga) there was the collapse of the previously formed orogen accompanied by intense activity of C-O-H hydrothermal fluids, which precipitated the vein-graphite.

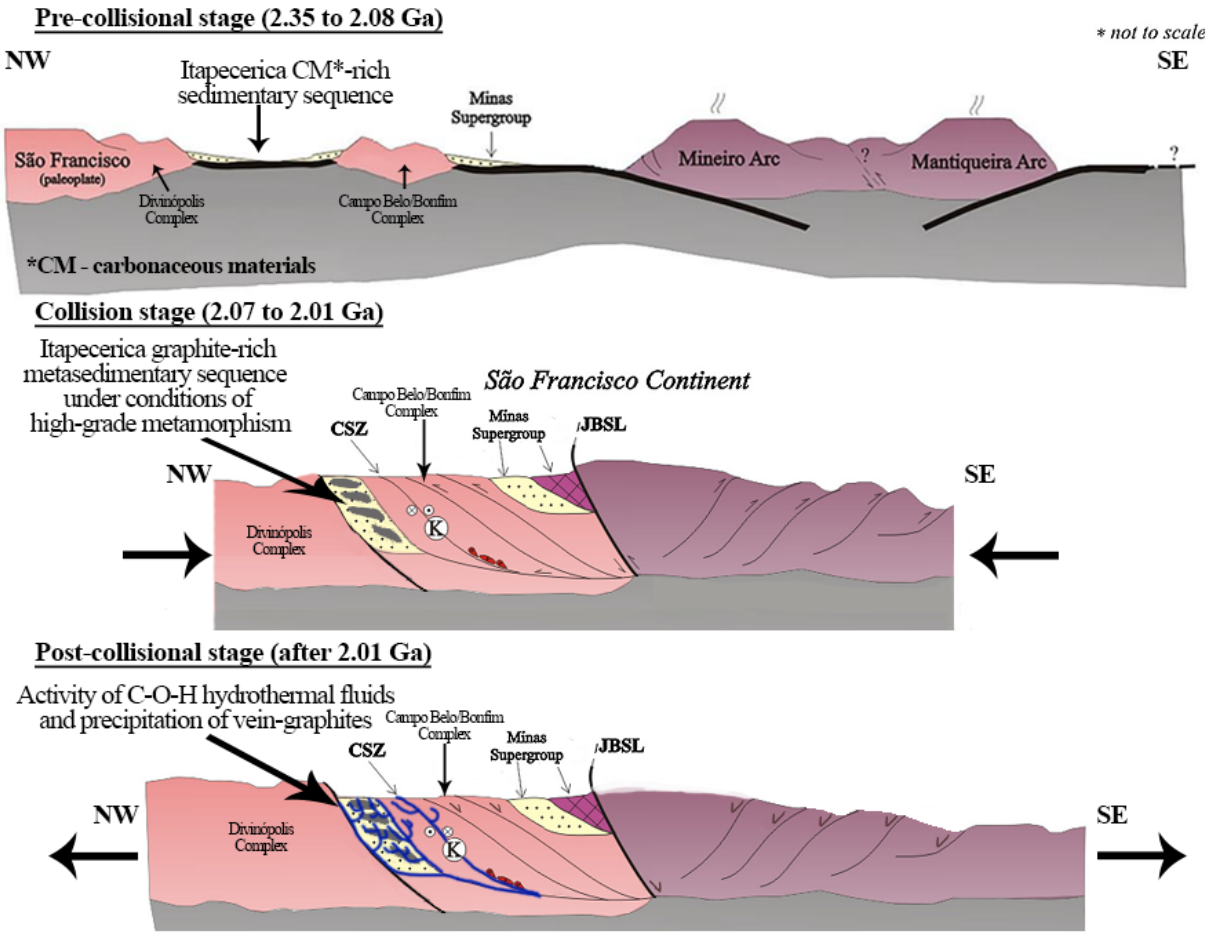

Figure 8. Illustration (adapted from Carvalho et al. 2017) of a tectonic model for the formation of the different types of graphite from the Itapecerica region. (K) Kinawa migmatite. (CSZ) Claudio Shear Zone. (JBSL) Jeceaba-Bom Sucesso lineament.

Conclusions

The $\delta^{13}C$ between −21.23 and −27.89 ‰, indicate that the source of CM is primitive biogenic carbon. Raman and XRD data indicate that all the graphite in the Itapecerica mines are of high crystallinity and have undergone high-grade metamorphism (amphibolite- to granulite facies conditions). High-grade metamorphic graphites that have been preserved from hydrothermalism process show average temperatures around 729 ºC, while hydrothermal recrystallizated graphites (vein-graphites) show temperatures around 611 ºC by XRD. The hydrothermal process with percolation of C-O-H fluids lead to a decreasing in the crystal size along stacking direction ($Lc_{(002)}$) when compared with the previously formed high-grade metamorphism graphites. The update on the current tectonic model for the Rhyacian-Orosirian orogeny in the Sao Francisco craton now includes the Itapecerica graphite-rich metasedimentary basin.

Acknowledgments: We are grateful to the Institute of Geosciences of UFMG that available the CPMTC laboratories, to PhD. Marcos Assunção Pimenta coordinator of the Technological Center of Nanomaterials - (CTnano-UFMG), to the *Nacional de Grafite* Company, the geologist Lairton de Oliveira and geology supervisor Gilson dos Santos. The second author thanks to CNPq the research productivity grant and FAPEMIG for research support through the project APQ-00654-16. This study was financed in part by the Coordenação de Aperfeiçoamento de Pessoal de Nível Superior - Brasil (CAPES) - Finance Code 001".

***Explanatory Note:**

An update to figure 2 of this article was necessary to correspond with the ideas discussed in the subsequent articles of this thesis.

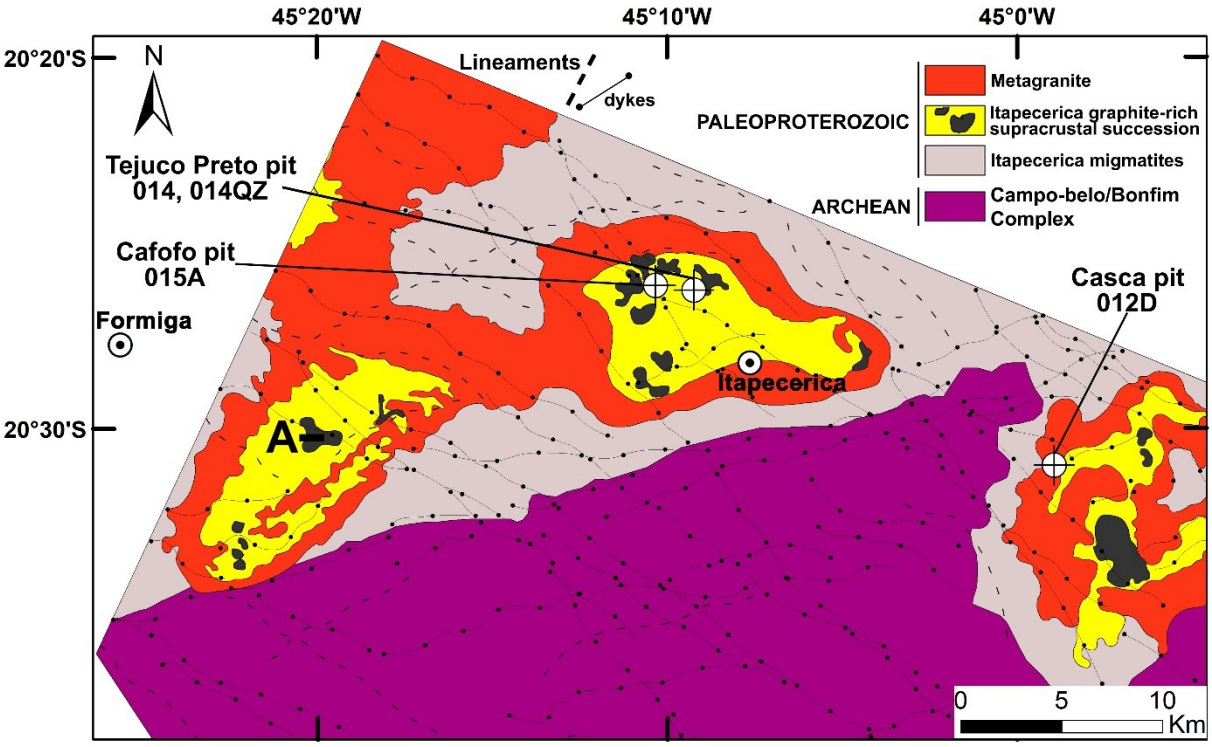

Figure 2. Geological map showing the elliptical shapes, which host the graphite-rich metasedimentary rocks. Map modified from Ruy et al. (2006) and Zacchi et al. (2007) over high-density magnetic and gamma ray spectrometric data; A = amphibolite. Samples were collected on the three mine pits (Casca, Cafofo and Tejuco Preto).

References

Alkmim, F.F., Noce, C.M., 2006, Outline of the geology of Quadrilátero Ferrífero, In: Alkmim, F.F. and Noce, C.M. (eds.) 2006. The Paleoproterozoic Record of the São Francisco Craton. IGCP 509 Field workshop, Bahia and Minas Gerais, Brazil. Field Guide & Abstracts, 114 p., p. 37-73.

Ávila, C.A., Teixeira, W., Bongiolo, E.M., Dussin, I.A., Vieira, T.A.T., 2014, Rhyacian evolution of subvolcanic and metasedimentary rocks of the southern segment of the Mineiro belt, São Francisco Craton, Brazil. Precambrian Res., v. 243, p. 221-251.

Baiju, K.R., Satish-Kumar, M., Kagi, H., Nambiar, C.G., Ravinsankar, M., 2005, Mineralogical characterization of graphite deposits from Thodupuzha-Kanjirappally Belt, Madurai Granulite Block, Southern India. Gond. Res., v. 8, p. 223-230.

Barbosa, N.S., Teixeira, W., Ávila, C.A., Montecinos, P.M., Bongiolo, E.M., 2015, 2.17–2.10 Ga plutonic episodes in the Mineiro belt, São Francisco Craton, Brazil: U-Pb ages, geochemical constraints and tectonics. Precambrian Res., v. 270, p. 204-225.

Bergh, S.G., Kullerud, K., Armitage, P.E.B., Zwaan, K.B., Corfu, F., Ravna, E.J.K., Myhre, P.I., 2010, Neoarchaean to Svecofennian tectono-magmatic evolution of the West Troms Basement Complex. North Norway. Norw. J. Geol., v. 90, p. 21-48.

Bergh, S.G., Corfu, F., Myhre, P.I., Kullerud, K., Armitage, P.E.B., Zwaan, K.B., Ravna, E.K., Holdsworth, R.E., Chattopadhya, A., 2012, Was the Precambrian basement of Western Troms and Lofoten-Vesterålen in Northern Norway linked to the Lewisian of Scotland? A comparison of crustal components, tectonic evolution and amalgamation history, In: Sharkov, E., (eds) Tectonics – Recent Advances. InTech, p. 283-330.

Beyssac, O., Goffé, B., Chopin, C., Rouzaud, J.N., 2002, Raman spectra of carbonaceous material in metasediments: a new geothermometer. J. Metamorph. Geol., v. 20, p. 859-871.

Beyssac, O., Rumble, D., 2014, Graphitic Carbon: A Ubiquitous, Diverse, and Useful Geomaterial. Elements, v. 10, p. 415-420.

Buseck, P.R., Beyssac, O., 2014, From Organic Matter to Graphite: Graphitization. Elements, v. 10, p. 421-426.

Campello, M.S., Vaz, B.B., Oliveira, M.A.S., Ávila, M.A.C., 2015, Relatório e mapa geológicos 1:100.000 da Folha Formiga SF.23-V-B-III. Projeto Fortaleza de Minas, CODEMIG/UFMG. A.C. Pedrosa Soares (coord.). 62 p.

Carneiro, M.A., Barbosa, M.S.C., 2008, Implicações geológicas e tectônicas da interpretação magnetométrica da região de Oliveira, Minas Gerais. Revista Brasileira de Geofísica, v. 26, n. 1, p. 87-98.

Carvalho, B.B., Sawyer, E.W., Janasi, V.A., 2016, Crustal reworking in a shear zone: transformation of metagranite to migmatite. J. Metamorph. Petrol., v. 34, p. 237-264.

Carvalho, B.B., Janasi, V.A., Sawyer, E.W., 2017, Evidence for Paleoproterozoic anatexis and crustal reworking of Archean crust in the São Francisco Craton, Brazil: a dating and isotopic study of the Kinawa migmatite. Precambrian Res., v. 291, p. 98-118.

Chaves, A.O., 2013, Enxames de diques máficos de Minas Gerais – o estado da arte. Geonomos, v. 21, n. 1, p. 29-33.

Chaves, A.O., Campello, M.S., Soares, A.C.P., 2015, Idade U-Th-Pb_T de monazitas do sillimanita-cordierita-granada-biotita gnaisse de Itapecerica (MG) e a atuação da orogenia Riaciano-Orosiriana no interior do Cráton São Francisco Meridional. Geociências, v. 34, n. 3, p. 324-334.

Condie, K., Boryta, M.D., Liu, J., Xianglin Qian, X., 1992, The origin of khondalites: geochemical evidence from the Archean to Early Proterozoic granulite belt in the North China craton. Precambrian Res., v. 59, p. 207-233.

Dagelaysky, V.B., 1997, The Ukrainian Shield, In: Rundkvist, D.V., Gillen, C., eds., Precambrian Ore Deposits of the East European and Siberian Cratons. Elsevier, p. 107-153.

Drummond, J.B.R., Pufahl, P.K., Porto, C.G., Carvalho, M., 2015, Neoproterozoic peritidal phosphorite from the Sete Lagoas Formation (Brazil) and the Precambrian phosphorous cycle. Sedimentology, v. 62, p. 1978-2008.

Farina, F.A., Albert, C., Lana, C., 2015, The Neoarchean transition between medium and high-K granitoids: clues from the Southern São Francisco Craton (Brazil). Precambrian Res., v. 266, p. 375-394.

Faure, M., Trap, P., Lin, W., Monie, P., Bruguier, O., 1997, Polyorogenic evolution of the paleoproterozoic Trans-North China belt, new insights from the Lüliangshan-Hengshan-Wutaishan and Fuping massifs. Episodes, v. 30, p. 1-12.

Feneyrol, J., Giuliani, G., Ohnenstetter, D., Fallick, A.E., Martelat, J.E., Monié, P., Dubessy, J., Rollion-Bard, C., Le Goff, E., Malisa, E., Rakotondrazafy, A., Pardieu, V., Kahn, T., Ichang'i, D., Venance, E., Voarintsoa, N.R., Ranatsenho, M.M., Simonet, C., Omito, E., Nyamai, C., Saul, M., 2013, New aspects and perspectives on tsavorite deposits. Ore Geol. Rev., v.53, p. 1-25.

Fernandes, R.A., Carneiro, M.A.O., 2000, Complexo Metamórfico Campo Belo (Craton São Francisco Meridional): unidades litodêmicas e evolução tectônica. Revista Brasileira de Geociencias, v.30, n. 4, p. 671-678.

Gálvez, M.E., Beyssac, O., Martinez, I., Benzerara, K., Chaduteau, C., Malvosin, B., Malavieille, J., 2013, Graphite formation by carbonate reductionduring subduction. Nat. Geosci., v. 6, p. 473-477.

Geng, Y.S., 2015, Early Precambrian geological signatures in South China Craton. *in* Zhai, M. (eds) Precambrian Geology of China. Springer, p. 207-239.

Henderson, I., Kendrick, M., 2003, Structural controls on graphite mineralisation, Senja. Troms. NGU Report., v. 11, p. 1-111.

Jöns, N., Schenk, V., 2011, The ultrahigh temperature granulites of southern Madagascar in a polymetamorphic context: implications for the amalgamation of the Gondwana supercontinent. Eur. J. Mineral, v. 23, p. 127-156.

Kwiecińska, B., Petersen, H., 2004, Graphite, semi-graphite, natural coke, and natural char classification-ICCP system. Int. J. Coal Geol., v. 57, p. 99-116.

Lünsdorf, N.K., 2015. Geothermometry by Raman Spectroscopy of Dispersed OrganicMatter PhD thesis University of Göttingen (113 p).

Lünsdorf, N.K., Lünsdorf, J.O., 2016, Evaluating Raman spectra of carbonaceous matter by automated, iterative curve-fitting. Int. J. Coal Geol., v. 160-161, p. 51-62.

Luque, F.J., Pasteris, J.D., Wopenka, B., Rodas, M., Barrenechea, J.F., 1998, Natural fluid-deposited graphite: mineralogical characteristics and mechanisms of formation. American Journal of Science, v. 298, p. 471-498.

Luque, F.J., Huizenga, J.-M., Crespo-Feo, E., Wada, H., Ortega, L., Barrenechea, J.F., 2014, Vein graphite deposits: geological settings, origin, and economic significance. Mineral. Deposita, v. 49, p. 261-277.

Machado, N., Schrank, A., Noce, C.M., Gauthier, G., 1996, Ages of detrital zircon from Archean-Paleproterozoic sequences: implications for greenstone belt setting and evolution of a Transamazonian foreland basin in Quadrilátero Ferrífero, southeast Brazil: evidence from zircon ages by laser ablation ICP-MS. Earth Planetary Science Letters, v. 141, p. 259-276.

Martín-Méndez, I., Boixereu, E., Villaseca, C., 2016, Mineralogical and isotopic characterization of graphite deposits from the Anatectic Complex of Toledo, central Spain. Miner Deposita, v. 51, p. 575-590.

Moreira, H., Lana, C., Nalini Jr, H.A., 2016, The detrital zircon record of an Archaean convergent basin in the Southern São Francisco Craton, Brazil. Precambrian Res., v. 275, p. 84-99.

Neri, M.E.N.V., Rosière, C.A., Lana, C.C., 2013, Supergrupo Minas na Serra de Bom Sucesso, extremo sudoeste do Quadrilátero Ferrífero – MG: petrografia, geoquímica e isótopos de U-Pb. Revista Geologia USP Série Científica, v. 13, n. 2, p. 117-202.

Noce, C.M., Machado, N., Teixeira, W., 1998, U-Pb Geochronology of gneisses and granitoids in the Quadrilatero Ferrıfero (Southern São Francisco Craton): age constraints for Archean and Paleoproterozoic magmatism and metamorphism. Revista Brasileira de Geociencias, v. 28, p. 95-102.

Oliveira, A.H., 2004, Evolução tectônica de um fragmento do Cráton São Francisco Meridional com base em aspectos estruturais, geoquímicos (rocha total) e geocronológicos (Rb-Sr, Sm-Nd, Ar-Ar, U-Pb). Tese de Doutoramento. Universidade Federal de Ouro Preto, Brazil, 92p.

Parthasarathy, G., Collins, A.S., Chetty, T.R.K., 2006, Natural graphite from Neoproterozoic psammitic gneiss, Inanalo mountain, southern Madagascar. J. Geol. Soc. India, v. 68, p. 176-180.

Pereira, R.M., Neumann, R., Salomão, M., Guimarães, P.V., Ramos, G.V., Dutra, A.C., Pedroso, E., 2016, Terrenos Khondalíticos: Principais domínios para manganês, grafita, ouro e zinco no estado do Rio de Janeiro e regiões limítrofes. Geonomos, v. 24, n. 1, p. 41-51.

Petrakakis, K., 1986, Metamorphism of high-grade gneisses from the Moldanubian zone, Austria, with particular reference to the garnets. J. Metamorph. Geol., v. 4, p. 323-344.

Petrakakis, K., 1997, Evolution of Moldanubian rocks in Austria: review and synthesis. J. Metamorph. Geol., v. 15, p. 203-222.

Rantitsch, G., Lämmerer, W., Fisslthaler, E., Mitsche, S., Kaltenböck, H., 2016, On the discrimination of semi-graphite and graphite by Raman spectroscopy. International Journal of Coal Geology, v. 159, p. 48-56.

Ruy, A.C., Silva, A.M., Toledo, C.L.B., Souza Filho, C.R., 2006, Uso de dados aerogeofísicos de alta densidade para mapeamento geológico em terrenos altamente intemperizados: o estudo de caso da região de Cláudio, porção sul do Cráton São Francisco. Revista Brasileira de Geofísica, v. 24, n. 4, p. 535-546.

Tagiri, M., 1981, A measurement of the graphitizing degree by the X-ray powder diffractometer. Journal of Mineralogy, Petrology and Economic Geology, v. 76, p. 345-52.

Tagiri, M., Oba, T., 1986, Hydrothermal syntheses of graphite from bituminous coal at 0.5-5 kbar water vapor pressure and 300-600°C. Journal of Mineralogy, Petrology and Economic Geology, v. 81, p. 260-71.

Teixeira, W., Figueiredo, M.C.H., 1991, An outline of Early Proterozoic crustal evolution in the Sãoo Francisco craton, Brazil: a review. Precambrian Res., v. 53, p. 1-22.

Teixeira, W., Ávila, C.A., Dussin, I.A., Corrêa Neto, A.V., Bongiolo, E.M., Santos, J.O.S., Barbosa, N., 2015, Zircon U-Pb-Hf, Nd-Sr constraints and geochemistry of the Resende Costa Orthogneiss and coeval rocks: new clues for a juvenile accretion episode (2.36-2.33 Ga) in the Mineiro belt and its role to the long-lived Minas accretionary orogeny. Precambrian Res., v. 256, p. 148-169.

Teixeira, W., Oliveira, E.P., Marques, L.S., 2017a, The nature and evolution of the Archean Crust of the São Francisco Craton, *in* Heilbron, M., Alkmim, F., Cordani, U.G., eds., São Francisco Craton, Eastern Brasil: tectonic genealogy of a miniature continent, Regional Geology Review Series. Springer-Verlag, p. 29-56.

Teixeira, W., Oliveira, E.P., Peng Peng, Dantas, E.L., Hollanda, M.H.B.M., 2017b, U-Pb geochronology of the 2.0 Ga Itapecerica graphite-rich supracrustal succession in the São Francisco Craton: Tectonic matches with the North China Craton and paleogeographic inferences. Precambrian Research, v. 293, p. 91-111.

Wada, I.H., Tomita, T., Iuchi, K., Ito, M., Morikiyo, T., 1994, Graphitization of carbonaceous matter during metamorphism with reference to carbonate and pelitic rocks of contact and regional metamorphism, Japan. Contrib. Mineral. Petrol., v. 118, p. 217-228.

Whitney, D.L., Evans, B.W., 2010, Abbreviations for names of rock-forming minerals. American Mineralogist, v. 95, n. 1, p.185-187.

Wintsch, R.P., O'connel, A.F., Lansom, B.L., Wiechmann, M.J., 1981, Evidence for the influence off CH4 on the crystallinity of disseminated carbon in greenschist facies rocks, Rhode Island, USA. Contrib. Mineral. Petrol., v. 77, p. 207-213.

Young, R.A., 1993, The Rietveld Method. International Union of Crystallography, Oxford University Press, New York, NY, p. 298.

Zacchi, E.N.P., Silva, A.M., Toledo, C.L.B., Souza Filho, C.R., 2007, As três anomalias elípticas da porção sul do Cráton São Francisco: novos alvos para a mineralização de grafita? Revista Brasileira de Geofísica, v. 25, n. 4, p. 421-431.

Zagnitko, V.M., Lyzhachenko, N.M., Kurylo, S.I., 2013, Atypical graphite occurrences in Zavallya field. Naukovyi Visnyk Natsionalnoho Hirnychoho Universytetu, v. 4, p. 10–17.

Supplementary material

Supplementary Table 1. Carbon isotope and XRD data.

Sample	$\delta^{13}C$‰	XRD results								
		2θ	$d_{(002)}$ (Å)	sd ±	FWHM (2θ)	$Lc_{(002)}$ (Å)	sd ±	GD	T(°C)	sd ±
012D-1	-27.89	26.516	3.362	0.01	0.138	592	62	149	756	38
012D-2		26.491	3.365	0.01	0.138	592	62	147	752	38
012D-3		26.430	3.372	0.01	0.138	592	62	144	741	37
012D-4		26.586	3.353	0.005	0.138	592	62	153	768	38
014QZ-1	-	26.448	3.370	0.01	0.157	518	50	116	650	33
014QZ-2		26.546	3.358	0.005	0.217	377	39	81	538	27
014QZ-3		26.478	3.366	0.01	0.157	518	54	117	654	33
014QZ-4		26.514	3.362	0.01	0.177	461	48	101	602	30
014-1	-25.70	26.519	3.361	0.01	0.197	415	43	89	564	28
014-2		26.504	3.363	0.01	0.157	519	54	118	658	33
014-3		26.629	3.348	0.005	0.177	461	48	105	615	31
014-4		26.555	3.357	0.005	0.177	461	48	102	606	30
015A-1	-21.23	26.451	3.370	0.01	0.138	592	62	145	745	37
015A-2		26.507	3.363	0.01	0.138	592	62	148	754	38
015A-3		26.447	3.370	0.01	0.157	518	54	116	650	32
015A-4		26.555	3.357	0.005	0.157	519	54	120	665	33

Supplementary Table 2. Raman data (mean values and standard deviation std of the position, half width at half maximum (HWHM) obtained from the decomposition of three Raman spectra per analysis). R2 ratio and temperature estimates obtained by the IFORS method.

Sample	D1 ±1350 cm^{-1}				D3 ±1500 cm^{-1}				D2 ±1610 cm^{-1}				G ±1580 cm^{-1}				R2	Std	T(°C)	Std
	HWHM	Std	Center	Std	HWHM	Std	Center	Std	HWHM	Std	Center	Std	HWHM	Std	Center	Std				
012Dg1p1(red)	-	-	-	-	-	-	-	-	-	-	-	-	7.94	0.42	1581.58	0.00	0.00	0.00	605	30
012Dg1p2(blue)	14.23	0.00	1360.38	0.00	-	-	-	-	5.61	0.01	1623.83	0.00	7.87	0.00	1581.58	0.00	0.07	0.00	594	30
012Dg1p3(green)	19.12	0.03	1357.90	0.00	-	-	-	-	4.13	0.00	1623.83	0.00	7.78	0.00	1581.58	0.00	0.07	0.00	598	30
012Dg2p1(red)	20.14	0.01	1355.41	0.00	-	-	-	-	6.38	0.01	1621.35	0.00	8.33	0.00	1581.58	0.00	0.12	0.00	586	29
012Dg2p2(blue)	20.87	0.03	1353.75	1.43	16.40	2.09	1503.70	1.43	6.12	0.03	1618.86	0.00	8.91	0.00	1581.58	0.00	0.07	0.00	588	29
012Dg2p3(green)	-	-	-	-	-	-	-	-	-	-	-	-	8.06	0.48	1581.58	0.00	0.00	0.00	600	30
012Dg3p1(red)	22.37	0.11	1357.90	0.00	13.58	0.28	1503.70	1.43	4.21	0.00	1623.83	0.00	7.90	0.00	1581.58	0.00	0.05	0.00	598	30
012Dg3p2(blue)	23.41	0.04	1357.90	0.00	24.47	0.10	1502.05	0.00	3.88	0.00	1623.83	0.00	8.08	0.00	1584.06	0.00	0.14	0.16	597	30
012Dg3p3(green)	-	-	-	-	26.16	0.03	1509.50	0.00	8.74	0.04	1606.43	0.00	7.67	0.00	1581.58	0.00	0.00	0.00	587	29
012Dg4p1(red)	-	-	-	-	4.95	0.58	1497.08	0.00	-	-	-	-	7.71	0.00	1581.58	0.00	0.00	0.00	606	30
012Dg4p2(blue)	15.91	0.03	1357.90	0.00	13.37	0.10	1499.56	0.00	6.73	0.01	1618.86	0.00	7.78	0.00	1579.09	0.00	0.13	0.00	585	29
012Dg4p3(green)	22.35	0.00	1352.92	0.00	-	-	-	-	17.98	0.24	1611.40	0.00	7.79	0.01	1581.58	0.00	0.12	0.00	587	29
012Dg5p1(red)	37.22	0.12	1340.50	0.00	-	-	-	-	-	-	-	-	7.85	0.00	1581.58	0.00	0.06	0.00	599	30
012Dg5p2(blue)	16.48	0.05	1355.41	0.00	16.12	0.37	1494.59	0.00	6.61	0.00	1613.89	0.00	8.00	0.00	1574.12	0.00	0.12	0.00	581	29
012Dg5p3(green)	-	-	-	-	-	-	-	-	-	-	-	-	8.89	0.00	1581.58	0.00	0.00	0.00	593	30
014QZg1p1(red)	21.92	0.00	1351.47	0.00	-	-	-	-	-	-	-	-	8.90	0.00	1583.28	0.00	0.22	0.00	567	28
014QZg1p2(blue)	21.65	0.00	1348.97	0.00	-	-	-	-	-	-	-	-	8.78	0.00	1580.79	0.00	0.05	0.00	591	30
014QZg1p3(green)	20.33	0.00	1351.47	0.00	-	-	-	-	-	-	-	-	9.58	0.01	1582.45	1.44	0.04	0.00	581	29
014QZg2p3(green)	21.02	0.00	1353.96	0.00	-	-	-	-	2.49	0.00	1623.17	0.00	8.12	0.00	1580.79	0.00	0.06	0.00	598	30
014QZg3p2(blue)	22.00	0.02	1346.48	0.00	17.55	0.20	1498.53	0.00	12.42	0.05	1610.70	0.00	8.17	0.01	1575.81	0.00	0.06	0.00	595	30
014QZg3p3(green)	20.54	0.02	1348.97	0.00	-	-	-	-	4.30	0.01	1625.66	0.00	8.46	0.00	1583.28	0.00	0.03	0.00	592	30
014QZg4p2(blue)	20.59	0.00	1348.97	0.00	-	-	-	-	9.82	9.00	1613.20	8.63	8.94	0.02	1578.30	0.00	0.08	0.00	581	29
014QZg4p3(green)	-	-	-	-	-	-	-	-	-	-	-	-	8.01	0.00	1580.79	0.00	0.00	0.00	576	29
014QZg5p2(blue)	19.95	0.09	1353.96	0.00	46.26	4.22	1497.70	1.44	6.63	0.15	1623.17	0.00	9.09	0.01	1583.28	0.00	0.14	0.00	575	29
014QZg5p3(green)	22.66	0.01	1351.47	0.00	-	-	-	-	5.01	0.04	1623.17	0.00	9.82	0.00	1583.28	0.00	0.06	0.00	578	29
014QZg6p1(red)	19.95	0.00	1364.88	0.00	-	-	-	-	-	-	-	-	8.51	0.00	1588.78	0.00	0.09	0.00	588	29
014QZg6p2(blue)	21.42	0.01	1360.73	0.00	17.07	0.18	1505.85	0.00	-	-	-	-	8.36	0.00	1588.78	0.00	0.04	0.00	593	30
014QZg6p3(green)	19.86	0.00	1360.73	0.00	-	-	-	-	-	-	-	-	9.32	0.00	1588.78	0.00	0.05	0.00	591	30
014g1p2(blue)	22.45	0.01	1347.95	0.00	-	-	-	-	-	-	-	-	8.82	0.00	1579.09	0.00	0.07	0.00	581	29
014g1p3(green)	24.88	0.02	1342.98	0.00	-	-	-	-	-	-	-	-	9.74	0.00	1571.64	0.00	0.12	0.00	570	29
014g2p1(red)	21.96	0.01	1338.01	0.00	-	-	-	-	-	-	-	-	8.22	0.00	1579.09	0.00	0.04	0.00	597	30
014g2p3(green)	-	-	-	-	-	-	-	-	-	-	-	-	8.59	0.00	1579.09	0.00	0.00	0.00	598	30
014g3p1(red)	53.17	18.04	1354.58	1.43	39.46	12.60	1502.05	0.00	-	-	-	-	8.00	0.00	1576.61	0.00	0.05	0.02	597	30
014g3p2(blue)	22.34	0.01	1335.53	0.00	-	-	-	-	21.77	0.14	1584.06	0.00	9.92	0.02	1559.21	0.00	0.10	0.00	564	28
014g4p1(red)	24.19	0.01	1340.50	0.00	-	-	-	-	15.63	0.01	1589.04	0.00	9.00	0.00	1564.18	0.00	0.04	0.00	589	29
014g4p2(blue)	25.50	0.13	1345.47	0.00	63.81	4.38	1499.56	0.00	-	-	-	-	10.83	0.00	1574.12	0.00	0.06	0.00	568	28
014g4p3(green)	18.65	0.18	1352.92	0.00	-	-	-	-	8.77	0.01	1616.37	0.00	8.17	0.00	1576.61	0.00	0.22	0.00	568	28
014g5p1(red)	22.85	0.02	1347.95	0.00	68.77	1.17	1502.05	0.00	16.15	0.02	1603.95	0.00	8.54	0.01	1579.09	0.00	0.14	0.00	568	28
014g5p2(blue)	49.64	0.99	1347.95	0.00	42.69	0.35	1507.02	2.49	26.45	0.69	1596.49	0.00	7.79	0.00	1571.64	0.00	0.05	0.00	597	30
014g5p3(green)	17.05	0.02	1345.47	0.00	-	-	-	-	-	-	-	-	8.06	0.00	1579.09	0.00	0.01	0.00	602	30
015Ag1p2(blue)	21.64	0.02	1356.45	0.00	-	-	-	-	-	-	-	-	7.98	0.01	1583.28	0.00	0.01	0.00	597	30
015Ag1p3(green)	22.68	0.01	1353.96	0.00	-	-	-	-	-	-	-	-	8.00	0.01	1580.79	0.00	0.27	0.00	576	29
015Ag2p1(red)	-	-	-	-	10.55	0.09	1503.52	0.00	-	-	-	-	8.05	0.00	1583.28	0.00	0.00	0.00	602	30
015Ag2p2(blue)	19.58	0.00	1358.94	0.00	-	-	-	-	4.68	0.00	1625.66	0.00	7.78	0.00	1583.28	0.00	0.04	0.00	602	30
015Ag2p3(green)	21.92	0.05	1356.45	0.00	12.36	0.72	1501.03	0.00	4.04	0.01	1625.66	0.00	8.22	0.00	1583.28	0.00	0.06	0.00	594	30
015Ag3p1(red)	20.19	0.16	1358.94	0.00	51.11	2.21	1517.23	1.76	5.70	0.24	1623.17	0.00	7.77	0.00	1583.28	0.00	0.13	0.01	591	30
015Ag3p2(blue)	11.63	0.10	1358.94	0.00	-	-	-	-	-	-	-	-	8.19	0.00	1583.28	0.00	0.10	0.00	590	30
015Ag4p1(red)	17.17	0.19	1360.61	1.44	11.92	1.64	1499.36	1.44	5.07	0.01	1625.66	0.00	8.91	0.00	1583.28	0.00	0.04	0.00	584	29
015Ag4p3(green)	19.31	0.02	1358.94	0.00	18.38	0.11	1503.52	0.00	-	-	-	-	7.97	0.00	1580.79	0.00	0.02	0.00	602	30
015Ag5p1(red)	22.61	0.00	1353.96	0.00	-	-	-	-	8.35	0.05	1620.67	0.00	8.39	0.01	1580.79	0.00	0.24	0.00	564	28
015Ag5p2(blue)	27.12	0.89	1351.47	0.00	-	-	-	-	11.61	5.48	1618.18	2.49	7.95	0.00	1580.79	0.00	0.07	0.01	597	30
015Ag6p2(blue)	20.88	0.00	1356.59	0.00	-	-	-	-	-	-	-	-	9.18	0.00	1580.49	0.00	0.05	0.00	592	30
015Ag6p3(green)	23.43	0.00	1352.44	0.00	24.24	0.03	1497.56	0.00	8.77	0.01	1613.66	0.00	8.91	0.00	1572.20	0.00	0.12	0.00	582	29

Supplementary Table 3. Mean values and standard deviation (std) for the XRD and Raman data. "n" shows the number of analysis.

	XRD						Raman				
	n	**$d_{(002)}$ (Å)**	**std**	**GD**	**std**	**T(°C)**	**std**	**n**	**G HWHM (cm^{-1})**	**std**	**R2**	**std**
012D	4	3.363	0.008	148.2	3.6	754	11	15	8.04	0.38	0.062	0.053
014QZ	4	3.364	0.005	103.5	16.9	611	54	13	8.77	0.57	0.071	0.055
014	4	3.357	0.007	103.4	12.1	611	39	12	8.81	0.92	0.075	0.062
015A	4	3.365	0.006	132.4	16.7	704	54	13	8.25	0.46	0.088	0.083

ARTICLE II - Paleoproterozoic khondalites in Brazil: a case study of metamorphism and anatexis in khondalites from Itapecerica supracrustal succession of the southern São Francisco Craton

Daniel Andrade Miranda[a,*], Alexandre de Oliveira Chaves[a], Ivo Antonio Dussin[b], Carla Cristine Porcher[c].

[a] *Geology Department – Institute of Geosciences – Federal University of Minas Gerais (UFMG). Av. Antonio Carlos, 6627, Belo Horizonte – MG, Brazil. CEP 31270-901.*

[b] *Regional Geology and Geotectonic Department – State University of Rio de Janeiro (UERJ). R. São Francisco Xavier, 524. Rio de Janeiro – RJ, Brazil. CEP 20550-013.*

[c] *Institute of Geosciences – Federal University of Rio Grande do Sul (UFRGS). Av. Bento Gonçalves, 9500. Porto Alegre – RS, Brazil. CEP 91501-970.*

Published in periodic International Geology Review.

DOI: https://doi.org/10.1080/00206814.2020.1716273

ABSTRACT

In Brazil, Paleoproterozoic khondalites were recognized in Ceará, Bahia, Goiás, Tocantins, and Minas Gerais. The Itapecerica supracrustal succession in the Southern São Francisco Craton (Minas Gerais) contains sillimanite-cordierite-garnet-biotite gneiss (khondalite) with anatectic record. The high-grade khondalite preserve representative mineral assemblages of peak and orogen collapse after post-peak decompressional stage. Based on petrographic observations and P–T pseudosections of bulk rock compositions, a clockwise pressure-temperature-time (P–T-t) path was inferred. The metamorphic peak assemblage is liquid + plagioclase ± K-feldspar + garnet + biotite + ilmenite + sillimanite + quartz at 715–772 ºC and 5.5–7.5 kbar. In addition, the precursor sediments had mixed pelitic-wacke compositions resulting from erosion of different sources. Sediment deposition would have occurred at active continental marginal setting. Surrounding the khondalite occurs a peraluminous metagranite named here as Água Rasa, formed in syn- to post- collisional setting, whose $\varepsilon Nd_{(t)}$ (-0.5 to -2.7) and $^{87}Sr/^{86}Sr_{(t)}$ (1.04 to 1.08) and the data set indicate that the precursor magma of the Água Rasa metagranite originated from anatexis of the khondalitic rocks (crustal source) and associated amphibolites (mantle source) during the crustal thickening followed by tectonic exhumation at peak metamorphism and at decompressional stage during the orogenic collapse. The khondalite yielded ages from monazite U-Th-Pb_T dating of 2090±26 Ma and 1937±32 Ma, while the Água Rasa metagranite yielded ages of 2077±24 Ma and 1941±23 from monazite and 1934±74 Ma from zircon U-Pb. The ages of > 2.0 Ga are related to the metamorphic peak, while the younger ones (~ 1940 Ma) are related to the orogen collapse after post-peak decompressional stage. Similarities between the khondalite rocks of this study and of the North China Craton suggest that the São Francisco-Congo Craton was near the North China Craton in the supercontinent Columbia for the 2.1–1.9 Ga period

Keywords: Khondalite; Provenance; Anatexis; Petrology; Geochronology; P-T-t path; São Francisco Craton.

Introduction

From a global geodynamic perspective, khondalite belts represent precursor basins that underwent granulite-facies metamorphism because of subduction-collision process, culminating in the amalgamation of continental fragments (Teixeira et al. 2017a). The term khondalite was first used to designate a suite consisting of quartz-garnet-sillimanite ± graphite gneisses, garnet gneisses, quartz-feldspathic gneisses and quartzites, which host manganese deposits in Orissa, India (Walker 1902). In general, the khondalitic belts represent a significant component of granulite facies terrains, and the gneisses that occur associated with these belts correspond mainly to Alumina types (Pereira et al. 2016). High-grade metamorphic terrains on the Brazilian territory are represented, among others, by the granulitic belt of Goiás, the migmatite-granulite complexes of Minas Gerais and the granulitic belt of Santa Catarina (Pereira et al. 2016).

In Brazil, Paleoproterozoic khondalites were recognized in Itapecerica - Minas Gerais State (Campello et al. 2015; Chaves et al. 2015; Teixeira et al. 2017a; Miranda et al. 2019), in Granja - Ceará State, (Santos et al. 2001; Silva et al. 2014), in Canavieiras/Rio Pardo (Litwinsky 1985; Delgado et al. 1988), Brejões (Barbosa and Sabaté 2004; Barbosa 2006; Barbosa et al. 2006; Queiroz 2016) and Tanque-Novo Ipirá complex - Bahia State (Kosin et al. 1999; Kosin et al. 2003), and in Ticunzal Formation - Goiás/Tocantins States (Botelho et al. 2006; Fuck et al. 2006; Fuck et al. 2014; Cuadros et al. 2017) (Fig. 1). Some of their characteristics are listed on table 1.

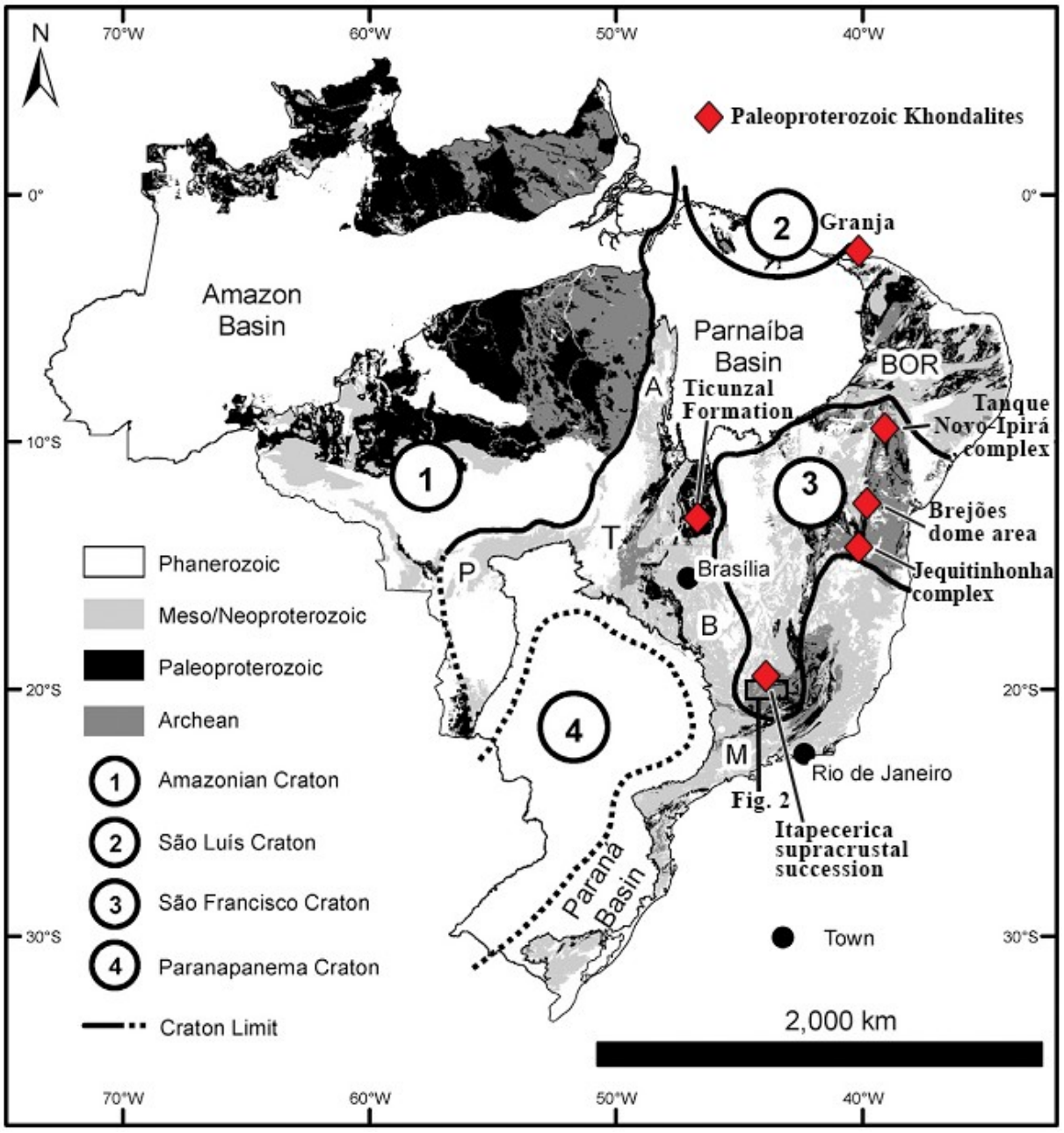

Figure 1. Paleoproterozoic Khondalite occurrences in Brazil. BOR – Borborema Structural Province. M – Mantiqueira Structural Province. T – Tocantins Structural Province. P – Paraguai Belt. A – Araguaia Belt. B – Brasília Belt. Modified from Fuck et al. (2014).

Table 1 – Paleoproterozoic khondalite-like occurrences in Brazil (Mineral abbreviations after Whitney and Evans 2010).

Location	Unit	Rock	Age	T/P estimates and/or metamorphic facies	References
Minas Gerais	Itapecerica supracrustal succession	Sil-Crd-Grt-Bt gneiss	Paleoproterozoic U-Th-Pb_T monazite of 2090 ± 26 Ma and 1937 ± 32 Ma	715–768 ºC and 5.5–7.5 kbar Granulite	Campello et al. 2015; Chaves et al. 2015; Teixeira et al. (2017a); Miranda et al. (2019)
Ceará	Granja paragneisses	Grt-Sil-Bt-Qz-Pl gneiss	Paleoproterozoic	850-950 ºC and 9-10 kbar Granulite	Santos et al. 2001; Silva et al. 2014; Silva 2017
Bahia	Jequitinhonha complex	Bt-Grt gneiss/Bt-Sil-Crd-Grt gneiss/ kinzigite gneiss/quartzite/amphibolite	Paleoproterozoic	High amphibolite	Litwinsky 1985; Delgado et al. 1988
	Brejões dome area metasedimentary granulites/heterogeneous granulites	Quartzite/Pl-Qz-Grt-Bt gneiss	Paleoproterozoic	~850 °C and 5-6 kbar Granulite	Barbosa and Sabaté 2004; Barbosa 2006; Barbosa et al. 2006; Queiroz 2016
	Tanque Novo-Ipirá complex/Bom Despacho gneiss	Gr gneiss/Quartzite/Bt gneiss	Neoarchean/Paleoproterozoic	High amphibolite to Granulite	Kosin et al. (1999); Kosin et al. (2003)
Goiás and Tocantins	Ticunzal Formation	Qz-Ms-Gr xist/Bt-Grt gneiss	Paleoproterozoic U-Pb zircon 2166±10 Ma and 2120±2 Ma	Granulite	Botelho et al. 2006; Fuck et al. 2006; Fuck et al. 2014; Cuadros et al. 2017

In Minas Gerais, the Paleoproterozoic Itapecerica graphite-rich supracrustal succession keep a high-grade paragenesis with sillimanite ± cordierite ± garnet ± biotite ± graphite (Campello et al. 2015; Chaves et al. 2015; Teixeira et al. 2017a) with maximum depositional age of ~2080 Ma (Teixeira et al. 2017a). Chaves et al. (2015) suggest that the sillimanite-cordierite-garnet-biotite paragenesis indicate that these rocks formed under high amphibolite- to granulite-facies conditions with temperatures in order of 750-800ºC. Miranda and Chaves (2019) found temperatures around 729 ºC analyzing the graphite from Itapecerica supracrustal succession rocks. Cai et al. (2017) found P-T conditions of peak at 830-860 ºC and 9.5-11 kbar on similar rocks of the same metamorphism age (~ 1.95 Ga) and depositional age of 2.3-2.0 Ga (Wan et al. 2006) in Wulashan complex on the North China Craton. Calculating the conditions of pressure (P) and temperature (T) are essential to understand regional geology settings and the tectonic evolution of the southern São Francisco Craton.

According to Cai et al. (2017) phase equilibria modeling has been widely applied to the investigations of khondalite metamorphism in recent years and provides a powerful way of constraining multistage metamorphic P-T conditions. Traditional geothermobarometry has several limitations compared to phase equilibria modeling (Powell and Holland, 2008).

Geophysical images based on high-density airborne gamma-ray spectrometric data (Ruy et al. 2006; Zacchi et al. 2007) in the Itapecerica region allowed distinguishing three nearly elliptical anomalies that host the Itapcerecica supracrustal sequence (Fig. 2). Campello et al. (2015) describe a peraluminous metagranitoid that surrounds the Itapecerica khondalitic rocks. In this study, the proposed name for the peraluminous gneiss is Água Rasa metagranite.

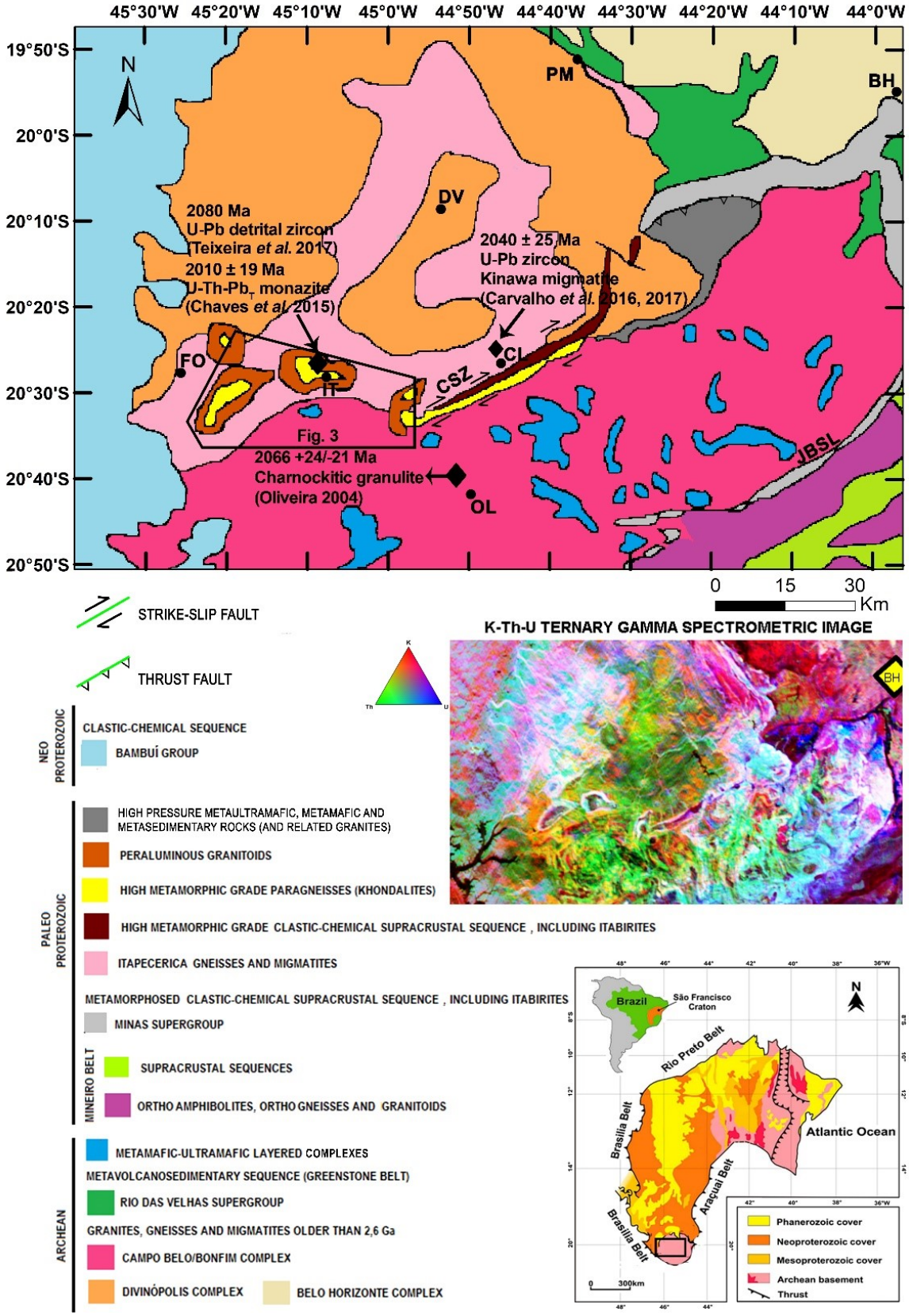

Figure 2. Simplified geological map of the southern portion of the São Francisco Craton. Keys: CSZ = Cláudio Shear Zone; JBSL = Jeceaba-Bom Sucesso Lineament. Towns: BH (Belo Horizonte), CL (Cláudio), DV (Divinópolis), FO (Formiga), IT (Itapecerica), OL (Oliveira), PM (Pará de Minas). K-Th-U ternary gamma spectrometric image of the southern São Francisco Craton from CPRM-CODEMIG (2014). Black polygon marks the location of the studied area (Fig. 3).

In order to evaluate the conditions of pressure (P), temperature (T) and the age of the metamorphism, pseudosections are constructed for Itapecerica khondalites combined with monazite and zircon geochronology of the khondalite and Água Rasa metagranite to provide the pressure-temperature-time (P-T-t) path of the metamorphism under which khondalite and nearby amphibolite anatexis took place to generate the Água Rasa metagranite. Additionally, Rb-Sr and Sm-Nd analysis were obtained to investigate the magma sources during the formation of the Água Rasa metagranite.

Geological Setting

The southern part of São Francisco Craton (SFC) (Fig. 2) comprises an Archean crust (3.2–2.6 Ga) composed mainly of granite-gneisses terranes (Farina et al. 2015; Teixeira et al. 2017b) and greenstone belts (Rio das Velhas Supergroup), including associations of mafic-ultramafic (komatiite) rocks with intermediate-felsic volcanic rocks, volcanoclastic rocks (Noce et al. 1998) and clastic sediments (Dorr 1969; Baltazar and Zucchetti 2007). Different metamorphic complexes named as Divinópolis, Campo Belo/Bonfim and Belo Horizonte (Machado Filho et al. 1983; Teixeira et al. 1996) compose the subdivision of the Archaean granitic basement (Fig. 2). Paleoproterozoic clastic-chemical metasedimentary rocks (including the banded iron formations of the Quadrilatero Ferrifero (QF) from Minas Supergroup, with a minimum deposition age ~2.0 Ga (Machado et al. 1996; Moreira et al. 2016) and Neoproterozoic pelitic-carbonate sedimentary rocks from Bambuí Group (Teixeira et al. 2017b) are also found in the southern SFC. The Minas Supergroup, formed in the Paleoproterozoic orogeny, extends to the SW of the QF, as portrayed by the correlative strata along the Jeceaba-Bom Sucesso lineament (Neri et al. 2013). Mafic dykes of several generations crosscut the southern SFC (Chaves 2013).

The Paleoproterozoic Minas accretionary orogeny (Rhyacian-Orosirian orogeny) represents the accretion of juvenile crust that formed the Mineiro Belt (Noce et al. 1998; Ávila et al. 2014; Teixeira et al. 2015) and was responsible for extensive reworking of terranes located at the margins of the craton (Noce et al. 2007). Alkmim and Marshak (1998) made a speculative reconstruction of the provinces after the Rhyacian-Orosirian orogeny, which shows that a great part of the southern portion of the São Francisco paleoplate lay in the foreland of that orogeny. Several studies (Campos and Carneiro, 2008; Heilbron et al. 2010; Ávila et al. 2014; Teixeira et al. 2015; Barbosa et al. 2015) maintain that the NW limit between the Mineiro Belt and the Archean core is defined by the NE-SW Jeceaba Bom-

Sucesso lineament (JBSL in Fig. 2). However, the Kinawa migmatite of the Itapecerica Metamorphic Complex is an example of reworked granitic crust, in which 2.7 Ga metagranodiorites of the Campo Belo/Bonfim Metamorphic Complex were partially melted in the Cláudio Shear Zone (CSZ in Fig. 2) during the Paleoproterozoic. SHRIMP zircon U-Pb ages of 2.05-2.03 Ga (Carvalho et al. 2017) show the zircon producing event recognized in the interior part of the southern SFC Archean core and confirm the existence of a Paleoproterozoic event previously recognized only from monazite in sillimanite-cordierite-garnet-biotite gneiss (graphite-rich khondalitic rocks) near CSZ (Chaves et al. 2015).

The study area is located in Itapecerica region (Fig. 2) and, according to Carneiro and Barbosa (2008), the area contains gneisses, metagranitoids, amphibolites, mafic, metaultramafic and metacharnockitic rocks formed in Mesoarchean. Those rocks were recrystallized under high amphibolite- to granulite facies conditions (Fernandes and Carneiro 2000). The elliptical geophysical anomalies (Fig. 3) hosting the second largest graphite mine in Brazil are located to the west of the CSZ around Itapecerica town. The perimeter of the elliptical anomalies is constituted by the Água Rasa metagranite, which appears in white in gamma spectrometric image in figure 3.

Neoarchean Candeias and Paleoproterozoic Itapecerica gneissic units surround the Água Rasa metagranite and the Itapecerica supracrustal succession rocks (Fig. 3). Both units show variable migmatization (Oliveira 2004; Campello et al. 2015). The Candeias-type rocks are essentially banded gneisses and subordinately charnockitic granulites that vary from granodioritic to granitic in composition. The mineral paragenesis hypersthene-diopside-hornblende-biotite is consistent with high-grade metamorphism under retrograde amphibolite-facies metamorphic conditions (Carneiro et al. 2007). The adjacent peraluminous Itapecerica Gneiss show granitic to granodioritic composition and is locally migmatized. The main mineral constituents are K-feldspar, plagioclase, quartz, biotite and rare amphibole in a granoblastic texture. Zircon, apatite, opaques, chlorite, sericite and epidote are the common accessory and secondary minerals (Carneiro et al. 2007).

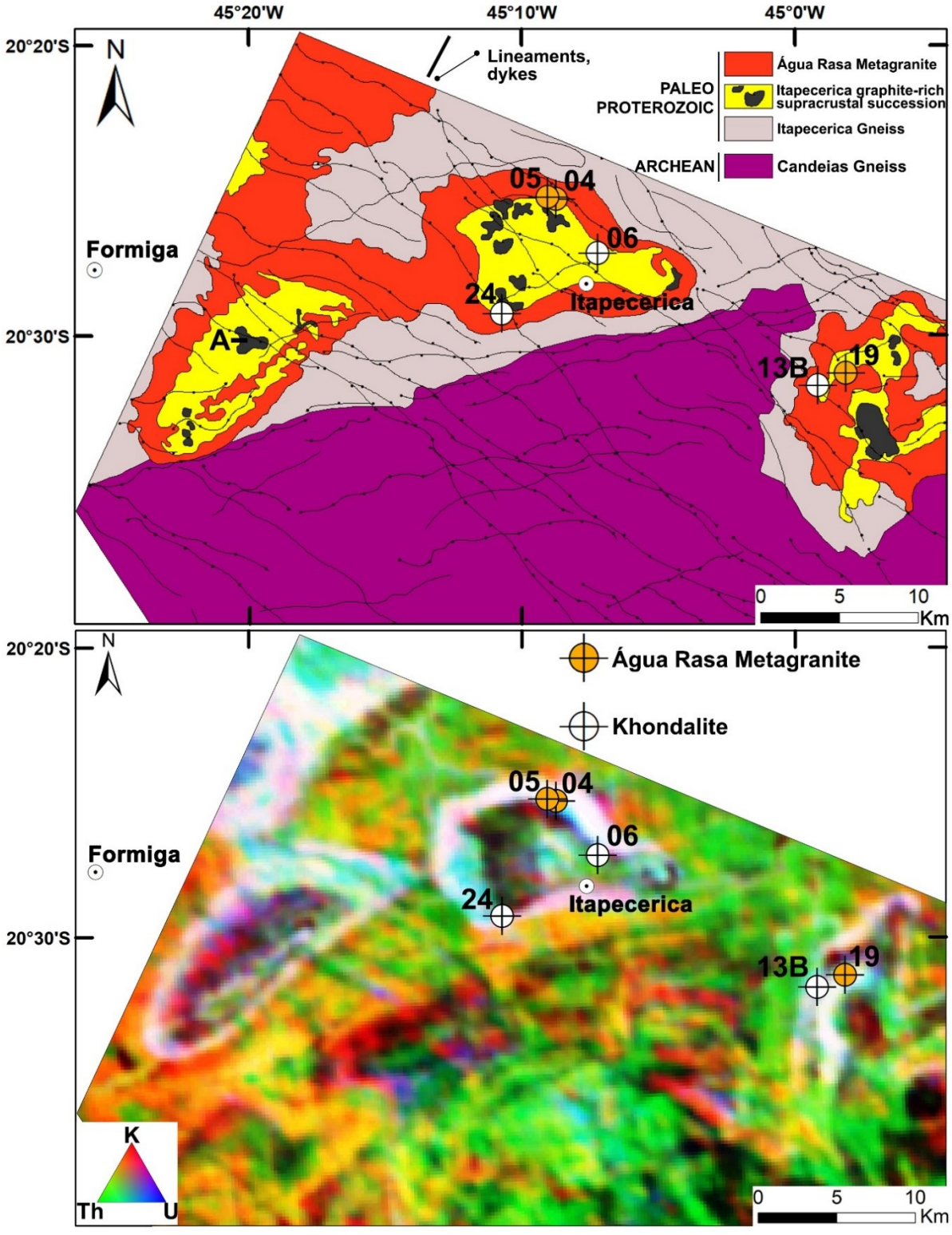

Figure 3. Geological map and Gamma-ray ternary K-Th-U map showing the elliptical geophysical anomalies, which host the graphite-rich supracrustal succession rocks and the Água Rasa metagranite with samples sites. Adapted from Ruy et al. (2006) and Zacchi et al. (2007). A = Amphibolite.

The Itapecerica graphite-rich supracrustal succession rocks occur along E-W trending exposure. Amphibolite bodies occur together inside elliptical geophysical anomalies (Fig. 3). These succession rocks essentially consists of khondalite paragneiss and minor lenticular graphite schist that is interlayered with quartzite bands (partly ferruginous with laminar graphite). In particular, the khondalite exhibits compositional layering and local anatexis and may contain thin graphite films (Carneiro et al. 2007; Campello et al. 2015). The bedding strikes (NE-SW, NW-SE, and E-W) and dips (from 10º to 80º) of the Itapecerica supracrustal succession vary, which suggest complex deformation (Teixeira et al. 2017a).

Teixeira et al. (2017a) conducted isotopic studies on the Itapecerica graphite-rich supracrustal succession and the detrital zircon analyses in paragneiss indicated a maximum deposition age of 2080 Ma and a metamorphic overprint on granulite facies of 2069 ± 84 Ma (Fig. 2). Chaves et al. (2015) previously reported monazite electron microprobe chemical data in paragneisses that yielded a U-Th-Pb_T mean age of 2010 ± 19 Ma (Fig. 2); this age is also related to time of the high-grade metamorphism.

Methods

Mineral chemistry

After micropetrography of three samples done in a Nikon microscope, garnet, biotite, plagioclase and cordierite (Supplementary Table 2 to 5) were analyzed with a JXA-8900 JEOL electron microprobe (EMP), at Microanalysis Laboratory of the Microscopy Center at Federal University of Minas Gerais (LMA-CM-UFMG), by using wavelength dispersive X-ray spectroscopy (WDS). Operating conditions were 15 kV accelerating voltage and 20 nA sample current. Oxide and silicate standards were used for calibration. Counting times were 10-20 s on the peak and 5-10 s on the background. Three spectrometers were used simultaneously. A ZAF correction procedure was applied. The electron beam was focused to the minimum size (2 micrometers). Mineral imaging has been done by using backscattered electron technique.

Whole-rock geochemistry

Three rock samples of the khondalite (Supplementary Table 1) and three samples of the Água Rasa metagranite (Supplementary Table 6) were sent to the SGS-Geosol Laboratory, where, after milling in a tungsten mill, the rock powder material was melted with lithium

metaborate and dilute nitric digestion. The major elements and five trace elements (Ba, Nb, Sr, Y, Zr) were analyzed by ICP-OES (Optical Emission Spectrometry with Inductively Coupled Plasma). Seven other traces, together with fourteen rare earth elements, were analyzed by ICP-MS (Inductively Coupled Plasma Mass Spectrometry). Detection limits were generally around 0.01% for the higher oxides and 1 ppm for the others. The accuracy is in the range of 1-2% from the relative standard deviation. The loss on ignition (LOI) occurred by mass difference after heating at 1000 °C. Then, to examine the geochemical data the Geoplot program (Zhou and Li 2006), a supplement for Microsoft Excel, was used.

Zircon U-Pb geochronology

In the Laboratory of Isotopic Geology (LGI) of the Federal University of Rio Grande do Sul (UFRGS) the extraction of zircons from one sample of the Água Rasa metagranite (Supplementary Table 7) followed the conventional processes of concentration of heavy minerals, i.e. crushing, grinding and sieving with separation of the fine fraction material (less than 180 mesh). The grains individually selected were placed on acrylic resin and the mount was polished with alumina powder to expose the centers of the grains. The cathodoluminescence (CL) images of the zircon grains were obtained in a scanning electron microscope (SEM) JEOL 6510, at the Image Laboratory of Federal University of Ouro Preto (UFOP).

The data were obtained through a multicollector Thermo-Finnigan Neptune MC-ICP-MS connected to a laser system Photon-Machines of 193 nm G2 at UFOP following the procedure described in Santos et al. (2017). The configuration parameters used in the instrument were 30 μm spot diameter, 6 Hz frequency, 10% energy and with intensity of 0.3 mJ. The U-Pb data were standardized using zircon GJ-1 (609 Ma, Jackson et al. 2004) as the primary standard and tested using zircon Plesovice (337 Ma, Slama et al. 2008) and BB (560 Ma, Santos et al. 2017) as secondary patterns. External errors were propagated considering internal reproducibility of the individual ratios, external reproducibility of GJ-1, and long-term uncertainty of pattern validation, uncertainty in reference pattern ratios, and uncertainty of Pb-common index (Lana et al. 2017). The evaluation of the data for each spot was filtered considering the outliers of the values of common Pb content, individual errors of the isotopic ratios, high percentages of discordance and Th/U ratio. From the selected points, only those with discordance less than 25% were used to calculate and plot in discordia diagrams. The discordia diagrams were obtained using the software Isoplot/Ex (Ludwig, 2003) and, the

individual uncertainties are presented in level 2σ.

Monazite mineral chemistry and U-Th-Pb_T geochronology

Regarding microanalysis for geochronological purposes, the compositions of different monazite grains in rock polished thin sections were determined using the same JEOL EMP of the LMA-CM-UFMG (Supplementary Table 8, 10). Standards and quantitative WDS analytical parameters used during monazite analyses are described in Chaves et al. (2013). A ZAF correction procedure was applied. Overlaps of X-ray peaks between Y and Pb have not been corrected because there was no measurement in PbMa (Lead M alpha), but only in PbMb (Lead M beta). However, to avoid errors in the obtained ages, the interference of ThMz (Thorium M gamma) on the measured UMb (Uranium M beta) had to be corrected, following Scherrer et al. (2000) in adaptation to the conditions of the LMA-CM-UFMG, as follows (Chaves et al. 2013):

$$U_{corrected} = U_{measured} - (0.006365 \times Th_{measured}).$$

Microprobe chemical U-Th-Pb_T ages and associated errors were obtained using EPMA Dating software (Pommier et al., 2004) and the average ages were taken through Isoplot/Ex software (Ludwig, 2003). The age equation used is:

$$Pb = \{Th \times [\exp(\lambda_{232}T)-1] \times (M_{208}/M_{232})\} + \{Uc \times [\exp(\lambda_{238}T)-1] \times (M_{206}/M_{238}) \times 0.9928\} + \{Uc \times [\exp(\lambda_{235}T) - 1] \times (M_{207}/M_{235}) \times 0.0072\}$$

Where $^{238}U/(^{235}U+^{238}U) = 0.9928$ and $^{235}U/(^{235}U+^{238}U) = 0.0072$. Uc (U corrected), Th and Pb are concentrations in ppm; T is the age in Ma; M_{206}, M_{207}, M_{208}, M_{235}, M_{238}, M_{232} are the atomic masses of ^{206}Pb, ^{207}Pb, ^{208}Pb, ^{235}U, ^{238}U, ^{232}Th; $\lambda_{232} = 0.49475 \times 10^{-4}$ Ma^{-1}; $\lambda_{238} = 1.55125 \times 10^{-4}$ Ma^{-1}; $\lambda_{235} = 9.8485 \times 10^{-4}$ Ma^{-1} (Pommier et al., 2004).

WDS Yttrium compositional maps of the selected grains that would allow detecting heterogeneities eventually correlated to different geological events (Williams et al., 2007) have been acquired by using the same JEOL EMP of the LMA-CM-UFMG.

Whole-rock Sm-Nd and Rb-Sr

Sm-Nd and Rb-Sr isotopes of two samples of the Água Rasa metagranite were obtained in the LGI of UFRGS (Supplementary Table 9). The isotopic data were acquired using a VG54E Sector multi-collector thermal mass spectrometer (TIMS). The analytical

procedures and the dissolution routine are described with details in Gioia and Pimentel (2000). The Neodymium ratios were corrected for fractionation during normalization analysis for a $^{146}Nd/^{144}Nd$ ratio of 0.7219 and adjusted for bias based on SPEX Nd, assuming $^{143}Nd/^{144}Nd = 0.511110$ and calibrated against Nd La Jolla assuming a value of $^{143}Nd/^{144}Nd$ of 0.511856. εNd and $^{143}Nd/^{144}Nd_{(t)}$ calculated for rock crystallization age. Nd blank during the analysis was less than 160 pg. The raw data was reduced using Excel macros produced in the LGI. The value of the age of the mantle depletion model (TDM) for whole-rock samples was calculated using DePaolo (1988) model. The $^{87}Sr/^{86}Sr$ isotope ratios were normalized to $^{86}Sr/^{88}Sr = 0.1194$ and adjusted for bias based on $SrCO_3$ NBS-987 using $^{87}Sr/^{86}Sr = 0.71025$; NBS $987_{(LGI)} = 0.71026 \pm 0.0011$. Sr blank during the analysis was less than 100 pg. $^{87}Rb/^{86}Sr$ ratio was calculated based on elementary data of Rb and Sr. $^{87}Sr/^{86}Sr^*$ = mean ratio on the mass spectrometer; $^{87}Sr/^{86}Sr_{(t)}$ = calculated ratio based on rock crystallization age. SE (%) = standard error.

Phase equilibria modeling

The pressure-temperature (P-T) conditions were investigated by phase equilibrium calculations in the system $MnO–Na_2O–CaO–K_2O–FeO–MgO–Al_2O_3–SiO_2–H_2O–TiO_2–Fe_2O_3$ (MnNCKFMASHTO), using THERIAK-DOMINO software (De Capitani and Petrakakis 2010), in combination with the updated td-tcds62-6axmn-03.txt database of metapelites from Holland and Powel (2011). This database handle ferric iron using the traditional approach used in Theriak-Domino by controlling the amount of ferric iron in a calculation by specifying the proper amount of oxygen, and there is thus only one Fe system component, denoted “FE”. The a-x models used for the phase equilibria modeling were plagioclase (Holland and Powell 2003); garnet and biotite (White et al. 2014a; 2014b); Melt (White et al. 2002; 2014b); ilmenite (White et al. 2000; 2014a); spinel-magnetite (White et al. 2000; 2002) and cordierite (Holland and Powell 2011; White et al. 2014a; 2014b). Mineral abbreviations are: Pl – plagioclase; Kfs – K-feldspar; Grt – garnet; Bt – biotite; Ilm – ilmenite; Crd – cordierite; Liq – silicate liquid/melt; Qz – quartz; Ky – kyanite; Sil – sillimanite; And – Andalusite. Pseudosections were calculated using **bulk rock composition** from three samples of the khondalite (not in the leucosome portions) and isopleths were calculated using the mineral chemistry. Appropriate values for water content were investigated on T-X pseudosections and the bulk H_2O values (06 = 0.90 wt%; 13B = 1.0 wt%; 024 = 1.5 wt %) were chosen according to the methodology of White et al. (2001).

Results

Three samples (06, 13B, and 24) of the sillimanite-cordierite-garnet-biotite gneiss (khondalite) (Fig. 3 and Fig. 4A, 4B) and three samples (04, 05, and 19) of Água Rasa metagranite (Fig. 3 and Fig. 4C, 4D) were collected for detailed petrological and geochronological investigation. Mineral abbreviations are after Whitney and Evans (2010), including: Bt – Biotite; Crd – Cordierite; Grt – Garnet; Ilm – Ilmenite; Kfs – K-feldspar; Pl – Plagioclase; Qz – Quartz; Sil – Sillimanite; Mnz – Monazite.

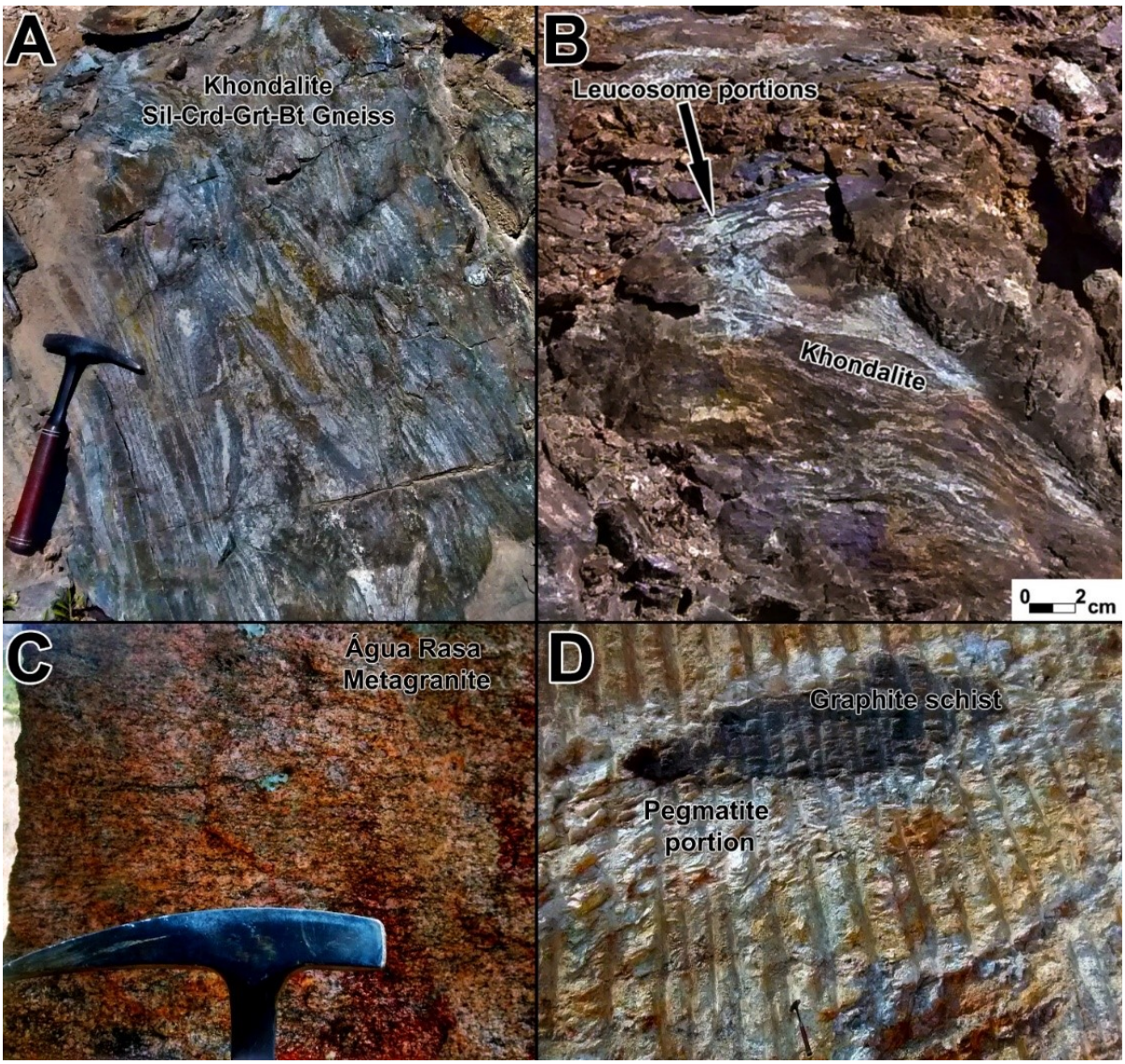

Figure 4. Outcrop photos showing key macroscopic relationships found. (A) Sil-Crd-Grt-Bt gneiss folded, revealing the complex deformation. (B) Sil-Crd-Grt-Bt gneiss keeping leucosome portions. (C) Água Rasa metagranite showing his weak foliation denoted by the mafic minerals, especially biotite. (D) Pegmatite portion of the Água Rasa metagranite with a graphite schist xenolith (or melting residue?) from the Itapecerica supracrustal succession rocks.

Sillimanite-Cordierite-Garnet-Biotite Gneiss (khondalite)

The khondalite is part of the Itapecerica graphite-rich supracrustal succession rocks and exhibits compositional layering characterized by the variance of grey/dark sillimanite-garnet-biotite-rich layers and thick leucocratic quartz-feldspathic bands with local anatexis and complex deformation (Fig. 4A, 4B).

Petrography and microstructures

Khondalite shows granolepidoblastic texture with oriented biotite crystals throughout the demarcated foliation (Fig. 5). Garnet is usually poikiloblastic, with quartz, biotite, ilmenite and plagioclase inclusions. Fibrolitic sillimanite occurs within cordierite, which is altered to pinite. Cordierite occurs in a banded form associated with biotite parallel to the foliation and at garnet rims. In addition, fine-grained biotite and plagioclase are distributed around garnet. In localized domains, garnet is surrounded by biotite. Plagioclase occurs disperse in the matrix alongside with quartz and is usually altered to saussurite. No K-feldspar was found. Monazite, zircon and ilmenite were accessory minerals. In modal terms, the studied rock is classified as a sillimanite-cordierite-garnet-biotite gneiss.

During the metamorphic peak, the possible stable assembly is indicated by the presence of preserved equigranular texture of biotite, sillimanite, K-feldspar, plagioclase, quartz and garnet (Fig. 5A-5F). In the matrix, it is possible to observe the consumption of the edges of relict biotite crystals due to replacement with plagioclase (Fig. 5B) and the garnet grows by consuming sillimanite, biotite and plagioclase. The biotite-melting dehydratation reaction of Patiño Douce and Johnston (1991) describes this process:

$$Bt + Sil + Qz \pm Pl \rightarrow Grt + Kfs + Melt$$

In the post-peak, the matrix cordierite grows incorporating biotite relicts, sillimanite and quartz (Fig. 5C) due to biotite decompression melting reaction described by Harley and Carrington (2001):

$$Bt + Sil + Qz \pm Pl \rightarrow Crd + Kfs \pm Ilm + Melt$$

The presence of fine-grained minerals of biotite, plagioclase and quartz and coarse/anhedral grains of cordierite, quartz, sillimanite and biotite surrounding garnet (Fig.

5B, 5C, 5D, 5E, 5F) show that the melt generated at the metamorphic peak was being consumed during the decompressional stage. This feature seems to indicate different local compositions (Cai et al. 2017). Garnet rims replaced by cordierite and relicts of sillimanite and quartz (Fig. 5B, 5C) also occurs from the consumption of melt by the reaction described by Cai et al. (2017) and is common in typical high-grade metapelitic rocks areas from the North China Craton (Jiao et al. 2013; Cai et al. 2014; Cai et al. 2017):

$$Grt + Sil + Melt \rightarrow Crd + Bt + Fe\text{–}oxide$$

Biotite, plagioclase and quartz on the rims of garnet (Fig. 5E, 5F) are described by Vielzeuf and Montel (1994) as the garnet breakdown reaction:

$$Grt + Melt \rightarrow Bt + Qz \pm Pl$$

In addition, garnets surrounded by coarse grains of biotite with euhedral to subhedral shapes (Fig. 5F) also indicates the replacement of garnet by the reverse reaction of biotite dehydration described by Patiño Douce and Johnston (1991):

$$Grt + Kfs + Melt \rightarrow Bt + Sil + Qz \pm Pl$$

Finally, in minor concentrated portions with garnet without included minerals and interstitially distributed along quartz grain boundaries, garnet rims with quartz/plagioclase films and symplectites of cordierite mantle garnet (Fig. 5D, 5E, 5F) indicates crystallization of the remaining melt. These reactions are similar to those found in khondalite from North China Craton described by Cai et al. (2017).

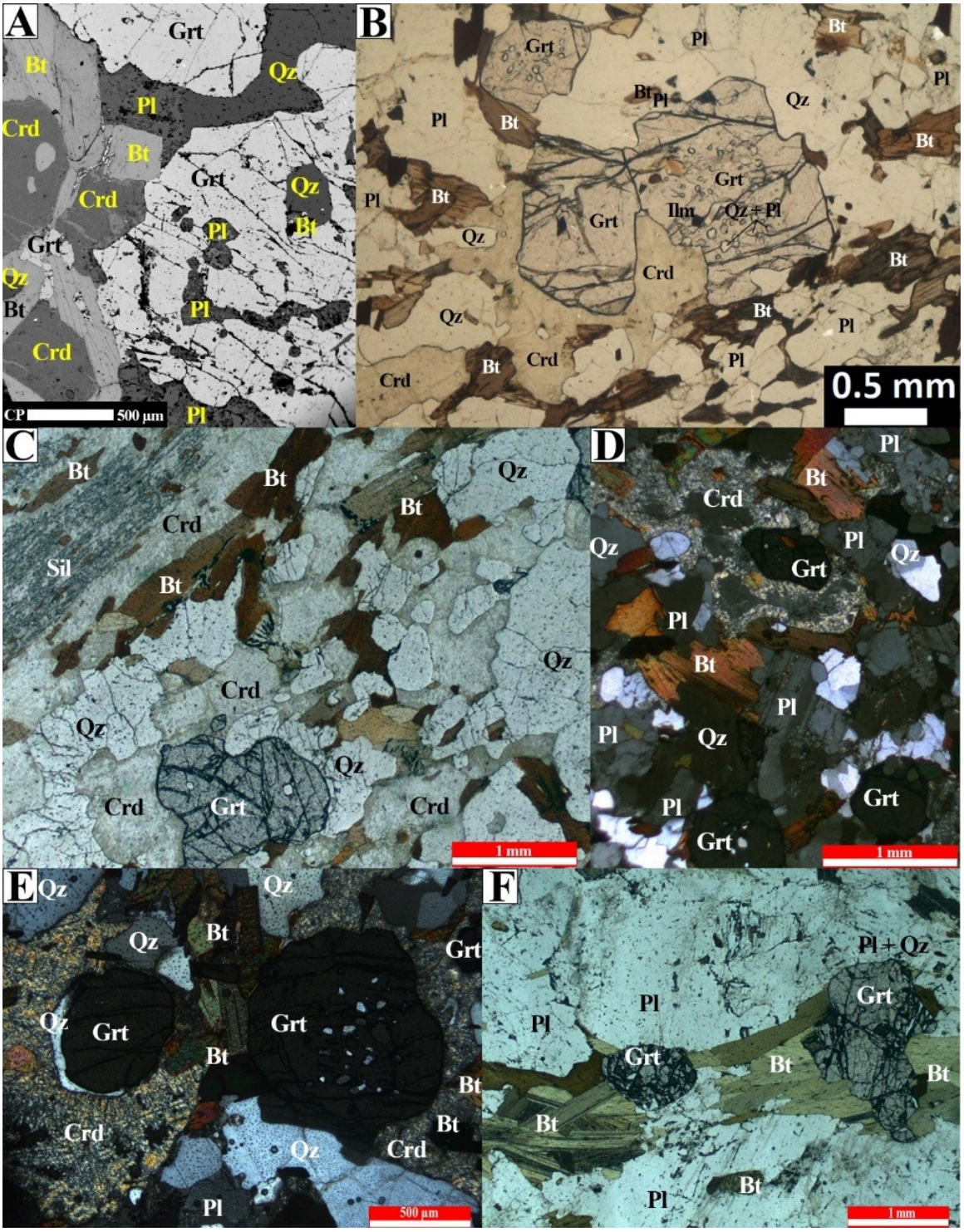

Figure 5. Photomicrographs (plane-polarized light, PPL; cross-polarized light, CPL) and back-scattered electron (BSE) images of representative mineral assemblages and microstructures of the khondalite. (A) BSE image of biotite + plagioclase + quartz inclusions in garnet. (B) Photomicrograph (PPL) of inclusions in garnet, matrix biotite partially replaced by plagioclase, biotite included in cordierite (pinitized) and garnet partially consumed with wedge-shaped or irregular rim in contact with quartz and cordierite. (C) Photomicrograph (PPL) of garnet, coarse-grained biotite in matrix and fibrolitic sillimanite inclusions in cordierite. (D) Photomicrograph (CPL) showing microdomains of Grt–Crd–Sil gneisses or garnet-bearing quartz plagioclase leucosomes and mantled by a corona of cordierite and late re-crystallized biotite forming the outer rim. (E) Photomicrograph (CPL) of quartz mantling garnet related to melt-consuming reaction. (F) Photomicrograph (PPL) of garnet surrounded by coarse-grained biotite with euhedral to subhedral shapes, in the quartz-feldspar leucosome microdomains. Mineral abbreviations are after Whitney and Evans (2010).

Whole-rock geochemistry

The results of whole-rock geochemistry for the khondalite are listed on the supplementary table 1. Not only Itapecerica khondalite samples in the diagram of Werner (1987) indicate a sedimentary origin displaying low P_2O_5/TiO_2 ratios (Fig. 6A), but also the samples from Silva et al. (2014). The high MgO/CaO ratio of the sample 24 is due to its higher cordierite/biotite content than samples 06 and 13B. In the precursor sediment classification diagram of Herron (1988), khondalite samples and samples from Cai et al. (2017) indicate a wacke domain. Samples from Silva et al. (2014) plot on the boundary between greywacke and shale domains (Fig. 6B). The empirical ratio of $100TiO_2/Zr$ (wt.%/ppm) based on a transition metal (Ti) and a high field-strength element (Zr), which are assumed to have an immobile behavior during metamorphism (Silva et al. 2014), varies from 0.35 to 0.57 for the khondalites, indicating a significant input of psammitic material in the precursor sediments according to Garcia et al. (1991) and Abu El-Enen (2011).

The variation in the K_2O/Na_2O ratio for the khondalites (0.85 to 10.87) suggests a diversity of protholith rock types (pelitic to semipelitic). In the A-CN-K ternary plot of Nesbitt and Young (1984), the khondalite samples, Cai et al. (2017) samples and samples from Silva et al. (2014) define a trend between silt-clay and clay sediments consistent with a mixed greywacke-shale composition (Fig. 6C). The chemical index of alteration (CIA = $[(Al_2O_3/(Al_2O_3+CaO+Na_2O+K_2O))*100]$) from Nesbitt and Young (1982) for the khondalites varies from 69-77 with average of 73, indicating the typical values for chemical weathering of shales (70-75) as parent sedimentary rocks.

The rare earth elements (REE) patterns for khondalites, represented in a chondrite-normalized diagram (Sun and McDonough, 1989), show enrichment of light rare earth elements (LREE) with LREE / HREE fractionation (La_N/Yb_N = 9.16 - 18.02) and flat heavy rare earth elements (HREE) pattern (Gd_N/Yb_N = 1.49 - 2.15) and Eu negative anomalies (Eu/Eu*) = 0.14 - 0.21) (Fig. 6D). The same pattern is observed on samples from Silva et al. (2014) and presents close similarities to the post-Archean average Australian Shale (PAAS, Nance and Taylor 1976) and the Early Proterozoic Greywackes (EP GREY, Condie 1993), demonstrating another evidence for a pelitic to semipelitic protolith. In the Eu/Eu* versus Gd_N/Yb_N diagram (Fig. 6E) khondalite samples plot on both fields of post-Archean metasediments and Archean Greenstone Sediments from McLennan & Taylor (1991) and McLennan et al. (1995) while the samples of Silva et al. (2014) plot within the range of post-

Archean sediments.

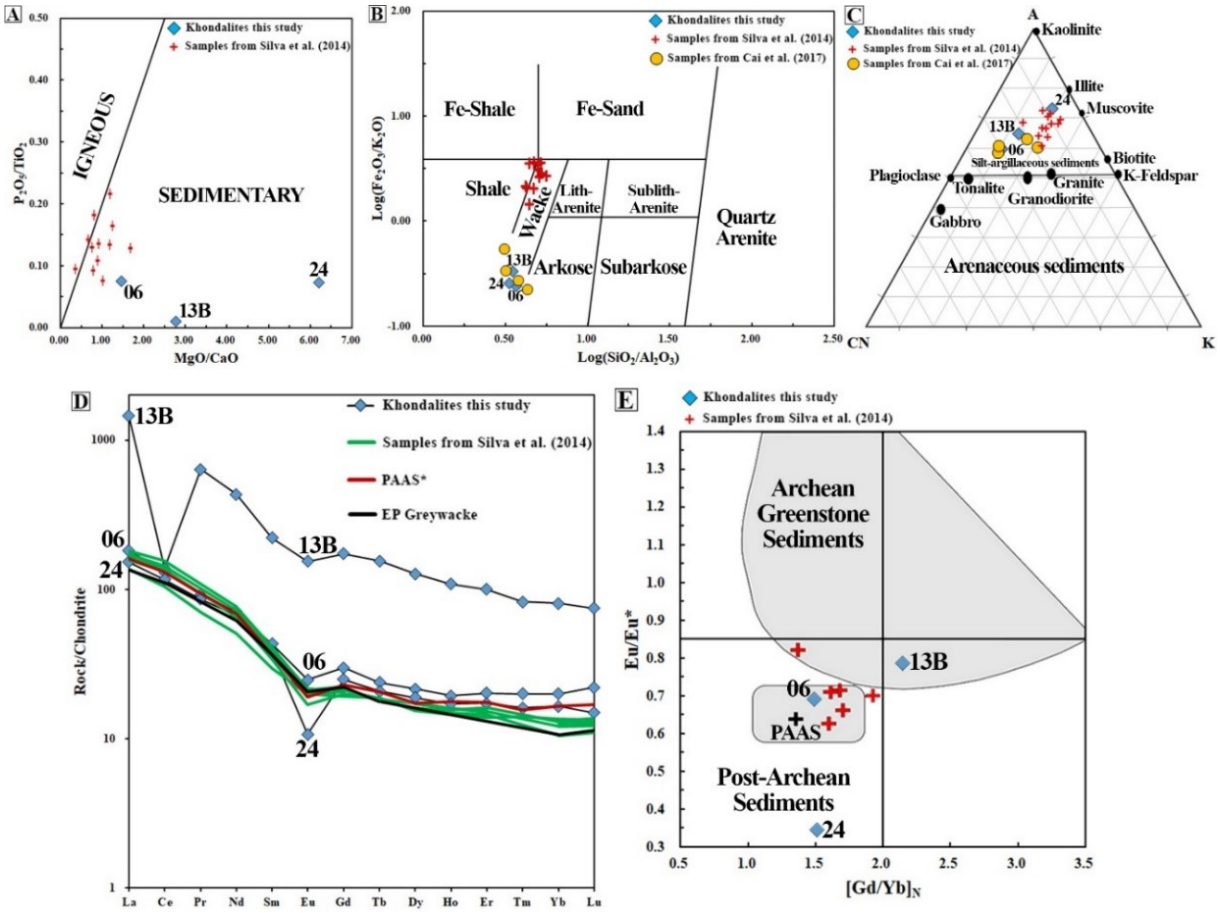

Figure 6. (A) P_2O_5/TiO_2 x MgO/CaO discrimination diagram of Werner (1987). (B) $Log(SiO_2/Al_2O_3)$ x $Log(Fe_2O_3/K_2O)$ classification diagram of Herron (1988). (C) A-CN-K ternary plot of Nesbitt and Young (1984). A = mol. Al_2O_3; CN = mol. CaO* + mol. Na_2O; K = mol. K_2O. The CaO* = mol. CaO - 3.33 mol. P_2O_5. (D) Chondrite normalized REE patterns from Sun and McDonough (1989) - black line represents Early Proterozoic average Greywacke (EP GREY) and red line post-Archean average Australian Shale (PAAS). (E) Eu/Eu* x Gd_N/Yb_N diagram (McLennan and Taylor 1991) - shadowed fields correspond to post-Archean Sediments and Archean Greenstone Sediments (McLennan et al. 1995).

For provenance and tectonic setting, in the diagram of Roser and Korsch (1988) the khondalite samples plot along the fields of quartzose sedimentary provenance and intermediate igneous provenance (Fig. 7A) and, in the diagram of Roser and Korsch (1986), the sediment deposition would have essentially occurred at an active continental margin setting (Fig. 7B).

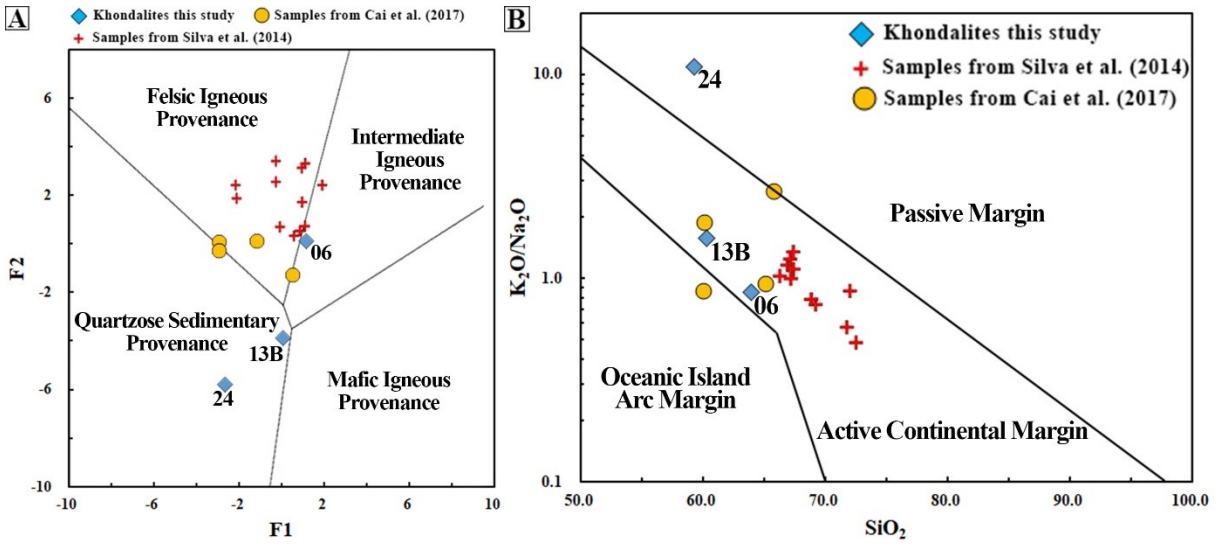

Figure 7. (A) Diagram of Roser and Korsch (1988), F1 = (-1.773TiO_2 + 0.607Al_2O_3 + 0.76Fe_2O_3t - 1.5 MgO + 0.616CaO + 0.509Na_2O - 1.224K_2O) - 9.09; F2 = (0.445TiO_2 + 0.07Al_2O_3 - 0.25Fe_2O_3t - 1.142MgO + 0.438CaO + 1.475Na_2O + 1.426K_2O) - 6.861. (B) K_2O/Na_2O x SiO_2 tectonic setting discrimination diagram of Roser and Korsch (1986).

Mineral Chemistry

The results of electron microprobe analyses of garnet, biotite, plagioclase and cordierite are listed in supplementary tables 2 to 5. Garnet general composition is almandine (70-79 % molar) (Supplementary Table 2), but it is possible to note that the X_{Fe} (X_{Fe} = $Fe^{2+}/(Fe^{2+}$ + Mg)) content in the core of the garnets are lower than the X_{Fe} content in the rims of garnet. As stated by Dallmeyer and Dodd (1971) and described by Cai et al. (2017) the rimward increase in Fe records late cation diffusion zoning from core to rim during the retrograde stage.

All biotite crystals form khondalite have a similar composition range for X_{Mg} (X_{Mg} = $Mg/(Mg + Fe^{2+})$) (0.44 to 0.62) and Ti (0.15 to 0.29 % molar) (Supplementary Table 3). The higher X_{Mg} from biotite included in garnet (0.56-0.62) than in the rim of garnet/cordierite (0.44-0.52) and in matrix (0.44-0.51) indicates that Fe-Mg exchange with garnet has occurred (Cesare et al. 2008).

Plagioclase from sample 06 have X_{An} = 15-25, while plagioclase from samples 13B and 24 are more calcic (X_{An} = 27-38) (Supplementary Table 4). According to Cai et al. (2017) the higher X_{An} (X_{An} = 0.38) from plagioclase in garnet rim of sample 24 than plagioclase in matrix (X_{An} = 0.36) occurs due the release of CaO during garnet breakdown reaction.

While sample 06 is cordierite, samples 13B and 24 are pinitizated cordierite due to

high contents of K_2O (Supplementary Table 5). In general the X_{Mg} adjacent to garnet (X_{Mg} = 0.68-0.64) is lower than in matrix (X_{Mg} = 0.65-0.84), reflecting Mg–Fe exchange (Cai et al. 2017).

Água Rasa metagranite

The Água Rasa metagranite surrounds khondalites, quartzites and graphite schists of the Itapecerica supracrustal succession unit, limiting them through the elliptical geophysical anomalies observed by high-density airborne gamma-ray spectrometric data (Fig. 3). Mineral orientation denoted especially by biotite marks an incipient foliation in this rock (Fig. 4C), which is coarse- to medium-grained with phaneritic texture and variable amounts of subhedral to anhedral plagioclase and K-feldspar. The main composition is quartz, microcline, plagioclase and biotite. Accessory minerals include mainly zircon, monazite, epidote, opaque minerals and rare amphibole (Fig. 8A-F). Quartz show features of recrystallization as formation of sub grains and interlobate grain boundaries (Fig. 8B, 8D). Plagioclase is usually altered to saussurite. Myrmekitic textures in the boundary with K-feldspar and quartz are observed (Fig. 8B, 8C, 8D, 8F) and perthitic textures are observed in some K-feldspar crystals (Fig. 8B, 8C, 8D, 8F). Biotite is the main mafic phase but reaches a maximum of 10% of modal values (Fig. 8A, 8F).

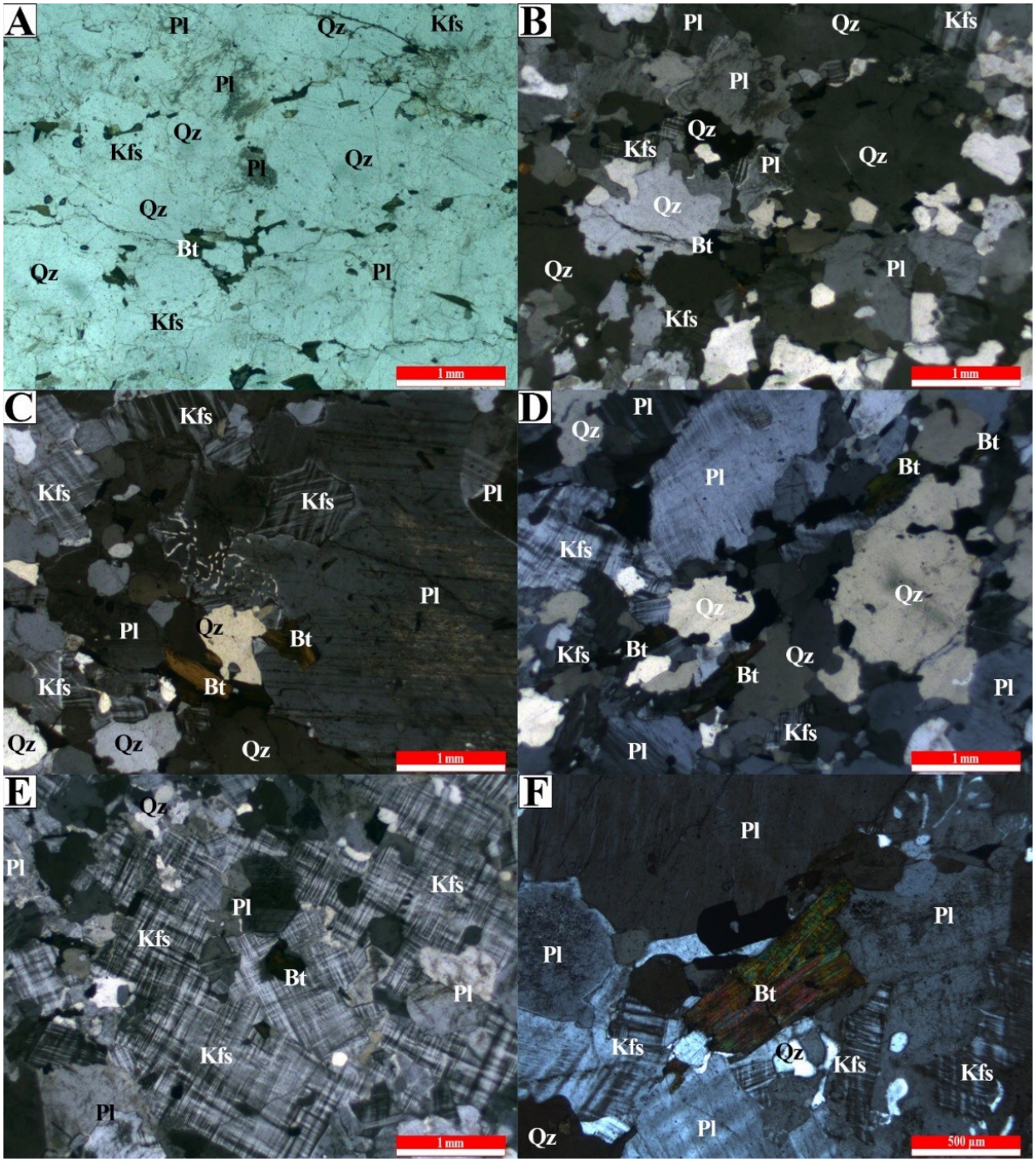

Figure 8. Photomicrographs (plane-polarized light, PPL; cross-polarized light, CPL) of representative mineral assemblages of the Água Rasa metagranite. (A) Photomicrograph (PPL) of the incipient foliation denoted by the biotite and elongated quartz. (B) Photomicrograph (CPL) of quartz showing features of recrystallization as formation of sub grains and interlobate grain boundaries. (C) Photomicrograph (CPL) of plagioclase showing saussuritization and myrmekites at rim. (D) Photomicrograph (CPL) showing the rare foliation, recrystallized quartz. (E) Photomicrograph (CPL) of a K-feldspar dominant portion with tartan texture. (F) Photomicrograph (CPL) of biotite. There are myrmekites at the boundary of plagioclase and K-feldspar. Mineral abbreviations are after Whitney and Evans (2010).

The results of whole-rock geochemistry for the Água Rasa metagranite are listed on the supplementary table 6. The Água Rasa metagranite protolith is classified as monzogranite according to the QAP modal diagram from Streckeisen (1974) (Fig. 9A). It is silica saturated

plotting in the granite field of Total Alkali vs Silica (TAS) diagram (Middlemost 1994) (Fig. 9B). It is calc-alkaline to alkali-calcic monzogranite with FeOt/(FeOt+MgO) ratios above 0.85 for SiO_2 > 75 wt%, ASI > 1.0 (0.99-1.11) (Fig. 9C) plotting on the peraluminous leucogranites field (n=90) (Frost et al. 2001) , while ranging between weak metaluminous to peraluminous (Fig. 9D) in Maniar and Piccoli (1989) plot. The REE patterns for Água Rasa metagranite, represented in a chondrite-normalized diagram (Sun and McDonough, 1989), show enrichment of LREE and negative anomalies of Eu ((Eu/Eu*) = 0.14-0.21) (Fig. 9E). Incompatible elements normalized to N-MORB (Normal mid-ocean ridge basalts) from Sun and McDonough (1989) display an enrichment in most incompatible elements (Fig. 9F). Negative anomalies are noticed for Nb, Ta, Zr, Hf and Eu. Tectonic discrimination diagrams indicate that the Água Rasa metagranite was formed in syn- to post-collisional setting (Fig. 9G, 9H).

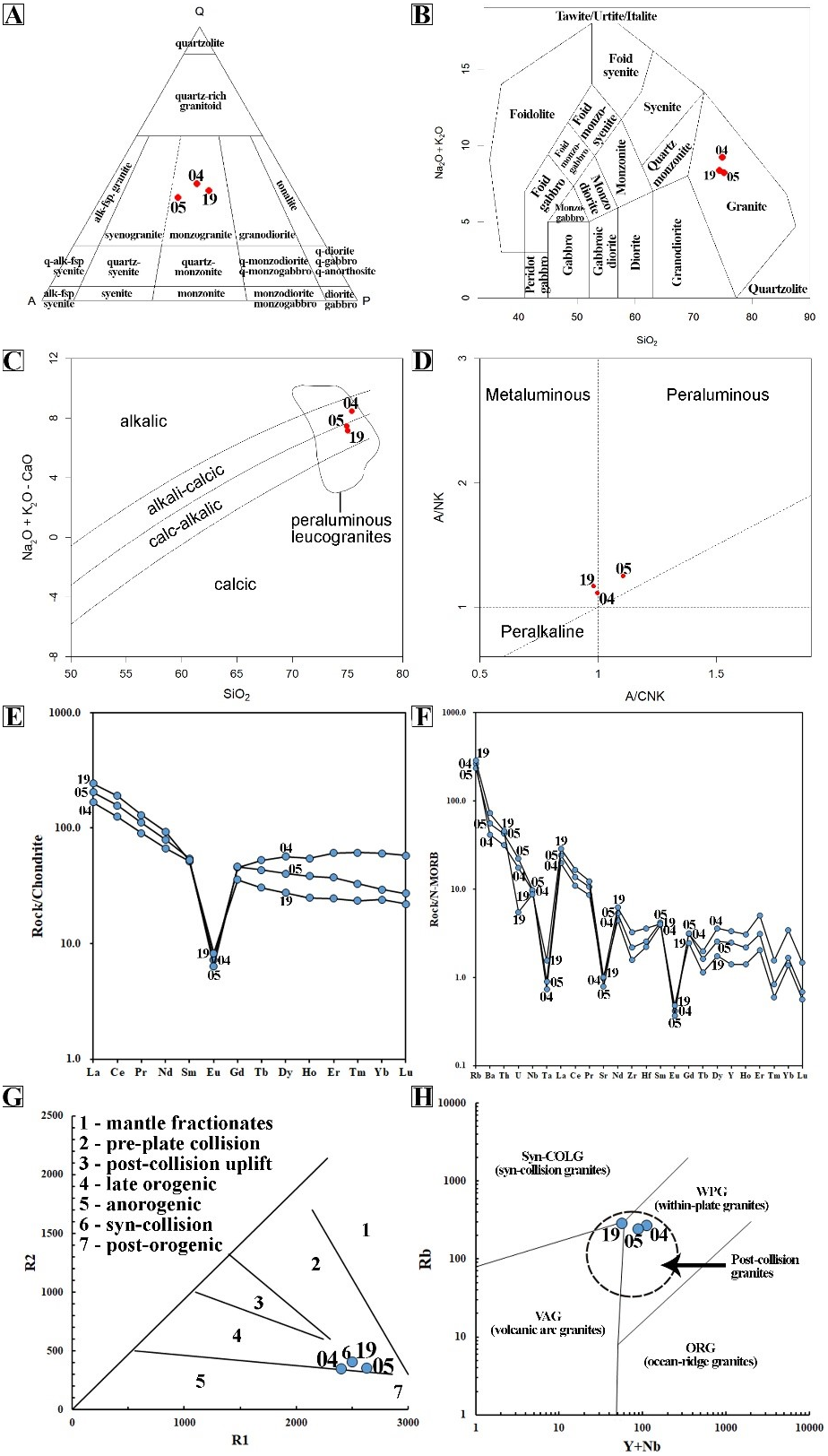

Figure 9. Lithochemical data from Água Rasa metagranite plotted on classification diagrams. (A) QAP modal diagram from Streckeisen (1974). (B) Total Alkalis versus Silica (TAS – Middlemost 1994). (C) $Na_2O + K_2O +$ CaO vs. SiO_2 (wt%) from Frost et al. (2001) (D) Diagram A/CNK-A/NK (Maniar and Piccoli, 1989). (E) Chondrite-normalized REE patterns from Sun and McDonough (1989). (F) Multi-elemental spider diagram normalized to N-MORB from Sun and McDonough (1989). (G) R1-R2 diagram (Batchelor and Bowden 1985). (H) Rb vs. Y+Nb tectonic diagram from Pearce (1996).

Zircon U-Pb and monazite U-Th-Pb$_T$ geochronology and whole-rock Sm-Nd and Rb-Sr

Zircon U-Pb and monazite U-Th-Pb$_T$ ages obtained in the study are presented in figures 10 and 11 and supplementary tables 7 and 8. The whole-rock Sm-Nd and Rb-Sr data are presented in the supplementary table 9.

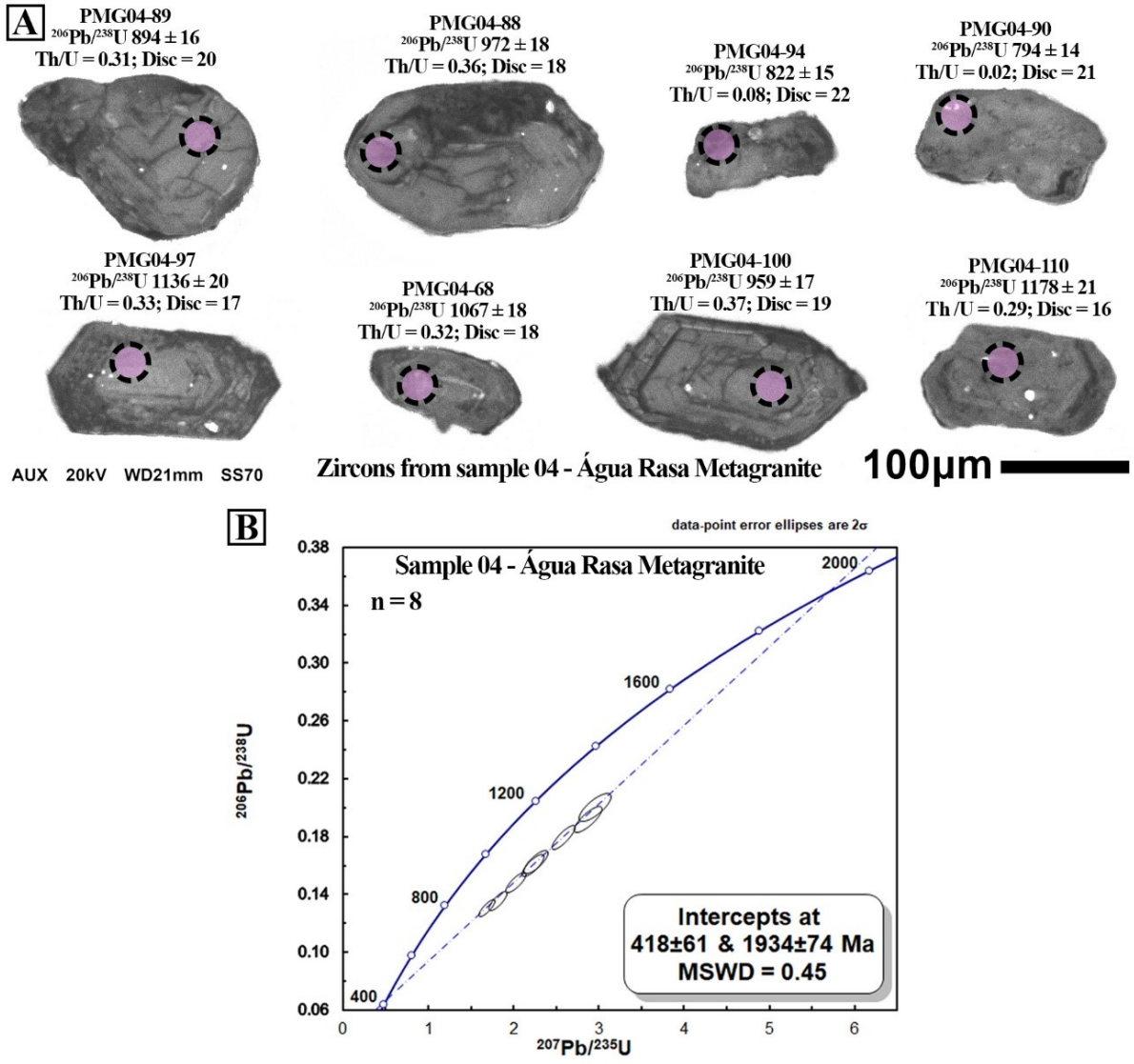

Figure 10. Cathodoluminescence (CL) images of zircons grains (A) and U-Pb Discordia diagram (B) for the Água Rasa metagranite.

Sample 04 – Água Rasa metagranite

Zircon crystals from Água Rasa metagranite range from 100 to 200 µm in size, with length to width ratios of 1:1 and 2:1 exhibiting morphology ranging from prismatic to subhedral and sometimes rounded to ovoid (metamorphic zircons). Zircon zoning is well developed and has internal fractures and metamorphic overgrowths; many grains are

metamictic and corroded (Fig. 10A). Eight spots (Supplementary Table 8) regressed to yield an upper intercept of 1934 ± 74 Ma and lower intercept of 418 ± 61 Ma with MSWD = 0.45 (Fig. 10B).

Monazite grains from the Água Rasa metagranite are subhedral, generally 50-100 µm in size with most being around 100 µm. BSE imaging indicates the presence of weakly zoned grains but the Yttrium (Y) map showed no zoning (Fig. 11A). Chemical data indicate that crystals are monazite-(Ce) (Supplementary Table 10). Eight spot analyses on a monazite grain from Água Rasa metagranite (Supplementary Table 8) yield two mean ages of 1941 ± 23 Ma (edge spots, 95% conf., MSWD = 1.07; probability = 0.36) and 2077 ± 24 Ma (core spots, 95% conf., MSWD = 0.21; probability = 0.89). In this grain, compositional domains of Yttrium were not observed (Fig. 11A).

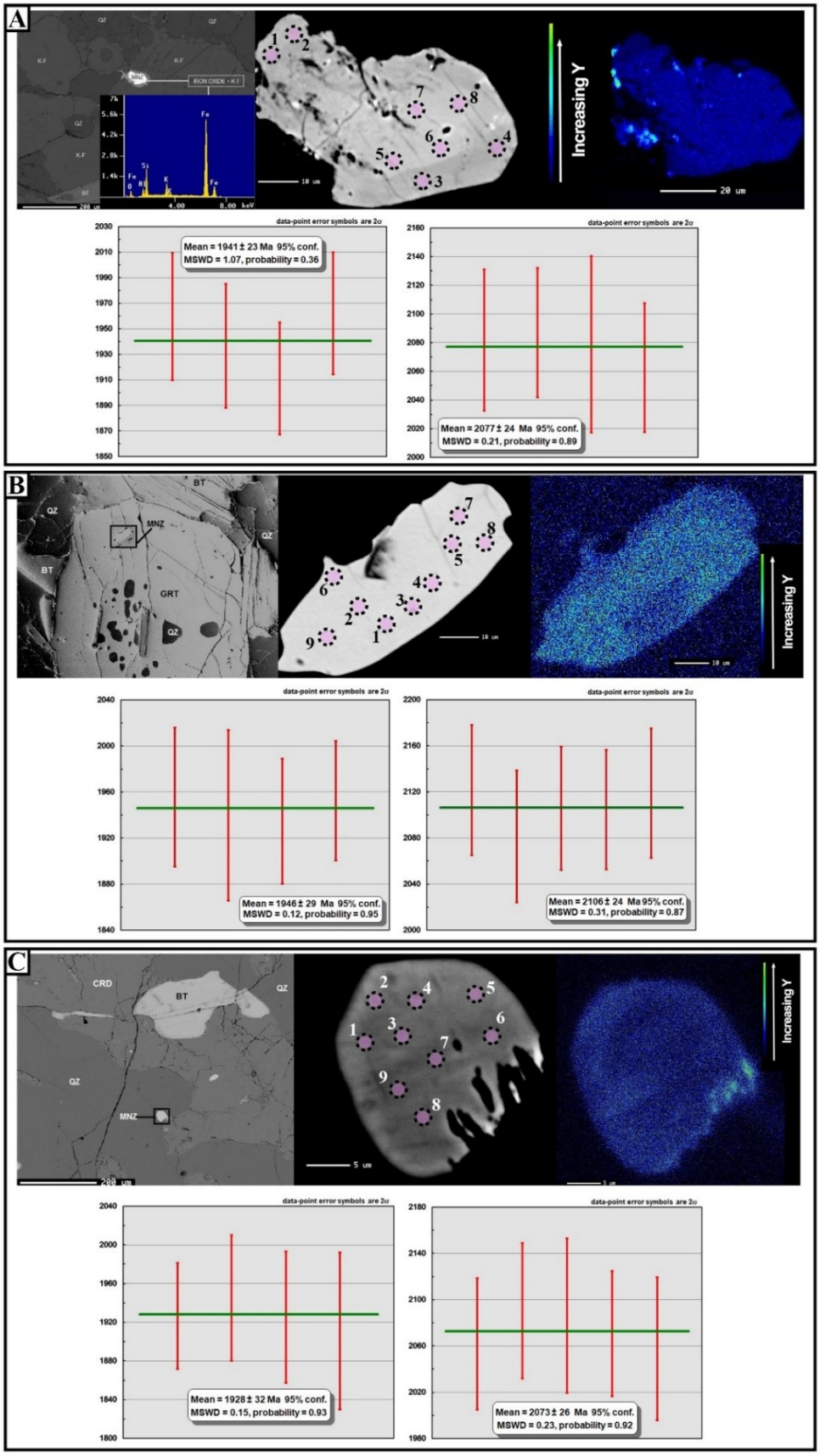

Figure 11. Backscatter electron images and Yttrium maps with respective U-Th-Pb_T mean ages from monazite crystals. (A) Água Rasa metagranite monazite. (B) Khondalite monazite in garnet. (C) Khondalite monazite in matrix.

The Sm-Nd whole-rock isotopic analyses from Água Rasa metagranite (Supplementary Table 9) yielded *f*Sm/Nd values between -0.28 and -0.30, which are compatible with crustal parameters for Nd fractionation (DePaolo, 1988). The intermediate values of $\varepsilon Nd_{(t)}$ (-0.5 to -2.7) suggest that the precursor magma of the Água Rasa metagranite had the contribution of different sources, one predominantly crustal with low Sm/Nd ratio and another juvenile mantelic with high Sm/Nd ratio. The high values of $^{87}Sr/^{86}Sr_{(t)}$ ratio (1.04-1.08) are usually explained by crustal anatexis, introducing radiogenic Sr derived from sedimentary rocks into the magma (Gazis et al. 1998) (Fig. 12). The T_{DM} ages ranged from 2.4 to 2.6 Ga for values calculated at age of 1950 Ma.

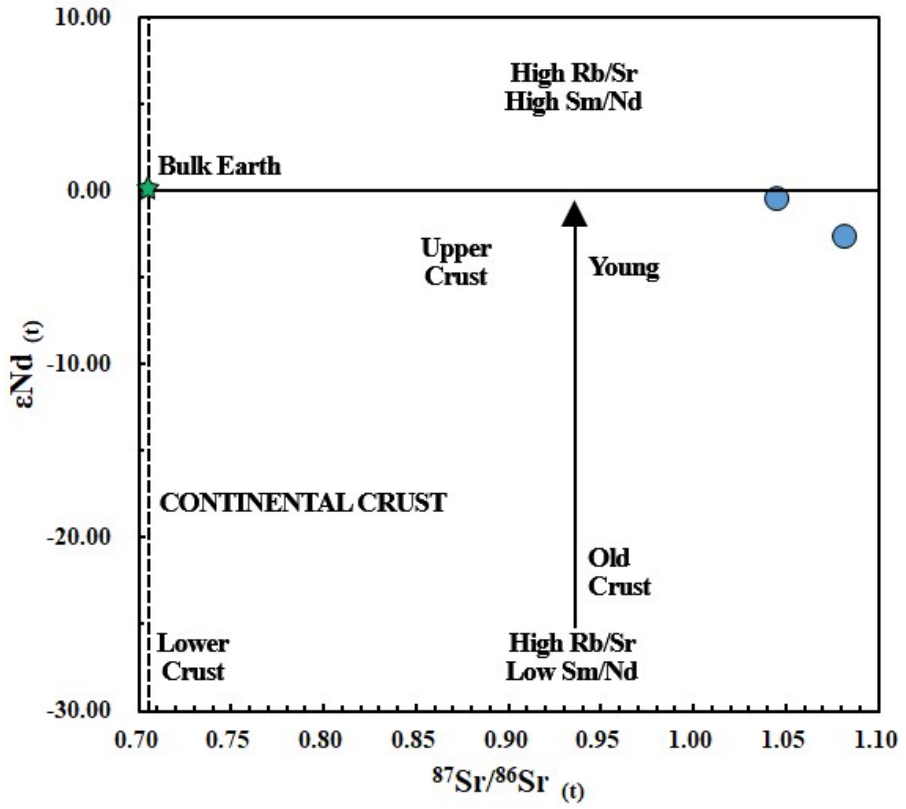

Figure 12. εNd(t) vs. Sr initial ratio; values calculated at 1950 Ma.

Sample 06 – Khondalite

Monazite grains from the khondalite are anhedral to subhedral, generally 20-100 µm in size with most being around 50 µm. BSE imaging indicates that the grains are internally homogeneous, non-zoned, but the Yttrium maps show zoning with variation in Y content (Figs. 11B, 11C). Chemical data indicate that crystals are monazite-(Ce) (Supplementary Table 10). Two monazites were analysed, one inside garnet (Fig 11B) and another in the rock matrix (Fig 11C).

On the monazite inside garnet nine spot analyses (Supplementary Table 10) being five with high Y_2O_3 content (Y_2O_3 higher than 0.23) and four with low Y_2O_3 content (Y_2O_3 below 0.23) yield, respectively, two mean ages of 1946 ± 29 Ma (95% conf., MSWD = 0.12; probability = 0.95) and 2106 ± 24 Ma (95% conf., MSWD = 0.31; probability = 0.87) (Fig. 11B).

On the monazite in the rock matrix nine spots analysis (Supplementary Table 10) being five with high Y_2O_3 content and four with low Y_2O_3 content yield, respectively, two mean ages of 1928 ± 31 Ma (95% conf., MSWD = 0.15; probability = 0.93) and 2073 ± 26 Ma (95% conf., MSWD = 0.23; probability = 0.92) (Fig. 11C).

P-T conditions

The individual bulk rock compositions of the khondalite gneiss (samples 06, 13B and 24) were used to calculate P–T pseudosections (Supplementary Table 1). For the sample 06, the identified mineral assemblage at metamorphic peak Liq + Pl ± Kfs + Grt + Bt + Ilm + Sil + Qz is stable between 680-770 ºC and 4.5-9.1 kbar (Fig. 13A – red field). Modeled garnet show compositional isopleth of Z_{Ca} (ZCa = Ca/(Ca + Fe2+ + Mg + Mn)) values ranging from 0.025 to 0.026 (Fig. 13B). The X_{Fe} isopleths for biotite 0.50-0.56 (Fig. 13B) show that P-T path led to the actual mineral paragenesis of the rock with Pl ± Kfs + Grt + Bt + Crd + Ilm + Sil + Qz after decompressional stage in the orogen collapse (Fig. 13A – yellow field) and together with garnet isopleth narrow the peak P-T conditions to 695-770 ºC and 5.4-7.4 kbar. In addition, it narrows the conditions of orogen collapse stage to 630-700 ºC and 3.3-4.5 kbar. The X_{Ca} (XCa = Ca/(Ca + Na + K)) isopleth for plagioclase of 0.19-0.25 show that it exists in all the range of modeled variables.

For the sample 13B, the identified mineral assemblage at metamorphic peak Liq + Pl ± Kfs + Grt + Bt +Ilm + Sil + Qz is stable between 710-775 ºC and 5.2-9.1 kbar (Fig. 13C – red field). Modeled garnet show compositional isopleth of Z_{Ca} values ranging from 0.027 to 0.036 (Fig. 13D). Plagioclase shows compositional isopleth of X_{Ca} ranging from 0.27-0.28 (Fig. 13D). The X_{Fe} isopleths for biotite 0.44-0.54 and X_{Fe} isopleths for cordierite 0.32-0.37 (Fig. 13D) show that P-T path led to the actual mineral paragenesis of the rock with Pl ± Kfs + Grt + Bt + Crd + Ilm + Sil + Qz after decompressional stage in the orogen collapse (Fig. 13C – yellow field). Garnet isopleth together with plagioclase isopleth narrow the P-T conditions of peak to 750-775 ºC and 6.2-8.1 kbar. In addition, the biotite isopleth together with the

cordierite isopleth narrow the conditions of orogen collapse stage to 620-720 ºC and 3.3-5.0 kbar.

For the sample 24, the identified mineral assemblage at metamorphic peak Liq + Pl ± Kfs + Grt + Bt +Ilm + Sil + Qz is stable between 685-770 ºC and 4.7-8.3 kbar (Fig. 13E – red field). Modeled garnet show compositional isopleth of Z_{Ca} values ranging from 0.039 to 0.064 (Fig. 13F). The X_{Fe} isopleths for biotite 0.38-0.53 (Fig. 13F) and X_{Fe} isopleths for cordierite 0.31-0.35 in combination with garnet isopleth show that P-T path led to the actual mineral paragenesis of the rock with Pl ± Kfs + Grt + Bt + Crd + Ilm + Sil + Qz after decompressional stage in the orogen collapse (Fig. 13E – yellow field). Garnet isopleth together with biotite isopleth narrow the P-T conditions of peak to 700-770 ºC and 4.8-7.0 kbar. In addition, the biotite isopleth together with the cordierite isopleth narrow the conditions of orogen collapse stage to 630-715 ºC and 3.2-4.7 kbar.

The melt contours for the samples (Fig. 13A, 13C, 13E) indicate that 15-17% of melt can be produced by the time terminal biotite stability is exceeded. According to Cai et al. (2017) this indicates that has occurred substantial melt loss under near-peak conditions, and White and Powell (2002) proposes that the loss of early low-temperature melts would result in less melt production at higher temperatures.

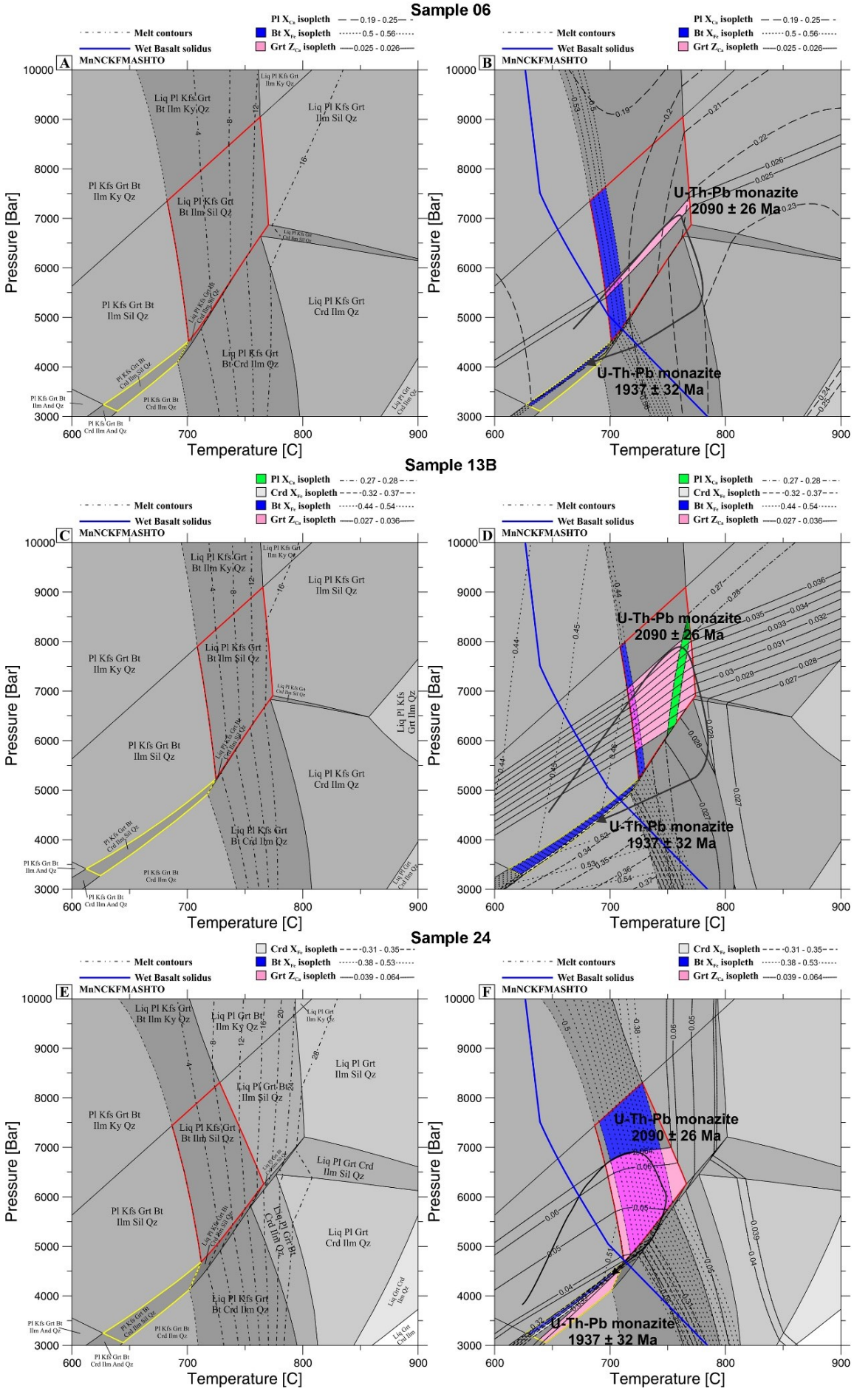
Sample 06
Sample 13B
Sample 24
A
B
C
D
E
F
MnNCKFMASHTO
Melt contours
Wet Basalt solidus
Pl X$_{Ca}$ isopleth
Bt X$_{Fe}$ isopleth
Grt Z$_{Ca}$ isopleth
Crd X$_{Fe}$ isopleth
0.19 - 0.25
0.5 - 0.56
0.025 - 0.026
0.27 - 0.28
0.32 - 0.37
0.44 - 0.54
0.027 - 0.036
0.31 - 0.35
0.38 - 0.53
0.039 - 0.064
U-Th-Pb monazite
2090 ± 26 Ma
U-Th-Pb monazite
1937 ± 32 Ma
Pressure [Bar]
Temperature [C]
Liq Pl Kfs Grt Bt Ilm Ky Qz
Liq Pl Kfs Grt Ilm Sil Qz
Pl Kfs Grt Bt Ilm Ky Qz
Liq Pl Kfs Grt Bt Ilm Sil Qz
Pl Kfs Grt Bt Ilm Sil Qz
Liq Pl Kfs Grt Crd Ilm Qz
Liq Pl Kfs Grt Bt Crd Ilm Qz
Pl Kfs Grt Bt Crd Ilm Qz
Pl Kfs Grt Bt Crd Ilm And Qz
Pl Kfs Grt Bt Ilm And Qz
Liq Pl Kfs Grt Ilm Qz
Liq Pl Kfs Grt Bt Ilm Qz
Liq Pl Kfs Grt Crd Ilm Sil Qz
Liq Pl Kfs Grt Bt Crd Ilm Sil Qz
Liq Pl Kfs Grt Bt Ilm Sil Qz
Liq Pl Kfs Grt Bt Crd Ilm Sil Qz
Liq Pl Kfs Grt Bt Crd Ilm And Qz
Liq Pl Kfs Grt Bt Ilm And Qz
Liq Pl Kfs Grt Ilm Qz
Liq Pl Kfs Grt Bt Ilm Qz
Liq Pl Kfs Grt Crd Ilm Sil Qz
Liq Pl Kfs Grt Bt Crd Ilm Sil Qz
Liq Pl Kfs Grt Bt Ilm Sil Qz
Liq Pl Kfs Grt Bt Crd Ilm Sil Qz
Liq Pl Kfs Grt Bt Crd Ilm And Qz
Liq Pl Kfs Grt Bt Ilm And Qz
Liq Pl Kfs Grt Ilm Qz
Liq Pl Kfs Grt Bt Ilm Qz
Liq Pl Grt Bt Ilm Ky Qz
Liq Pl Grt Ilm Ky Qz
Liq Pl Grt Ilm Sil Qz
Liq Pl Grt Bt Ilm Sil Qz
Liq Pl Grt Crd Ilm Sil Qz
Liq Pl Grt Bt Crd Ilm Qz
Liq Pl Grt Crd Ilm Qz
Liq Grt Crd Ilm Qz
Liq Grt Crd Ilm
Liq Pl Grt Bt Crd Ilm Qz
Liq Pl Kfs Grt Bt Crd Ilm Qz
Pl Kfs Grt Bt Crd Ilm And Qz
Pl Kfs Grt Bt Ilm And Qz

Figure 13. Calculated P-T pseudosections for the khondalite samples 06, 13B and 24, by using whole-rock composition (Supplementary Table 1). (A) P-T fields of peak assemblage for sample 06: Liq+Pl±Kfs+Grt+Bt+Ilm+Sil+Qz (bold red field) and orogen collapse assemblage: Pl±Kfs+Grt+Bt+Crd+Ilm+Sil+Qz (bold yellow field). (B) Plot of compositional isopleths of Grt Z_{Ca}, Bt X_{Fe} and Pl X_{Ca} isopleths for sample 06. (C) P-T fields of peak assemblage for sample 13B: Liq+Pl±Kfs+Grt+Bt+Ilm+Sil+Qz (bold red field) and orogen collapse assemblage: Pl±Kfs+Grt+Bt+Crd+Ilm+Sil+Qz (bold yellow field). (D) Plot of compositional isopleths of Grt Z_{Ca}, Pl X_{Ca}, Bt X_{Fe} and Crd X_{Fe} isopleths for sample 13B. (E) P-T fields of peak assemblage for sample 24: Liq+Pl±Kfs+Grt+Bt+Ilm+Sil+Qz (bold red field) and orogen collapse assemblage: Pl±Kfs+Grt+Bt+Crd+Ilm+Sil+Qz (bold yellow field). (F) Plot of compositional isopleths of Grt Z_{Ca}, Bt X_{Fe} and Crd X_{Fe} isopleths for sample 24. Monazite U-Th-Pb_T ages represent mean khondalite ages. Wet basalt solidus (blue curve) from Lambert and Wyllie (1972).

Discussion

The reactions between the minerals along with the microstructures and the mineral assemblages in the khondalite indicate that the metamorphic evolution was complex with a peak-stage metamorphism involving melt-producing reactions followed by decompression with melt-consuming reactions and orogen collapse assemblages.

In all samples the calculated K-feldspar volume is around 1%, and probably this amount is lost due to reversal reaction of biotite-melting dehydration, it is also possible that potassium, as an active element, is incorporated into melt and extracted by segregation, resulting in the lack of K-feldspar, so in thin section no K-feldspar was found.

Petrographic evidences show that the producing melt last through the peak and post-peak metamorphism and is consumed due to back reactions between mineral phases and in situ crystallizing melt on microdomains.

The diagrams of provenance and tectonic settings suggest that the sedimentary basin that was metamorphosed to become the khondalite has received contribution from different sources with pelitic to wacke sediments and it was formed at an active continental margin setting.

Monazite U-Th-Pb_T geochronology from khondalite show mean ages of 2090 ± 26 Ma and 1937 ± 32 (Fig. 11B, 11C). The older age is interpreted as crystallization of the monazite during the metamorphic peak of the Itapecerica supracrustal succession rocks accompanied by tectonic exhumation of the orogen. The younger one is the age of the orogen collapse stage observed in thin sections and mineral assemblage reactions (Fig. 5; Fig. 13), resetting the U-Th-Pb system in monazite during the orogenic collapse. From the mineral assemblages observed in thin sections (Fig. 5) and the pseudosections calculated (Fig. 13), the P-T-t path

of all three khondalite samples was clockwise with an orogen collapse (bold yellow field; Fig. 13) after decompressional stage and metamorphic peak (bold red field; Fig.13).

The P-T conditions of metamorphic peak by pseudosections reached average 715-772 ºC and 5.5-7.5 kbar while the orogen collapse stage reduced the conditions of P-T to average 627-712 ºC and 3.2-4.7 kbar. It is close to the temperature found by Miranda and Chaves (2019) around 729 ºC analyzing the graphite from Itapecerica supracrustal succession rocks and nearby the P-T conditions of peak at 830-860 ºC and 9.5-11 kbar found by Cai et al. (2017) on similar rocks of similar metamorphism age (~ 1.95 Ga) in the Wulashan Complex on North China Craton.

The monazite 2077 ± 24 Ma older age of the Água Rasa metagranite (Fig. 11A) seems to point to initial melting generation promoted by crustal thickening followed by tectonic exhumation during metamorphic peak. The monazite 1941 ± 23 Ma younger age (Fig. 11A) and the upper intercept 1934 ± 74 Ma age obtained from zircon of the Água Rasa metagranite (Fig. 10B) are similar. Although discordant, zircon ages of the Água Rasa metagranite plotted only a discordia. This age around 1941 Ma for the Água Rasa metagranite is similar to that of younger monazite age from khondalite. Based on this younger age, the final crystallization of the Água Rasa metagranite matches with the orogen collapse-related decompressional stage recorded by the monazite from the khondalite. Geochemical data showed that the Água Rasa metagranite formed during syn- to post-collisional setting (Fig. 9G, 7H) and cross-cutting observations (Fig. 4D) seem to confirm this. The differences between the Y_2O_3 content from the monazites of the khondalite (Y_2O_3 - 0.16 to 0.38 - Supplementary Table 10)* and the monazite form the Água Rasa metagranite (Y_2O_3 - 2.68 to 2.90) seem to indicate that during the anatexis of the khondalite the Yttrium, as an incompatible element, goes to the melt and is incorporated during the crystallization of the monazites from the Água Rasa metagranite. *See explanatory note after Acknowledgments.

High-grade metapelitic rocks commonly develop partial melting (Sawyer 2012; Kriegsman 2001). The presence of peraluminous metagranitoid that surrounds the Itapecerica khondalitic rocks suggest that this peraluminous metagranitoid may be derived from partial melting of the high-grade metamorphosed Itapecerica khondalites. However, $\varepsilon Nd_{(t)}$ and $^{87}Sr/^{86}Sr_{(t)}$ data (Supplementary Table 9, Fig. 12) indicate that the precursor magma of the Água Rasa metagranite originated from anatexis of the Itapecerica supracrustal succession (crustal source) and associated amphibolites (mantle source) (Fig. 3) during the crustal

thickening followed by tectonic exhumation at peak metamorphism and at decompressional stage during the orogenic collapse. In the metamorphic P-T path, Itapecerica supracrustal succession rocks surpassed the wet granite solidus curve (Huang and Wyllie 1973) and wet basalt solidus curve (Lambert and Wyllie 1972) (Fig. 13), making khondalite and amphibolite partial melting possible. It is possible that there are large amount of more high-grade supracrustal rocks with higher temperatures beneath the surface to generate these metagranites. Such amphibolite- metasedimentary rocks association suggest an ocean-floor basin setting before metamorphism. Nb, Ta and Zr negative anomalies of the Água Rasa metagranite are indicators of crustal contamination brought by metasedimentary rocks melting contribution (Winter 2001).

The similarities between the khondalite rocks of this study and khondalites of the North China Craton, such as related mineral paragenesis and reactions, same provenance, tectonic setting, depositional age, nearby P-T conditions and metamorphism age suggest a potential genetic correlation of these rocks. Nevertheless, diachronism in sedimentary deposition and metamorphism between both cratons in Paleoproterozoic could explain different age and metamorphic intensities. In addition, they are compatible with the recent attempts (Teixeira et al. 2017a; Chaves and Rezende 2019) to reconstruct the Columbia supercontinent, which place the São Francisco-Congo Craton near the North China Craton. Based on paleomagnetic data the figure 14 shows the probable zone of similar occurrences of khondalite belts in the São Francisco Craton and the North China Craton.

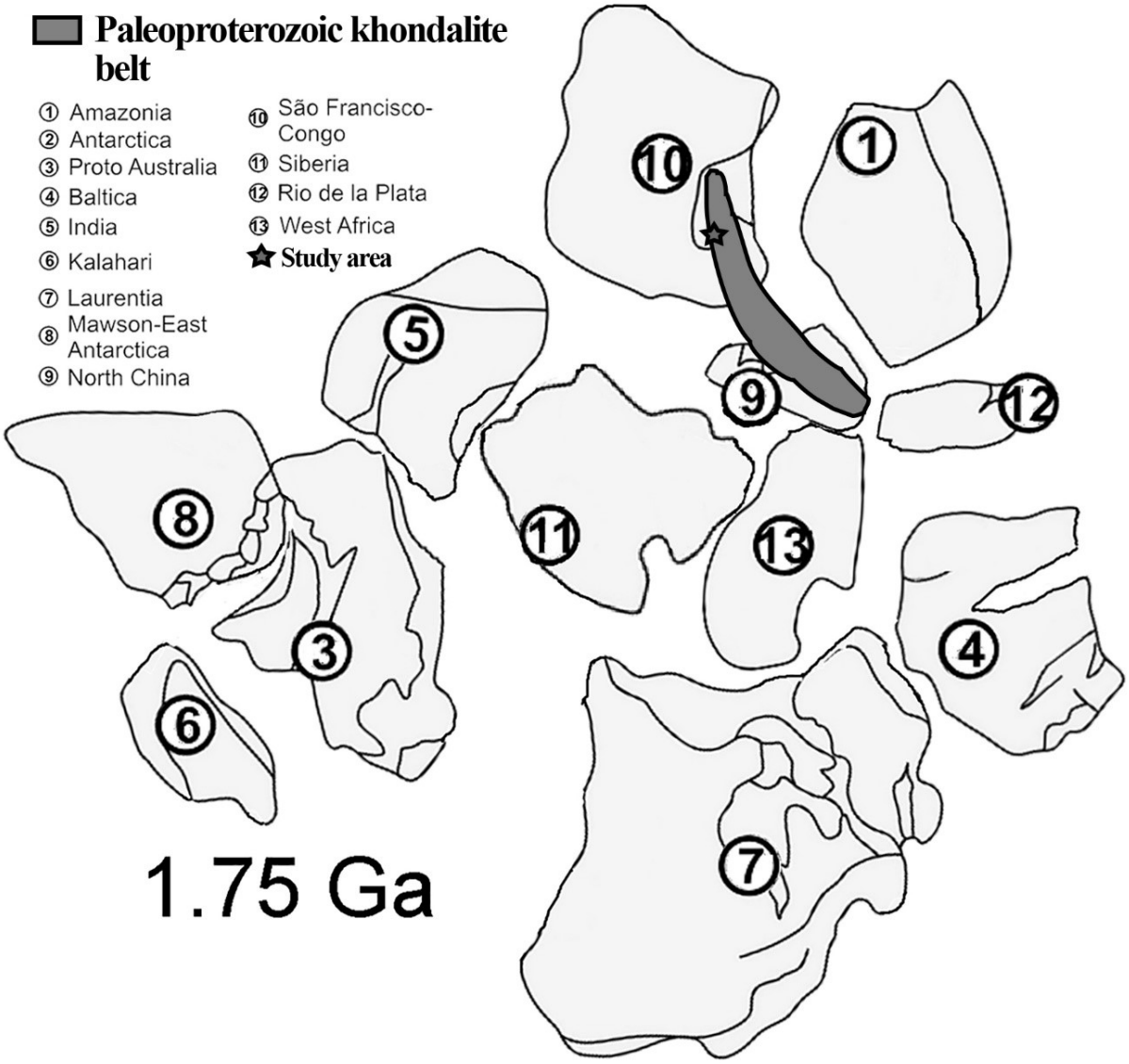

Figure 14. Configuration of the supercontinent referred to as Columbia (Nuna) based on paleomagnetism, with probable khondalite belt zone. Modified from Chaves and Rezende (2019).

Conclusions

The Água Rasa metagranite surrounding khondalitic rocks in Itapecerica region was originated from anatexis of the Itapecerica supracrustal succession rocks and associated amphibolites. Melting started due to tectonic exhumation during metamorphic peak under 715-772 ºC and 5.5-7.5 kbar around 2090 Ma to 2077 Ma (monazite ages from khondalite and metagranite) and proceeded due to decompressional stage during orogenic collapse of the regional Rhyacian-Orosirian orogeny under P-T conditions of 627-712 ºC and 3.2-4.7 kbar around 1941 Ma. Khondalites keep the peak metamorphic assemblage: liquid + plagioclase ± K-feldspar + garnet + biotite + ilmenite + sillimanite + quartz formed under 715-772 ºC and 5.5-7.0 kbar around 2090 ± 26 Ma (monazite ages from Khondalite). Whole-rock

geochemical data for these rocks suggest that the precursor sediments had mixed pelitic-wacke compositions resulting from erosion of different sources. Sediment deposition would have occurred at an active continental marginal setting. The similarities between the khondalite rocks of this study and of the North China Craton suggest that the São Francisco-Congo Craton was near the North China Craton in the supercontinent Columbia for the 2.1–1.9 Ga period, as summarized in the table 2.

Table 2 – Comparison between khondalite rocks of this study and of the North China Craton.

		Itapecerica Khondalites	**Wulashan Complex Khondalites (North China) (Cai et al. 2017)**	**Água Rasa metagranite**
Petrography		Sil-Crd-Grt-Bt-Pl-Qz with acessory Mnz-Zrn-Ilm	Grt-Bt-Crd-Sil-Kfs-Pl-Qz with acessory Rt-Mag-Ilm	Bt-Pl-Kfs-Qz with acessory Zrn-Mnz-Ep-Opq-Amp
T (°C)	**peak**	715-768	830-860	-
P (Kbar)		5.5-7.5	9.5-11	
T (°C)	**post-peak**	648-712	840-880	
P (Kbar)		3.6-4.7	6.0-7.5	
Age	**U-Th-Pb$_T$ monazite**	2090 ± 26 Ma (peak metamorphism/tectonic exhumation)	-	2077 ± 24 Ma
		1937 ± 32 Ma (post-peak/orogen collapse)		1941 ± 23 Ma
	U-Pb zircon	-	1.95-1.92 Ga (U-Pb metamorphic zircon)	1934 ± 74 Ma (U-Pb metamorphic zircon)
Sm-Nd		-	-	$\varepsilon Nd_{(t)}$ (-0.5 to -2.7) / T_{DM} ages 2.4 to 2.6 Ga.
Rb-Sr		-	-	$^{87}Sr/^{86}Sr_{(t)}$ ratio (1.04-1.08)
Protolith setting		Active continental margin	Active continental margin	Anatexis from Khondalites and Amphibolies
Protolith depositional age		Max. ~2080 Ma	2300-2000 Ma	-

Acknowledgments: To the Nacional de Grafite Company, the geologist Lairton de Oliveira and geology supervisor Gilson dos Santos. This study was financed in part by the Coordenação de Aperfeiçoamento de Pessoal de Nível Superior - Brasil (CAPES) - Finance Code 001. The second author thanks to CNPq the research productivity grant and to FAPEMIG for research support through the project APQ-00654-16.

***Explanatory Note:**

The correct Y_2O_3 content from the monazites of the khondalite varies from 0.12 to 0.38 not 0.16-0.38 as stated on the discussions (Supplementary Table 10).

References

Abu El-Enen, M.M., 2011, Geochemistry, provenance, and metamorphic evolution of Gabal Samra Neoproterozoic metapelites, Sinai, Egypt. Journal of African Earth Sciences, v. 59, p. 269-282.

Alkmim, F.F., Marshak, S., 1998, Transamazonian Orogeny in the Southern São Francisco Craton Region, Minas Gerais, Brazil: evidence for Paleoproterozoic collision and collapse in the Quadrilátero Ferrífero. Precambr. Res., v. 90, p. 29-58.

Ávila, C.A., Teixeira, W., Bongiolo, E.M., Dussin, I.A., Vieira, T.A.T., 2014, Rhyacian evolution of subvolcanic and metasedimentary rocks of the southern segment of the Mineiro belt, São Francisco Craton, Brazil. Precambrian Res., v. 243, p. 221-251.

Batchelor, R.A., Bowden, P., 1985, Petrogenetic Interpretation of Granitoid Rock Series Using Multicationic Parameters. Chemical Geology, v. 48, p. 43-55.

Baltazar, O.F., Zucchetti, M., 2007, Lithofacies associations and structural evolution of the Archean Rio das Velhas greenstone belt, Quadrilátero Ferrífero, Brazil: a review of the setting of gold deposits. Ore Geol. Rev., v. 32, p. 471-499.

Barbosa, J.S.F., Sabaté, P., 2004, Archean and Paleoproterozoic crust of the São Francisco Craton, Bahia, Brazil: geodynamic features. Precambrian Research, v. 133, p. 1-27.

Barbosa, J.S.F., 2006, Field Trip 1 The Paleoproterozoic Orogenic domain of Eastern Bahia. Day 6, from Jiquiriçá to Jequié. In: Alkmim, F.F., Noce, C.M., (eds.) 2006, The Paleoproterozoic Record of the São Francisco Craton. IGCP 509 Field workshop, Bahia and Minas Gerais, Brazil. Field Guide & Abstracts, 114 p.

Barbosa, J.S.F., Nicollet, C., Leite, C., Kienast, J.R., Fuck, R.A., Macedo, E.P., 2006, Hercynite–quartz-bearing granulites from Brejões Dome area, Jequié Block, Bahia, Brazil: Influence of charnockite intrusion on granulite facies metamorphism. Lithos, v. 92, p. 537-556.

Barbosa, N.S., Teixeira, W., Ávila, C.A., Montecinos, P.M., Bongiolo, E.M., 2015, 2.17–2.10 Ga plutonic episodes in the Mineiro belt, São Francisco Craton, Brazil: U-Pb ages, geochemical constraints and tectonics. Precambr. Res., v. 270, p. 204-225.

Botelho, N.F., Fuck, R.A., Dantas, E.L., Laux, J.H., Junges, S.L., 2006, The Paleoproterozoic peraluminous Aurumina granite suite, Goiás and Tocantins, Brazil: geological, whole rock geochemistry and U-Pb and Sm-Nd isotopic constraints. In: Alkmim, F.F., Noce, C.M., (eds.) 2006, The Paleoproterozoic Record of the São Francisco Craton. IGCP 509 Field workshop, Bahia and Minas Gerais, Brazil. Field Guide & Abstracts, 114 p.

Campello, M.S., Vaz, B.B., Oliveira, M.A.S., Ávila, M.A.C., 2015, Relatório e mapa geológicos 1:100.000 da Folha Formiga SF.23-V-B-III. Projeto Fortaleza de Minas, CODEMIG/UFMG. A.C. Pedrosa Soares (coord.). 62 p.

Cai, J., Liu, F.L., Liu, P.H., Liu, C.H.,Wang, F., Shi, J.R., 2014, Metamorphic P-T path and tectonic implications of pelitic granulites from the Daqingshan Complex of the Khondalite Belt, North China Craton. Precambr. Res., v. 241, p. 161-184.

Cai, J., Liu, F., Liu, P., Wang, F., Liu, C., Shi, J., 2017, Anatectic record and P–T path evolution of metapelites from the Wulashan Complex, Khondalite Belt, North China Craton. Precambr. Res., v. 303, p. 10-29.

Campos, J.C.S., Carneiro, M.A., 2008, Neoarchean and Paleoproterozoic granitoids marginal to the Jeceaba-Bom Sucesso lineament (SE border of the southern São Francisco craton): genesis and tectonic evolution. J. S. Am. Earth Sci., v. 26, p. 463-484.

Carneiro, M.A., Barbosa, M.S.C., 2008. Implicações geológicas e tectônicas da interpretação magnetométrica da região de Oliveira, Minas Gerais. Revista Brasileira de Geofísica, v. 26, n. 1, p. 87-98.

Carneiro, M.A., Nalini Júnior, H.A., Endo, I., Suita, M.T.F., Castro, P.T.A., Barbosa, M.S.C., Campos, J.C.S., Goulart, L.E.A., Silva, E.F.S., Pereira, A.A., Tavares, T.D., Jiamelaro, F., Carneiro, J.M., Mariano, L.C., Miguel, F.P., Silva Junior, A.C., Barbosa, A.S., Prado, G.E.A., Santos, C., Urbano, E.E.M.C., 2007, Folha Campo Belo- SF.23-V-B-VI, escala 1:100.000: nota explicativa integrada com Oliveira. UFOP/CPRM, Minas Gerais, 114 p.

Carvalho, B.B., Sawyer, E.W., Janasi, V.A., 2016, Crustal reworking in a shear zone: transformation of metagranite to migmatite. J. Metamorph. Petrol., v. 34, p. 237-264.

Carvalho, B.B., Janasi, V.A., Sawyer, E.W., 2017, Evidence for Paleoproterozoic anatexis and crustal reworking of Archean crust in the São Francisco Craton, Brazil: a dating and isotopic study of the Kinawa migmatite. Precambrian Res., v. 291, p. 98-118.

Cesare, B., Satish-Kumar, M., Cruciani, G., Pocker, S., Nodari, L., 2008, Mineral chemistry of Ti-rich biotite from pegmatite and metapelitic granulites of the Kerala Khondalite Belt (southeast India): petrology and further insight into titanium substitutions. Am. Mineral. v. 93, p. 327-338.

Chaves, A.O., 2013, Enxames de diques máficos de Minas Gerais – o estado da arte. Geonomos, v. 21, n. 1, p. 29-33.

Chaves, A.O., Oliveira, E.K., Garcia, L.R.A., 2013, Desenvolvimento do método de datação química U-Th-Pb de monazita por microssonda eletrônica na UFMG. Geonomos, v. 21, n. 2, p. 13-18.

Chaves, A.O., Campello, M.S., Soares, A.C.P., 2015, Idade U-Th-Pb_T de monazitas do sillimanita-cordierita-granada-biotita gnaisse de Itapecerica (MG) e a atuação da orogenia Riaciano-Orosiriana no interior do Cráton São Francisco Meridional. Geociências, v. 34, n. 3, p. 324-334.

Chaves, A.O., Rezende, C.R., 2019, Fragments of 1.79-1.75 Ga Large Igneous Provinces in reconstructing Columbia (Nuna): a Statherian supercontinent-superplume coupling? Episodes, v. 24, n. 1, p. 55-67.

Condie, K.C., 1993, Chemical composition and evolution of the upper continental crust: Contrasting results from surface samples and shales. Chemical Geology, v. 104, p. 1-37.

CPRM, Serviço Geológico do Brasil and CODEMIG, Companhia de Desenvolvimento Econômico de Minas Gerais, 2014, Mapa Geológico do Estado de Minas Gerais, Escala 1:1.000.000. DVD-Rom.

Cuadros, F.A., Botelho, N.F., Fuck, R.A., Dantas, E.L., 2017, The peraluminous Aurumina Granite Suite in central Brazil: An example of mantle-continental crust interaction in a Paleoproterozoic cordilleran hinterland setting? Precambrian Research, v. 299, p. 75-100.

Dallmeyer, R.D., Dodd, R.T., 1971, Distribution and significance of cordierite in paragneisses of the Hudson Highlands, Southeastern New York. Contrib. Miner. Petrol. v. 33, p. 289-308.

De Capitani, C., Petrakakis, K., 2010, The computation of equilibrium assemblage diagrams with Theriak/Domino software. American Mineralogist, v. 95, p. 1006-1016.

Delgado, I.M., Neves, J.P., Filho, O.M., Bomfim, L.F.C., Oliveira, J.E., Gomes, P.J.P., Motta, A.C., Filho, N.C.S., 1988, Projeto Mapas Metalogenéticos e de Previsão de Recursos Minerais Folhas SD.24-Y-D Itapetinga e SD.24-Z-C Canavieiras Escala 1:250.000 Volume I Texto e Mapas. Companhia de Pesquisa e Recursos Minerais CPRM, Superintendência regional de Salvador. 113 p.

DePaolo, D.J., 1988, Neodymium Isotope Geochemistry: An Introduction. Springer, Berlin, 187 p.

Dorr, J.V.N., 1969, Physiographic, stratigraphic and structural development of Quadrilatero Ferrifero, Minas Gerais, Brazil. USGS/DNPM, Professional paper 641-A, 110 p.

Farina, F.A., Albert, C., Lana, C., 2015, The Neoarchean transition between medium and high-K granitoids: clues from the Southern São Francisco Craton (Brazil). Precambrian Res., v. 266, p. 375-394.

Fernandes, R.A., Carneiro, M.A.O., 2000, Complexo Metamórfico Campo Belo (Craton São Francisco Meridional): unidades litodêmicas e evolução tectônica. Revista Brasileira de Geociencias, v.30, n. 4, p. 671-678.

Frost, B.R., Barnes, C.G., Collns, W.J., Arculus, R.J., Ellis, D.J., Frost, C.D., 2001, A geochemical classification for granitic rocks. J. Petrology, v. 42, p. 2033-2048.

Fuck, R.A., Dantas, E.L., Pimentel, M.M., Botelho, N.F., Laux, J.H., Junges, S.L., 2006, Paleoproterozoic Crust Forming Events in the Basement of the Brasília Belt, SE Tocantins- NE Goiás, Central Brazil: Constraints From U-Pb and Sm-Nd Isotopic Data. In: Alkmim, F.F., Noce, C.M., (eds.) 2006, The Paleoproterozoic Record of the São Francisco Craton. IGCP 509 Field workshop, Bahia and Minas Gerais, Brazil. Field Guide & Abstracts, 114 p.

Fuck, R.A., Dantas, E.L., Pimentel, M.M., Botelho, N.F., Armstrong, R., Laux, J.H., Junges, S.L., Soares, J.E., Praxedes, I.F., 2014, Paleoproterozoic crust-formation and reworking events in the Tocantins Province, central Brazil: A contribution for Atlantica supercontinent reconstruction. Precambr. Res., v. 244, p. 53-74.

Garcia, D., Coelho, J., Perrin, M., 1991, Fractionation between TiO_2 and Zr as a measure of sorting within shale and sandstone series (northern Portugal). European Journal of Mineralogy, v. 3, p. 401-414.

Gazis, C.A., Blum, J.D., Chamberlain, C.P., Poage, M., 1998, Isotope systematics of granites and gneisses of the Nanga Parbat Massif, Pakistan Himalaya. American Journal of Science, v. 298, p. 673-698.

Gioia, S.M.C.L., Pimentel, M.M., 2000, The Sm–Nd isotopic method in the Geochronology Laboratory of the University of Brasília. Anais da Academia Brasileira de Ciências, v. 72, p. 219-245.

Harley, S.L., Carrington, D.P., 2001, The distribution of H_2O between cordierite and granitic melt: H_2O incorporation in cordierite and its application to high-grade metamorphism and crustal anatexis. J. Petrol. v. 42, p. 1595-1620.

Heilbron, M., Duarte, B.P., de Morisson Valeriano, C., Simonetti, A., Machado, N., Nogueira, J.R., 2010, Evolution of reworked Paleoproterozoic basement rocks within the Ribeira belt (Neoproterozoic), SE-Brazil, based on U-Pb geochronology: implications for paleogeographic reconstructions of the São Francisco-Congo paleocontinent. Precambr. Res., v. 178, p. 136-148.

Herron, M.M., 1988, Geochemical classification of terrigenous sands and shales from core or log data. Journal of Sedimentary Petrology, v. 58, p. 820-829.

Holland, T., and Powell, R., 2003, Activity-composition relations for phases in petrological calculations; an asymmetric multicomponent formulation. Contributions to Mineralogy and Petrology, v. 145, p. 492-501.

Holland, T.J.B and Powell, R., 2011, An improved and extended internally consistent thermodynamic dataset for phases of petrological interest, involving a new equation of state for solids. Journal of Metamorphic Geology, v. 29, p. 333-383.

Huang, W.L., Wyllie, P.J., 1973, Melting relations of muscovite-granite to 35 kbar as a model for fusion of metamorphosed subducted oceanic sediments. Contributions to Mineralogy and Petrology, v. 42, p. 1-14.

Jackson, S.E., Pearson, N.J., Griffin, W.L., Belousova, E.A., 2004, The application of laser ablation-inductively coupled plasma-mass spectrometry to in situ U-Pb zircon geochronology. Chemical Geology, v. 211, p. 47-69.

Jiao, S.J., Guo, J.H., Harley, S.L., Windley, B.F., 2013, New constraints from garnetite on the P-T path of the Khondalite Belt: implications for the tectonic evolution of the North China Craton. J. Petrol., v. 54, p. 1725-1758.

Kosin, M., Guimarães, J.T., Abram, M.B. (Orgs.), 1999, Folha Aracaju-SW, folha SC.24-Y. Salvador, CPRM. Programa de Levantamentos Geológicos Básicos do Brasil – PLGB.

Kosin, M., Melo, R.C., Souza, J.D., Oliveira, E.P., Carvalho, M.J., Leite, C.M.M., 2003, Geologia do segmento norte do Orógeno Itabuna-Salvador-Curaçá e guia de excursão. Revista Brasileira de Geociências, v.33, p. 15-26.

Kriegsman, L.M., 2001, Partial melting, partial melt extraction and partial back reaction in anatectic migmatites. Lithos, v. 56, p. 75-96.

Lambert, I.B., Wyllie, P.J., 1972, Melting of gabbro (quartz eclogite) with excess water to 35 kilobars, with geological applications. Journal of Geology, v.80, p. 693-708.

Lana, C., Farina, F., Gerde, A., Alkmim, A., Gonçalves, G.O., Jardim, A.C., 2017, Characterization of zircon reference materials via high precision U–Pb LA-MC-ICP-MS. Journal of Analytical Atomic Spectrometry, v. 32, p. 2011-2023.

Litwinsky, N., 1985, Evolução Tectono-Termal da Região Nordeste de Minas Gerais e Sul da Bahia [Ph.D. thesis]: Instituto de Geociências, Universidade de São Paulo, 207 p.

Ludwig, K.R., 2003, Isoplot/Ex 3.00: A geochronological toolkit for Microsoft Excel. Berkeley Geochronology Center, Special Publication, n.4, 70 p.

Machado Filho, L., Ribeiro, M.W., Gonzalez, S.R., Schenini, C.A., Santos Neto, A.S., Barros Palmeira, R.C., Pires, J.L., Teixeira, W., Castro, H.E.F., 1983, Geologia. In: Projeto Radam Brasil, Folhas SF 23/24, Rio de Janeiro/Vitória, v. 32, p. 36-45.

Machado, N., Schrank, A., Noce, C.M., Gauthier, G., 1996, Ages of detrital zircon from Archean-Paleproterozoic sequences: implications for greenstone belt setting and evolution of a Transamazonian foreland basin in Quadrilátero Ferrífero, southeast Brazil: evidence from zircon ages by laser ablation ICP-MS. Earth Planetary Science Letters, v. 141, p. 259-276.

McLennan, S.M., Taylor, S.R., 1991, Sedimentary Rocks and Crustal Evolution: Tectonic Setting and Secular Trends. Journal of Geology, v. 99, p. 1-21.

McLennan, S.M., Hemming, S.R., Taylor, S.R., Eriksson, K.A., 1995, Early Proterozoic crustal evolution: Geochemical and Nd-Pb isotopic evidence from metasedimentary rocks, southwestern North America. Geochimica et Cosmochimica Acta, v. 59, p. 1153-1177.

Maniar, P.D., Piccoli, P.M., 1989, Tectonic discriminations of granitoids. Geological Socitey of America Bulletin, v. 101, p. 635-643.

Middlemost, E.A.K., 1994, Naming materials in magma/igneous rock system. Earth Sci Rev, v. 37, p. 215-224.

Miranda, D.A., Chaves, A.O., Campello, M.S., Ramos, S.L.L.M., 2019, Origin and thermometry of graphites from Itapecerica supracrustal succession of the southern Sao Francisco Craton by C isotopes, X-ray diffraction and Raman spectroscopy. International Geology Review, DOI: 10.1080/00206814.2018.1564073.

Moreira, H., Lana, C., Nalini Jr, H.A., 2016, The detrital zircon record of an Archaean convergent basin in the Southern São Francisco Craton, Brazil. Precambrian Res., v. 275, p. 84-99.

Nance, W.B., Taylor, S.R., 1976, Rare-Earth Element Patterns and Crustal Evolution, Australian Post-Archean Sedimentary-Rocks. Geochimica et Cosmochimica Acta, v. 40, p. 1539-1551.

Neri, M.E.N.V., Rosière, C.A., Lana, C.C., 2013, Supergrupo Minas na Serra de Bom Sucesso, extremo sudoeste do Quadrilátero Ferrífero – MG: petrografia, geoquímica e isótopos de U-Pb. Revista Geologia USP Série Científica, v. 13, n. 2, p. 117-202.

Nesbitt, H.W., Young, G.M., 1982, Early Proterozoic climates and plate motions inferred from major element chemistry of lutites. Nature, v. 299, p. 715-717.

Nesbitt, H.W., Young, G.M., 1984, Prediction of some weathering trends of plutonic and volcanic rocks based on thermodynamic and kynetic considerations. Geochimica et Cosmochimica Acta, v. 48, p. 1523-1534.

Noce, C.M., Machado, N., Teixeira, W., 1998, U-Pb Geochronology of gneisses and granitoids in the Quadrilatero Ferrıfero (Southern São Francisco Craton): age constraints for Archean and Paleoproterozoic magmatism and metamorphism. Revista Brasileira de Geociencias, v. 28, p. 95-102.

Noce, C.M., Pedrosa-Soares, A.C., Silva, L.C., Armstrong, R., Piuzana, D., 2007, Evolution of polycyclic basement in the Araçuaí Orogen based on U-Pb SHRIMP data: implications for the Brazil-Africa links in the Paleoproterozoic time. Precambrian Res., v. 159, p. 60-78.

Oliveira, A.H., 2004, Evolução tectônica de um fragmento do Cráton São Francisco Meridional com base em aspectos estruturais, geoquímicos (rocha total) e geocronológicos (Rb-Sr, Sm-Nd, Ar-Ar, U-Pb). Tese de Doutoramento. Universidade Federal de Ouro Preto, Brazil, 92p.

Patiño Douce, A.E., Johnston, A.D., 1991, Phase equilibria and melt productivity in the pelitic system: implications for the origin of peraluminous granitoids and aluminous granulites. Contrib. Miner. Petrol. v. 107, p. 202-218.

Pearce, J. A., 1996, Sources and setting of granitic rocks. Episodes, v. 19, n. 4, p. 120-125.

Pereira, R.M., Neumann, R., Salomão, M., Guimarães, P.V., Ramos, G.V., Dutra, A.C., Pedroso, E., 2016, Terrenos Khondalíticos: Prinicipais Domínios para Manganês, Grafita, Ouro e Zinco no Estado do Rio de Janeiro e Regiões Limítrofes. Geonomos, v. 24, n. 1, p. 45-51.

Pommier, A., Cocherie, A., Legendre, O., 2004, EPMA Dating User's manual: Age calculation from electron probe microanalyser measurements of U-Th-Pb. BRGM Documents, 9 p.

Powell, R., Holland, T.J.B., 2008, On thermobarometry. J. Metamorph. Geol., v. 26, p. 155-179.

Queiroz, T.D.A., 2016, Mapeamento Geológico, Petrografia, Aspectos Litogeoquímicos e Geofísicos da Região de Maracás (Folha Sd.24-V-D-I), Bahia, Brasil [Dissertation]: Instituto de Geociências, Universidade Federal da Bahia, 113 p.

Roser, B.P., Korsch, R.J., 1986, Discrimination of tectonic setting of sandstone-mudstone suites using SiO_2 content and K_2O/Na_2O ratio. Journal of Geology, v. 94, p. 635-650.

Roser, B.P., Korsch, R.J., 1988, Provenance Signatures of Sandstone-Mudstone suites determined using discriminant function analysis of major-element data. Chemical Geology, v. 67, p. 119-139.

Ruy, A.C., Silva, A.M., Toledo, C.L.B., Souza Filho, C.R., 2006, Uso de dados aerogeofísicos de alta densidade para mapeamento geológico em terrenos altamente intemperizados: o estudo de caso da região de Cláudio, porção sul do Cráton São Francisco. Revista Brasileira de Geofísica, v. 24, n. 4, p. 535-546.

Santos, T.J.S.S., Neto, J.A.N., Hackspacher, P.C., 2001, Petrografia e litogeoquímica das rochas do embasamento cristalino da região de Granja - CE. Revista de Geologia, v. 14, p. 33-48.

Santos, M.M., Lana, C., Scholz, R., Buick, I., Schmit, M.D., Kamo, S.L., Gerdes, A., Corfu, F., Tapster, S., Lancaster, P., Storey, C.D., Basei, M.A.S., Tohver, E., Alkmim, A., Nalini, H., Krambrock, K., Fantini, C., Wiedenbeck, M., 2017, A New Appraisal of Sri Lankan BB Zircon as a Reference Material for LA-ICP-MS U-Pb Geochronology and Lu-Hf Isotope Tracing. Geostandards and Geoanalytical Research, v. 41, n. 3, p. 335-358.

Sawyer, E.W., 2012, Melt segregation in the continental crust. Geology, v. 22, p. 1019-1022.

Scherrer, N.C., Eng, M., Gnos, E., Jakob, V., Liechti, A., 2000, Monazite analysis; from sample preparation to microprobe age dating and REE quantification. Schweizer Mineralogische und Petrographische Mitteilungen, v. 80, p. 93-105.

Silva, A.J.F., Azevedo, M.R., Valle Aguado, B., Nogueira Neto, J.A., Santos, T.J.S., Silva, F.D.O., 2014, Petrographical and geochemical signatures of the Granja paragneisses (Médio Coreaú Domain, NW Ceará, Brasil). Estudios Geológicos, v. 70, n. 2, p. 1-14.

Silva, A.J.F., 2017, Processos de Migmatização no Complexo Granulítico de Granja (Domínio Médio Coreaú, Ceará, Brasil). Universidade de Aveiro, Phd Thesis, 402p.

Slama, J., Kosler, J., Condon, D.J., Crowley, J.L., Gerdes, A., Hanchar, J.M., Horstwood, M.S.A., Morris, G.A., Nasdala, L., Norberg, N., Schaltegger, U., Schoene, B., Tubrett, M.N., Whitehouse, M.J., 2008, Plesovice zircon - A newnatural reference material for U-Pb and Hf isotopic microanalysis. Chemical Geology, v. 249, p. 1-35.

Stacey, J.S., Kramers, J.D., 1975, Approximation of terrestrial lead isotope evolution by a two-stage model. Earth and Planetary Science Letters, v. 26, p. 207-221.

Streckeisen, A.L., 1974, Classification and Nomenclature of Plutonic Rocks. Recommendations of the IUGS Subcommission on the Systematics of Igneous Rocks. Geologische Rundschau. Internationale Zeitschrift für Geologie. Stuttgart, v. 63, p. 773-786.

Sun, S.S., McDonough, W.F., 1989, Chemical and isotopic systematics of oceanic basalts, implications for mantle composition and processes. In: Saunders, A. D., Norry, M. J., (Ed.). Magmatism in the ocean basins. Geological Society of London, London, v. 42, p. 313-345.

Teixeira, W., Carneiro, M.A., Noce, C.M., Machado, N., Sato, K., Taylor, P.N., 1996, Pb, Sr and Nd isotope constraints on the Archean evolution of the gneissic-granitoid in the southern São Francisco Craton, Brazil. Precambr. Res., v. 78, p. 151-164.

Teixeira, W., Ávila, C.A., Dussin, I.A., Neto, A.C., Bongiolo, E.M., Santos, J.O., Barbosa, N.S., 2015, A juvenile accretion episode (2.35–2.32 Ga) in the Mineiro belt and its role to the Minas accretionary orogeny: zircon U-Pb-Hf and geochemical evidences. Precambr. Res., v. 256, p. 148-169.

Teixeira, W., Oliveira, E.P., Peng Peng, Dantas, E.L., Hollanda, M.H.B.M., 2017a, U-Pb geochronology of the 2.0 Ga Itapecerica graphite-rich supracrustal succession in the São Francisco Craton: Tectonic matches with the North China Craton and paleogeographic inferences. Precambrian Research, v. 293, p. 91-111.

Teixeira, W., Oliveira, E.P., Marques, L.S., 2017b, The nature and evolution of the Archean Crust of the São Francisco Craton, in Heilbron, M., Alkmim, F., Cordani, U.G., eds., São Francisco Craton, Eastern Brasil: tectonic genealogy of a miniature continent, Regional Geology Review Series. Springer-Verlag, p. 29-56.

Vielzeuf, D.,Montel, J.M., 1994, Partialmelting ofmetagreywackes part I. Fluid-absent experiments and phase relationships. Contrib. Miner. Petrol. v. 117, p. 375-393.

Walker, T.L., 1902, The geology of Kalahandi state, central provinces. Memoirs of the Geological Survey of India, v. 33, part 3, 22 p.

Wan, Y.S., Song, B., Liu, D.Y., Wilde, S.A.,Wu, J.S., Shi, Y.R., Yin, X.Y., Zhou, H.Y., 2006, SHRIMP U-Pb zircon geochronology of Palaeoproterozoic metasedimentary rocks in the North China Craton: evidence for a major Late Palaeoproterozoic tectonothermal event. Precambr. Res., v. 149, p. 249-271.

Werner, C.D., 1987, Saxonian granulites: a contribution to the geochemical diagnosis of original rocks in high-metamorphic complexes. Gerlands Beitraege zur Geophysik, v. 96, p. 271-290.

Winter, J.D., 2001, An Introduction to Igneous and Metamorphic Petrology: Prentice Hall, New Jersey, 695p.

White, R.W., Powell, R., Holland, T.J.B., Worley, B.A., 2000, The effect of TiO_2 and Fe_2O_3 on metapelitic assemblages at greenschist and amphibolite facies conditions: mineral equilibria calculations in the system K_2O-FeO-MgO-Al_2O_3-SiO_2-H_2O-TiO_2-Fe_2O_3. Journal of Metamorphic Geology, v. 18, p. 497-511.

White, R.W., Powell, R., Holland, T.J.B., 2001, Calculation of partial melting equilibria in the system Na_2O-CaO-K_2O-FeO-MgO-Al_2O_3-SiO_2-H_2O (NCKFMASH). Journal of Metamorphic Geology, v. 19, 139p.

White, R., Powell, R., Clarke, G.L., 2002, The interpretation of reaction textures in Fe-rich metapelitic granulites of the Musgrave Block, central Australia: constraints from mineral equilibrium calculations in the system K_2O-FeO-MgO-Al_2O_3-SiO_2-H_2O-TiO_2-Fe_2O_3. Journal of Metamorphic Geology, v. 20, p. 41-55.

White, R.W., Powell, R., Johnson, T.E., 2014a, The effect of Mn on mineral stability in metapelites revisited: new a-x relations for manganese-bearing minerals. Journal of Metamorphic Geology, v. 32, p. 809-828.

White, R.W., Powell, R., Holland, T.J.B., Johnson, T.E., Green, E.C.R., 2014b, New mineral activity-composition relations for thermodynamic calculations in metapelitic systems. Journal of Metamorphic Geology, v. 32, p. 261-286.

Whitney, D.L., Evans, B.W., 2010, Abbreviations for names of rock-forming minerals. American Mineralogist, v. 95, n. 1, p.185-187.

Williams, M.L., Jercinovic, M.J., Hetherington, C.J., 2007, Microprobe monazite geochronology: understanding geologic processes by integrating composition and chronology. Annu. Rev. Earth Planet. Sci., v. 35, p. 137-175.

Zacchi, E.N.P., Silva, A.M., Toledo, C.L.B., Souza Filho, C.R., 2007, As três anomalias elípticas da porção sul do Cráton São Francisco: novos alvos para a mineralização de grafita? Revista Brasileira de Geofísica, v. 25, n. 4, p. 421-431.

Zhou, J., Li, X., 2006, GeoPlot: an excel VBA program for geochemical data plotting. Computers e Geosciences, v. 32, p. 554-560.

Supplementary material

Supplementary Table 1 – Bulk rock compositions for the khondalite.

Sample	Major Elements										
	SiO_2	TiO_2	Al_2O_3	Fe_2O_3t	MnO	MgO	CaO	Na_2O	K_2O	Lol	Total
	detection limit 0.01 %										
06	63.97	0.67	17.36	6.95	0.12	2.39	1.63	3.42	2.91	1.25	100.67
13B	60.36	0.98	17.23	10.66	0.15	3.72	1.34	2.07	3.23	1.09	100.83
24	59.29	0.96	17.72	10.88	0.21	4.22	0.68	0.39	4.24	1.99	100.58
TILL-3 standard	71.94	0.52	12.21	3.76	0.07	1.66	2.57	2.86	2.35	-	-

	Incompatible Elements											
	Rb	Ba	Sr	Zr	Nb	Y	Ni	Co	Hf	Ta	Th	U
detection limit (ppm)	**0.2**	**10**	**10**	**10**	**0.05**	**0.05**	**5**	**0.5**	**0.05**	**0.05**	**0.1**	**0.05**
06	131.90	636.00	225.00	192.00	17.70	30.06	93.00	20.90	5.46	1.43	22.30	2.33
13B	137.60	861.00	164.00	200.00	10.16	148.69	165.00	35.20	4.94	0.58	15.80	1.77
24	196.00	2519.00	49.00	169.00	7.82	25.05	146.00	32.40	4.16	0.37	11.40	1.61
TILL-3 standard	53.20	459.00	310.00	240.00	6.54	-	47.00	14.30	-	0.42	4.20	1.94

	Rare Earth Elements																
	La	Ce	Pr	Nd	Sm	Eu	Gd	Tb	Dy	Ho	Er	Tm	Yb	Lu	Eu/Eu*	La_N/Yb_N	Gd_N/Yb_N
detection limit (ppm)	**0.1**	**0.1**	**0.05**	**0.1**	**0.1**	**0.05**	**0.05**	**0.05**	**0.05**	**0.05**	**0.05**	**0.05**	**0.1**	**0.05**	**-**	**-**	**-**
06	43.40	79.80	8.72	33.30	6.60	1.44	6.14	0.89	5.48	1.10	3.34	0.51	3.40	0.56	0.69	9.16	1.49
13B	344.20	84.30	60.63	202.50	33.90	8.93	35.53	5.80	32.34	6.14	16.56	2.10	13.70	1.90	0.79	18.02	2.15
24	36.10	71.20	8.15	31.20	5.90	0.62	5.12	0.78	4.78	0.97	2.86	0.41	2.80	0.38	0.34	9.25	1.51
TILL-3 standard	19.60	40.50	4.49	17.60	3.20	0.90	2.95	0.44	2.61	0.48	1.46	0.21	1.40	0.21	-	-	-

Supplementary Table 2 – Representative electron microprobe analyses of garnet.

Sample	**06**	**06**	**06**	**06**	**06**	**06**	**13B**	**13B**	**13B**	**13B**	**13B**	**13B**	**13B**	**13B**	**13B**	**13B**	**24**	**24**	**24**	**24**	**24**	**24**	**24**
Location	**C**	**R Bt**	**C**	**R Bt**	**R Crd**	**C**	**C**	**C**	**C**	**C**	**C**	**C**	**M**	**C**	**R Bt**	**R Qz**	**C**	**R Bt**	**R Crd**	**C**	**R Qz**	**C**	**R Qz**
SiO_2	37.23	36.06	37.25	37.21	36.80	37.21	37.84	36.65	37.52	36.92	37.65	37.62	37.62	37.36	37.32	37.55	37.19	37.21	37.90	37.35	37.38	36.93	37.91
TiO_2	0.00	0.00	0.09	0.00	0.00	0.00	0.00	0.01	0.00	0.00	0.06	0.00	0.00	0.04	0.03	0.00	0.00	0.03	0.01	0.00	0.09	0.03	0.00
Al_2O_3	21.37	20.94	20.78	21.30	21.46	21.65	22.05	22.62	21.66	21.99	21.51	21.57	21.51	21.02	21.63	21.69	22.38	22.04	21.66	22.43	21.49	21.31	21.56
Cr_2O_3	0.02	0.05	0.05	0.02	0.09	0.02	0.02	0.03	0.03	0.03	0.01	0.04	0.00	0.05	0.02	0.03	0.01	0.05	0.04	0.05	0.05	0.00	0.02
FeO_T	34.41	35.47	34.60	35.02	34.62	33.32	32.51	32.29	33.38	32.10	31.73	32.47	33.95	33.43	34.91	34.25	31.08	32.62	34.16	32.01	32.35	34.40	33.75
MnO	2.59	2.94	2.54	2.58	3.15	2.04	1.23	1.22	1.12	1.11	1.14	1.16	1.23	1.13	1.35	1.20	1.07	1.18	1.37	1.20	1.22	1.25	1.30
MgO	3.46	2.91	3.56	3.31	3.00	4.26	5.23	5.47	5.09	4.98	5.14	5.15	5.24	5.42	4.48	5.26	5.29	4.50	3.93	5.01	5.44	4.26	4.61
CaO	0.83	0.83	0.87	0.81	0.81	0.84	0.99	1.06	0.99	1.19	1.15	1.13	0.97	0.98	0.98	0.95	2.16	1.63	1.49	1.73	1.33	1.56	1.35
Na_2O	0.01	0.03	0.00	0.07	0.02	0.05	0.05	0.04	0.01	0.57	0.48	0.57	0.06	0.00	0.02	0.04	0.01	0.03	0.00	0.03	0.00	0.00	0.02
Total	99.93	99.23	99.73	100.32	99.93	99.39	99.91	99.38	99.79	98.89	98.87	99.70	100.57	99.43	100.74	100.96	99.19	99.30	100.55	99.82	99.35	99.74	100.52
Si	2.99	2.95	3.01	2.99	2.97	2.99	2.99	2.92	2.99	2.97	3.02	3.00	2.98	2.99	2.97	2.97	2.95	2.97	3.01	2.96	2.98	2.97	3.00
Ti	0.00	0.00	0.01	0.00	0.00	0.00	0.00	0.00	0.00	0.00	0.00	0.00	0.00	0.00	0.00	0.00	0.00	0.00	0.00	0.00	0.01	0.00	0.00
Al	2.02	2.02	1.98	2.02	2.04	2.05	2.06	2.12	2.03	2.08	2.03	2.03	2.01	1.98	2.03	2.02	2.10	2.08	2.02	2.09	2.02	2.02	2.01
Fe(ii)	2.31	2.43	2.33	2.35	2.34	2.24	2.15	2.15	2.22	2.16	2.13	2.17	2.25	2.24	2.32	2.26	2.06	2.18	2.27	2.12	2.16	2.31	2.23
Mn	0.18	0.20	0.17	0.18	0.22	0.14	0.08	0.08	0.08	0.08	0.08	0.08	0.08	0.08	0.09	0.08	0.07	0.08	0.09	0.08	0.08	0.08	0.09
Mg	0.42	0.36	0.43	0.40	0.36	0.51	0.62	0.65	0.60	0.60	0.61	0.61	0.62	0.65	0.53	0.62	0.63	0.54	0.46	0.59	0.65	0.51	0.54
Ca	0.07	0.07	0.08	0.07	0.07	0.07	0.08	0.09	0.08	0.10	0.10	0.10	0.08	0.08	0.08	0.08	0.18	0.14	0.13	0.15	0.11	0.13	0.11
Total	7.99	8.04	8.00	8.00	8.00	7.99	7.98	8.02	8.00	7.99	7.97	7.98	8.02	8.02	8.02	8.03	8.00	7.99	7.98	7.99	8.00	8.02	7.99
Prp	13.95	11.61	14.23	13.25	12.09	17.22	21.03	21.84	20.23	20.36	21.05	20.73	20.41	21.23	17.56	20.37	21.25	18.28	15.75	20.14	21.56	16.77	18.25
Alm	77.73	79.35	77.52	78.57	78.35	75.65	73.29	72.36	74.42	73.56	72.90	73.36	74.17	73.50	76.69	74.36	70.08	74.25	76.84	72.12	71.91	76.02	74.98
Gro	2.40	2.38	2.50	2.33	2.34	2.43	2.87	3.04	2.83	3.49	3.39	3.26	2.71	2.77	2.74	2.64	6.23	4.77	4.29	5.00	3.79	4.42	3.84
Sp	5.92	6.67	5.75	5.85	7.22	4.70	2.81	2.77	2.52	2.58	2.66	2.65	2.71	2.51	3.00	2.63	2.44	2.71	3.12	2.74	2.74	2.79	2.93
Z_{Ca}	0.03	0.03	0.03	0.02	0.03	0.03	0.03	0.03	0.03	0.04	0.03	0.03	0.03	0.03	0.03	0.03	0.06	0.05	0.04	0.05	0.04	0.05	0.04
X_{Mg}	0.15	0.13	0.16	0.14	0.13	0.19	0.22	0.23	0.21	0.22	0.22	0.22	0.22	0.22	0.19	0.22	0.23	0.20	0.17	0.22	0.23	0.18	0.20
X_{Fe}	0.85	0.87	0.84	0.86	0.87	0.81	0.78	0.77	0.79	0.78	0.78	0.78	0.78	0.78	0.81	0.78	0.77	0.80	0.83	0.78	0.77	0.82	0.80

*Notes: (1) cations to 12 oxygens. (2) FeOT is total FeO. (3) $Z_{Ca} = Ca/(Ca + Fe^{2+} + Mg + Mn)$. (4) $X_{Mg} = Mg/(Mg + Fe^{2+})$. (5) $X_{Fe} = Fe^{2+}/(Fe^{2+} + Mg)$. (6) C - Garnet core; M - Garnet mantle; R Bt - Garnet rimmed by biotite; R Qz - Garnet rimmed by quartz; R Crd - Garnet rimmed by cordierite.

Supplementary Table 3 – Representative electron microprobe analyses of biotite.

Sample	06	06	06	06	06	06	13B	13B	13B	13B	13B	13B	24	24	24	24	24	24
Location	M	M	Grt R	Grt R	In Grt	Crd R	Grt R	M	M	M	In Grt	Grt R	Grt R	M	Crd R	In Grt	M	Grt R
SiO_2	34.28	33.96	34.73	34.93	35.38	35.82	35.23	33.70	35.27	34.20	33.63	35.01	33.95	34.16	35.78	35.42	34.97	34.60
TiO_2	3.14	3.28	3.38	3.27	3.77	2.95	4.12	4.88	2.70	4.87	4.61	4.54	4.38	4.93	3.48	3.76	4.25	4.05
Al_2O_3	18.86	18.77	18.40	19.84	17.90	18.96	18.18	18.51	19.70	18.23	18.50	17.98	17.57	17.82	17.91	18.42	17.58	18.03
Cr_2O_3	0.17	0.19	0.16	0.12	0.15	0.16	0.16	0.18	0.19	0.15	0.05	0.20	0.21	0.25	0.22	0.10	0.18	0.18
FeO_T	19.76	19.96	19.52	18.31	17.57	19.15	18.43	18.09	21.16	18.19	16.75	17.52	18.54	18.38	16.87	14.18	17.87	17.77
MnO	0.04	0.02	0.02	0.01	0.06	0.05	0.11	0.07	0.03	0.03	0.03	0.05	0.06	0.05	0.00	0.06	0.03	0.01
MgO	8.74	8.69	8.91	8.02	10.03	8.40	10.37	9.99	10.19	10.11	12.17	10.39	9.91	9.17	10.24	12.78	9.68	9.62
CaO	0.03	0.01	0.03	0.06	0.06	0.02	0.01	0.03	0.12	0.02	0.02	0.00	0.02	0.01	0.03	0.06	0.04	0.03
Na_2O	0.24	0.26	0.11	0.13	0.31	0.25	0.14	0.17	0.10	0.23	0.33	0.18	0.17	0.28	0.23	0.27	0.34	0.27
K_2O	9.80	9.62	9.84	9.47	9.41	9.72	8.60	10.22	6.31	10.05	9.82	9.58	9.07	9.61	9.63	8.35	9.51	9.59
Total	95.05	94.75	95.10	94.14	94.62	95.46	95.36	95.82	95.77	96.08	95.90	95.44	93.87	94.65	94.40	93.40	94.43	94.15
Si	2.64	2.63	2.67	2.68	2.70	2.72	2.67	2.57	2.65	2.60	2.54	2.65	2.63	2.63	2.73	2.67	2.69	2.67
Ti	0.18	0.19	0.20	0.19	0.22	0.17	0.23	0.28	0.15	0.28	0.26	0.26	0.26	0.29	0.20	0.21	0.25	0.23
Al	1.71	1.71	1.67	1.79	1.61	1.70	1.62	1.66	1.74	1.63	1.65	1.61	1.61	1.62	1.61	1.64	1.59	1.64
Fe(ii)	1.27	1.29	1.25	1.17	1.12	1.22	1.17	1.15	1.33	1.15	1.06	1.11	1.20	1.18	1.08	0.90	1.15	1.14
Mn	0.00	0.00	0.00	0.00	0.00	0.00	0.01	0.00	0.00	0.00	0.00	0.00	0.00	0.00	0.00	0.00	0.00	0.00
Mg	1.00	1.00	1.02	0.92	1.14	0.95	1.17	1.14	1.14	1.14	1.37	1.17	1.15	1.05	1.16	1.44	1.11	1.11
Ca	0.00	0.00	0.00	0.00	0.01	0.00	0.00	0.00	0.01	0.00	0.00	0.00	0.00	0.00	0.00	0.01	0.00	0.00
Na	0.04	0.04	0.02	0.02	0.05	0.04	0.02	0.02	0.01	0.03	0.05	0.03	0.02	0.04	0.03	0.04	0.05	0.04
K	0.96	0.95	0.96	0.93	0.92	0.94	0.83	0.99	0.60	0.97	0.95	0.93	0.90	0.94	0.94	0.80	0.93	0.94
Total	7.82	7.82	7.79	7.71	7.76	7.75	7.71	7.83	7.64	7.81	7.87	7.76	7.77	7.77	7.75	7.71	7.77	7.77
X_{Mg}	0.44	0.44	0.45	0.44	0.50	0.44	0.50	0.50	0.46	0.50	0.56	0.51	0.49	0.47	0.52	0.62	0.49	0.49
X_{Fe}	0.56	0.56	0.55	0.56	0.50	0.56	0.50	0.50	0.54	0.50	0.44	0.49	0.51	0.53	0.48	0.38	0.51	0.51

*Notes: (1) cations to 11 oxygens. (2) FeO_T is total FeO. (3) $X_{Mg} = Mg/(Mg + Fe^{2+})$. (4) $X_{Fe} = Fe^{2+}/(Fe^{2+} + Mg)$. (5) Grt R - In the rim of garnet; M - In matrix; In Grt – Included in garnet; Crd R - In the rim of cordierite.

Supplementary Table 4 – Representative electron microprobe analyses of plagioclase.

Sample	**06**	**06**	**06**	**06**	**13B**	**13B**	**13B**	**24**	**24**	**24**	**24**
Location	**M**	**M**	**Grt R**	**M**	**Grt R**	**M**	**M**	**M**	**M**	**M**	**Grt R**
SiO_2	62.19	62.50	62.92	63.97	62.77	62.23	61.48	61.64	61.58	61.58	61.64
TiO_2	0.07	0.00	0.02	0.01	0.03	0.00	0.00	0.00	0.03	0.00	0.00
Al_2O_3	23.87	23.93	23.06	22.81	23.69	23.80	23.88	23.74	23.34	24.30	23.48
Cr_2O_3	0.00	0.00	0.00	0.02	0.00	0.00	0.00	0.05	0.04	0.00	0.00
FeO_T	0.01	0.00	0.00	0.15	0.00	0.02	0.00	0.04	0.13	0.01	0.05
MnO	0.04	0.00	0.01	0.02	0.02	0.00	0.01	0.00	0.00	0.00	0.00
MgO	0.00	0.00	0.01	0.13	0.00	0.00	0.00	0.00	0.01	0.00	0.00
CaO	4.58	4.70	4.58	2.99	5.47	5.74	5.65	7.19	6.79	7.42	7.67
Na_2O	8.42	7.69	8.00	7.66	7.85	7.78	8.08	6.67	7.11	6.84	6.85
K_2O	0.29	0.30	0.35	1.56	0.27	0.28	0.30	0.19	0.23	0.21	0.14
BaO	0.10	0.00	0.23	0.23	0.19	0.08	0.19	0.00	0.10	0.27	0.13
Total	99.57	99.13	99.18	99.56	100.30	99.91	99.59	99.53	99.37	100.63	99.97
Si	2.76	2.78	2.80	2.84	2.77	2.76	2.74	2.75	2.75	2.72	2.74
Ti	0.00	0.00	0.00	0.00	0.00	0.00	0.00	0.00	0.00	0.00	0.00
Al	1.25	1.25	1.21	1.19	1.23	1.24	1.26	1.25	1.23	1.27	1.23
Fe(ii)	0.00	0.00	0.00	0.01	0.00	0.00	0.00	0.00	0.01	0.00	0.00
Ca	0.22	0.22	0.22	0.14	0.26	0.27	0.27	0.34	0.33	0.35	0.37
Na	0.73	0.66	0.69	0.66	0.67	0.67	0.70	0.58	0.62	0.59	0.59
K	0.02	0.02	0.02	0.09	0.02	0.02	0.02	0.01	0.01	0.01	0.01
Total	4.98	4.94	4.95	4.93	4.95	4.96	4.99	4.92	4.94	4.94	4.94
An	22.72	24.77	23.52	15.98	27.34	28.50	27.40	36.90	34.07	37.02	37.92
Ab	75.55	73.34	74.35	74.09	71.04	69.87	70.90	61.93	64.53	61.72	61.28
Or	1.73	1.89	2.13	9.93	1.62	1.63	1.70	1.17	1.40	1.26	0.81
X_{Ca}	0.23	0.25	0.24	0.16	0.27	0.28	0.27	0.37	0.34	0.37	0.38

*Notes: (1) cations to 8 oxygens. (2) FeO_T is total FeO. (3) X_{Ca} = Ca/(Ca + Na + K). (4) Grt R - In the rim of garnet; M - In matrix.

Supplementary Table 5 – Representative electron microprobe analyses of cordierite.

Sample	**06**	**06**	**13B**	**13B**	**13B**	**13B**	**13B**	**13B**	**13B**	**13B**	**13B**	**24**	**24**	**24**	**24**	**24**	**24**
Location	**M**	**M**	**Grt R**	**Grt R**	**Grt R**	**Grt R**	**Grt R**	**M**	**M**	**Grt R**	**Grt R**	**M**	**M**	**M**	**M**	**M**	**M**
SiO_2	49.60	49.03	46.07	44.73	45.36	46.98	45.74	47.18	46.18	46.53	45.31	44.49	46.14	45.56	43.60	42.88	44.85
TiO_2	0.00	0.04	0.02	0.00	0.00	0.03	0.03	0.00	0.00	0.01	0.00	0.00	0.02	0.00	0.00	0.00	0.01
Al_2O_3	31.98	32.01	30.47	29.78	30.27	31.41	31.01	31.47	30.88	31.14	30.70	29.51	30.45	29.62	29.68	29.66	30.55
Cr_2O_3	0.00	0.02	0.00	0.01	0.01	0.01	0.00	0.02	0.01	0.00	0.03	0.00	0.00	0.02	0.00	0.00	0.00
FeO_T	3.65	3.74	3.41	4.07	4.20	3.06	3.97	3.53	4.18	3.39	4.02	4.32	3.56	4.29	3.90	4.05	3.31
MnO	0.92	1.06	0.00	0.09	0.02	0.01	0.01	0.03	0.04	0.01	0.00	0.10	0.08	0.07	0.01	0.10	0.06
MgO	10.85	10.62	3.58	3.74	4.37	3.46	4.05	3.71	4.29	3.96	4.41	4.91	4.50	4.83	4.46	4.31	4.20
CaO	0.00	0.03	0.08	0.08	0.14	0.12	0.13	0.10	0.07	0.09	0.12	0.06	0.05	0.08	0.06	0.09	0.06
Na_2O	0.11	0.13	0.33	0.41	0.89	0.76	0.73	0.43	0.46	0.51	0.66	0.13	0.09	0.15	0.17	0.16	0.21
K_2O	0.00	0.03	8.60	8.45	6.86	8.10	7.63	7.55	7.38	7.77	7.40	7.47	7.82	7.04	7.79	8.41	9.16
BaO	0.12	0.00	0.55	0.76	0.06	0.17	0.00	0.45	0.08	0.49	0.15	0.11	0.21	0.27	0.70	1.14	1.57
Total	97.24	96.70	93.10	92.12	92.18	94.10	93.28	94.47	93.55	93.89	92.80	91.09	92.91	91.92	90.37	90.79	93.99
Si	5.08	5.05	5.18	5.13	5.11	5.18	5.10	5.18	5.13	5.16	5.09	5.10	5.16	5.16	5.07	5.02	5.08
Ti	0.00	0.00	0.00	0.00	0.00	0.00	0.00	0.00	0.00	0.00	0.00	0.00	0.00	0.00	0.00	0.00	0.00
Al	3.86	3.89	4.04	4.02	4.02	4.08	4.08	4.07	4.04	4.07	4.06	3.98	4.01	3.95	4.07	4.09	4.08
Fe(ii)	0.31	0.32	0.32	0.39	0.40	0.28	0.37	0.32	0.39	0.31	0.38	0.41	0.33	0.41	0.38	0.40	0.31
Mn	0.08	0.09	0.00	0.01	0.00	0.00	0.00	0.00	0.00	0.00	0.00	0.01	0.01	0.01	0.00	0.01	0.01
Mg	1.66	1.63	0.60	0.64	0.73	0.57	0.67	0.61	0.71	0.65	0.74	0.84	0.75	0.82	0.77	0.75	0.71
Ca	0.00	0.00	0.01	0.01	0.02	0.01	0.02	0.01	0.01	0.01	0.01	0.01	0.01	0.01	0.01	0.01	0.01
Na	0.02	0.03	0.07	0.09	0.20	0.16	0.16	0.09	0.10	0.11	0.14	0.03	0.02	0.03	0.04	0.04	0.05
K	0.00	0.00	1.23	1.24	0.99	1.14	1.09	1.06	1.05	1.10	1.06	1.09	1.11	1.02	1.15	1.26	1.32
Total	11.00	11.02	11.45	11.53	11.47	11.43	11.48	11.35	11.42	11.41	11.48	11.47	11.40	11.39	11.49	11.58	11.57
X_{Mg}	0.84	0.84	0.65	0.62	0.65	0.67	0.64	0.65	0.65	0.68	0.66	0.67	0.69	0.67	0.67	0.65	0.69
X_{Fe}	0.16	0.16	0.35	0.38	0.35	0.33	0.36	0.35	0.35	0.32	0.34	0.33	0.31	0.33	0.33	0.35	0.31

*Notes: (1) cations to 18 oxygens. (2) FeOT is total FeO. (3) $X_{Mg} = Mg/(Mg + Fe^{2+})$. (4) $X_{Fe} = Fe^{2+}/(Fe^{2+} + Mg)$. (5) M - In matrix; Grt R - In the rim of garnet.

Supplementary Table 6 – Bulk rock compositions for the Água Rasa metagranite.

Sample	Major Elements												
	SiO_2	TiO_2	Al_2O_3	FeO_T	MnO	MgO	CaO	Na_2O	K_2O	Lol	Total		
	detection limit 0.01 %												
04	75.34	0.13	13.20	1.83	0.03	0.13	0.75	3.61	5.48	0.11	100.61		
05	74.97	0.15	13.33	2.01	0.03	0.17	0.76	3.00	5.30	0.28	100.00		
19	75.03	0.27	13.18	2.04	0.04	0.35	1.19	3.73	4.76	0.18	100.77		
TILL-3 standard	71.94	0.52	12.21	3.76	0.07	1.66	2.57	2.86	2.35	-	-		
	Incompatible Elements												
	Rb	**Ba**	**Sr**	**Zr**	**Nb**	**Y**	**Ni**	**Co**	**Hf**	**Ta**	**Th**	**U**	
detection limit (ppm)	**0.2**	**10**	**10**	**10**	**0.05**	**0.05**	**5**	**0.5**	**0.05**	**0.05**	**0.1**	**0.05**	
04	265.50	249.00	88.00	117.00	19.33	93.22	7.00	1.30	4.46	0.74	31.50	17.42	
05	237.70	334.00	71.00	161.00	19.70	69.18	7.00	4.50	5.14	0.90	42.40	22.22	
19	286.60	437.00	90.00	242.00	17.62	39.45	9.00	2.30	7.23	1.55	45.80	5.52	
TILL-3 standard	53.20	459.00	310.00	240.00	6.54	-	47.00	14.30	-	0.42	4.20	1.94	
	Rare Earth Elements												
	La	**Ce**	**Pr**	**Nd**	**Sm**	**Eu**	**Gd**	**Tb**	**Dy**	**Ho**	**Er**	**Tm**	**Yb**	**Lu**
detection limit (ppm)	**0.1**	**0.1**	**0.05**	**0.1**	**0.1**	**0.05**	**0.05**	**0.05**	**0.05**	**0.05**	**0.05**	**0.05**	**0.1**	**0.05**
04	39.70	76.70	8.60	31.20	7.90	0.42	9.39	1.98	14.40	3.09	10.10	1.57	10.30	1.47
05	48.60	96.30	10.64	37.30	8.40	0.37	9.53	1.62	10.30	2.18	6.20	0.84	5.00	0.69
19	57.60	116.40	12.35	43.50	8.10	0.48	7.37	1.14	7.02	1.41	4.08	0.60	4.10	0.56
TILL-3 standard	19.60	40.50	4.49	17.60	3.20	0.90	2.95	0.44	2.61	0.48	1.46	0.21	1.40	0.21

Supplementary Table 7 – U-Pb isotopic data of the Água Rasa metagranite (sample 04). [a] Signal 207Pb in cps (counts per second). [b] Contents of U and Th/U ratios in relation to GJ-1 zircon. [c] common Pb correction using Stacey and Kramers (1975) model. [d] Rho error relation coefficient of 206Pb/238U/207Pb/235U. [e] Discordance = 100-(206Pb/238U age / 207Pb/206Pb age x 100).

	f-206	^{207}Pb[a]	^{206}Pb[a]	U[b]	Th/U[b]	$^{206}Pb/^{204}Pb$[c]	$^{207}Pb/^{235}U$[c]	2σ	$^{206}Pb/^{238}U$[c]	2σ	Rho[d]	$^{207}Pb/^{206}Pb$[c]	2σ	$^{206}Pb/^{238}U$	± 2σ	$^{207}Pb/^{235}U$	± 2σ	$^{207}Pb/^{206}Pb$	± 2σ	Disc[e]
		(cps)	(cps)	(µg g^{-1})				(%)		(%)			(%)	(Ma)		(Ma)		(Ma)		(%)
PMG04-89	0.3057	1563444	153809	558.91	0.31	88.50	2.0187	2.40	0.1488	1.93	0.80	0.0984	1.42	894	16	1122	16	1594	27	20
PMG04-88	0.4672	1531061	153930	500.27	0.36	54.57	2.2572	2.53	0.1628	1.97	0.78	0.1005	1.58	972	18	1199	18	1634	29	19
PMG04-94	0.2732	2023046	195276	791.45	0.08	88.64	1.8099	2.41	0.1360	1.93	0.80	0.0965	1.44	822	15	1049	16	1558	27	22
PMG04-90	0.0149	1645860	152549	667.93	0.02	1113.49	1.6754	2.28	0.1311	1.88	0.83	0.0927	1.28	794	14	999	15	1481	24	21
PMG04-97	0.2010	1241829	133736	342.78	0.33	141.52	2.8620	2.36	0.1927	1.90	0.81	0.1077	1.40	1136	20	1372	18	1761	26	17
PMG04-68	0.1517	1369882	142265	404.85	0.32	186.46	2.5778	2.21	0.1800	1.85	0.84	0.1039	1.20	1067	18	1294	16	1694	22	18
PMG04-100	0.2215	1060762	106550	351.99	0.37	105.81	2.2206	2.40	0.1603	1.92	0.80	0.1004	1.44	959	17	1188	17	1632	27	19
PMG04-110	0.3898	1583073	168855	419.92	0.29	71.40	2.9498	2.56	0.2006	1.97	0.77	0.1067	1.64	1178	21	1395	20	1743	30	16

Supplementary Table 8 – Monazite U-Th-Pb_T ages, U, Th and Pb contents and respective errors. MPb is the average Pb atomic mass.

Água Rasa monazite - sample 04									
	Age	Error	U	Error	Th	Error	Pb	Error	M Pb
nº	Ma		ppm						
1	1960	50	4265	100	66701	667	7547	100	207.6
2	2082	49	3988	100	74267	743	8698	100	207.7
3	1937	49	4098	100	70761	708	7761	100	207.6
4	2087	45	4782	100	86606	866	10221	102	207.6
5	1911	44	4543	100	83934	839	8967	100	207.7
6	1962	48	3976	100	74795	748	8197	100	207.7
7	2079	62	2531	100	55189	552	6294	100	207.7
8	2063	45	5110	100	82185	822	9784	100	207.6
Khondalite monazite - sample 06 - in Garnet									
1	1955	60	6439	100	34062	341	5301	100	207.2
2	2122	56	6652	100	42007	420	6693	100	207.3
3	1940	74	4806	100	27454	275	4103	100	207.2
4	1935	54	7061	100	40188	402	5997	100	207.2
5	2081	57	6793	100	39247	392	6331	100	207.2
6	1952	52	8311	100	38992	390	6377	100	207.1
7	2106	54	7888	100	40425	404	6944	100	207.2
8	2105	52	8443	100	40425	404	7148	100	207.1
9	2119	56	7228	100	38878	389	6591	100	207.2
Khondalite monazite - sample 06 - in matrix									
1	2062	57	7329	100	36769	368	6220	100	207.2
2	2090	59	5867	100	42077	421	6294	100	207.3
3	1927	55	6271	100	43764	438	6025	100	207.3
4	1945	65	4801	100	36453	365	4929	100	207.4
5	2086	67	4839	100	36048	360	5310	100	207.3
6	2071	54	7481	100	40671	407	6684	100	207.2
7	1925	68	4142	100	36127	361	4623	100	207.4
8	1911	81	3905	100	26373	264	3639	100	207.3
9	2058	62	4872	100	41998	420	5811	100	207.4

Supplementary Table 9 – Whole-rock Sm-Nd and Rb-Sr data of the Água Rasa metagranite. $\varepsilon Nd_{(0)}$ and TDM model age values for whole rock are also shown.

Sm-Nd

Sample	Sm (ppm)	Nd (ppm)	$^{147}Sm/^{144}Nd$	Error (SE %)	$^{143}Nd/^{144}Nd_{(t=0)}$	Error (SE %)	$\varepsilon Nd_{(0)}$	$\varepsilon Nd_{(t)}$	T_{DM} (Ma)	$^{143}Nd/^{144}Nd_{(t)}$	*f*Sm/Nd	Age (Ma)
04-A	6.0	25.5	0.1425	0.0708	0.511917	0.0006	-14.1	-0.5	2407	0.510088	-0.28	1950
04-B	10.1	44.6	0.1373	0.0735	0.511739	0.0023	-17.5	-2.7	2604	0.509977	-0.30	1950

Rb-Sr

Sample	Rb (ppm)	Sr (ppm)	$^{87}Rb/^{86}Sr$	Error (SE %)	$^{87}Sr/^{86}Sr^{*}$	Error (SE %)	$^{87}Sr/^{86}Sr_{(t)}$	Age (Ma)
04-A	265.5	88.0	8.521776	0.8521	1.284377	0.0018	1.045111	1950
04-B	265.5	88.0	8.521776	0.8521	1.320991	0.0018	1.081725	1950

Supplementary Table 10 – Monazite chemical data.

Água Rasa monazite - sample 04															
nº	P_2O_5	SiO_2	ThO_2	UO_2	Y_2O_3	La_2O_3	Ce_2O_3	Pr_2O_3	Nd_2O_3	Sm_2O_3	Gd_2O_3	Dy_2O_3	CaO	PbO	Total
1	26.76	2.02	7.59	0.53	2.73	11.16	29.10	2.89	11.16	2.85	1.97	0.90	0.49	0.81	100.99
2	25.72	2.25	8.45	0.51	2.68	11.09	29.16	2.83	10.96	2.84	2.11	0.97	0.38	0.94	100.88
3	26.26	2.45	8.05	0.52	2.84	10.88	28.24	2.92	11.25	2.95	2.01	0.96	0.45	0.84	100.59
4	26.26	2.82	9.86	0.61	2.70	10.61	27.07	2.90	10.62	2.64	2.20	1.04	0.42	1.10	100.82
5	25.39	2.84	9.55	0.58	2.70	10.63	26.99	2.75	10.54	2.73	2.06	0.94	0.57	0.97	99.24
6	26.18	2.68	8.51	0.51	2.74	10.88	28.54	2.94	10.74	2.78	2.05	0.86	0.47	0.88	100.76
7	27.17	2.33	6.28	0.33	2.73	11.53	28.29	3.12	10.35	3.11	2.84	0.78	0.32	0.68	99.84
8	26.07	2.67	9.35	0.64	2.90	10.65	27.24	2.83	10.76	2.62	2.02	1.00	0.49	1.05	100.29
Khondalite monazite - sample 06 – in Garnet															
1	31.61	0.65	3.88	0.76	0.17	13.99	29.63	3.19	10.95	2.73	1.26	0.16	1.01	0.57	100.55
2	29.53	0.55	4.78	0.79	0.38	13.74	31.61	3.04	10.31	2.42	1.31	0.09	1.14	0.72	100.42
3	30.34	0.70	3.12	0.57	0.16	14.24	32.76	3.27	11.79	2.53	1.18	0.16	0.64	0.44	101.89
4	28.72	0.59	4.57	0.83	0.22	12.79	31.20	3.01	11.60	2.86	1.68	0.30	1.16	0.65	100.16
5	29.38	0.55	4.47	0.80	0.30	12.89	31.69	3.14	11.20	2.74	1.77	0.21	1.19	0.68	101.02
6	29.51	0.58	4.44	0.97	0.22	13.13	31.63	3.03	11.43	2.72	1.51	0.23	1.22	0.69	101.30
7	29.70	0.69	4.60	0.92	0.33	13.39	31.62	3.13	10.93	2.43	1.57	0.21	1.19	0.75	101.46
8	28.27	0.55	4.60	0.99	0.38	13.46	31.25	3.12	10.93	2.46	1.55	0.14	1.27	0.77	99.74
9	28.96	0.57	4.42	0.85	0.30	12.90	31.37	3.15	11.15	2.63	1.54	0.25	1.18	0.71	99.97
Khondalite monazite - sample 06 - in matrix															
1	26.28	3.67	4.18	0.86	0.33	12.94	31.56	3.19	10.63	2.48	1.40	0.17	1.17	0.67	99.53
2	26.83	4.19	4.79	0.70	0.33	13.23	30.04	3.13	10.88	2.65	1.21	0.13	1.22	0.68	100.00
3	26.61	3.79	4.98	0.74	0.20	13.10	30.93	3.09	10.76	2.35	1.32	0.08	1.12	0.65	99.73
4	25.77	3.59	4.15	0.57	0.19	13.23	31.69	3.27	11.37	2.28	1.46	0.26	0.89	0.53	99.25
5	26.70	2.26	4.10	0.58	0.31	13.27	32.10	3.11	11.36	2.35	1.36	0.21	0.97	0.57	99.24
6	27.43	2.99	4.63	0.88	0.25	12.52	31.06	3.01	10.56	2.70	1.52	0.03	1.12	0.72	99.40
7	25.09	2.05	4.11	0.50	0.12	13.24	32.82	3.22	12.12	2.20	1.15	0.09	0.93	0.50	98.11
8	26.68	2.14	3.00	0.46	0.15	13.35	32.84	3.30	11.92	2.53	1.19	0.18	0.73	0.39	98.85
9	26.36	2.20	4.78	0.58	0.28	12.92	31.31	3.06	11.43	2.37	1.21	0.06	1.25	0.63	98.42

ARTICLE III - Itapecerica metamafic-ultramafic rocks with E-MORB signature: ophiolitic remnants of the Rhyacian-Orosirian orogeny in southern São Francisco craton?

Daniel Andrade Miranda[a,*], Alexandre de Oliveira Chaves[a]

[a] *Institute of Geosciences – Federal University of Minas Gerais (UFMG). Av. Antonio Carlos, 6627, Belo Horizonte – MG, Brazil. CEP 31270-901.*

ABSTRACT

In the Southern São Francisco Craton near Itapecerica (Minas Gerais – Brazil) occurs a supracrustal succession of rocks, varying from bottom to top by quartzite, graphite schist, khondalitic paragneiss and banded iron formation whose protoliths are from oceanic basin with ages in the context of the Rhyacian-Orosirian orogeny. Amphibolite and metaultramafic bodies occur associated to this succession. Mineralogical and textural features of the amphibolite allow suggesting a gabbroic protolith metamorphosed to granulite facies and retrometamorphosed in amphibolite facies to generate the amphibolite. Geochemistry reveals tholeiitic affinity to the amphibolite protolith, which has an E-MORB signature, associating this rock to an oceanic setting. The association of amphibolite to metaperidotite in oceanic setting suggest the transition of lgabbros to ultramafic rocks in a typical ophiolite sequence. A possible suture zone in the Itapecerica/Claudio region formed by the collision between Divinopolis and Campo Belo/Bonfim complexes during the Rhyacian-Orosirian orogeny involving the Itapecerica oceanic basin alongside Claudio Shear Zone and forward to Minas Basin is a suggestive geological setting of the investigated region.

Keywords: Amphibolite; Metaperidotite; Ophiolite; Geochemistry; Petrography; São Francisco Craton.

Introduction

Ophiolites are fragments of oceanic lithosphere with fundamental constraints on the reconstruction of the evolution of an ancient oceanic basin and surrounding continental areas (Saccani 2015). They form in a wide variety of tectonic settings including oceanic spreading ridges, hot spots, and suprasubduction zone (SSZ) environments such as intra-oceanic arcs, continental arcs, forearcs and back-arcs (Dilek and Furnes 2011).

In the Southern São Francisco Craton near Itapacerica (Minas Gerais, Brazil) occurs a supracrustal succession of rocks, varying from bottom to top, constituted by quartzite (partly ferruginous with laminar graphite), graphite schist interlayered with quartzite bands and khondalitic paragneiss (Carneiro et al. 2007; Campello et al. 2015). Recent radiometric dating of these rocks linked them to the Rhyacian-Orosirian orogeny (monazite U-Th-Pb_T mean age

of 2010 ± 19 Ma (Chaves et al. 2015); a maximum deposition age of 2080 Ma and a metamorphic overprint on granulite facies of 2069 ± 84 Ma (Teixeira et al. 2017a); monazite U-Th-Pb_T age of 2090 ± 26 Ma corresponding to metamorphic peak and 1937 ± 32 Ma to orogen collapse (Miranda et al. 2020)). Amphibolite and metaultramafic bodies occur in this succession.

The tectonic model proposed by Miranda et al. (2019) includes the Itapecerica supracrustal succession in the Rhyacian-Orosirian orogeny alongside Paleoproterozoic Minas Supergroup involved in a progressive compressional deformation, which resulted in a fold-thrust belt developed by the collision of the São Francisco paleoplate nucleus with other terranes, and ultimately with the Congo paleoplate nucleus at ca. 2100 Ma or immediately after (Dutra et al. 2019).

The possibility that these metamafic-ultramafic rocks represent remnants of an ophiolite could constrain the tectonic setting of the Itapecerica region. This paper consists of a petrologic study of these rocks using petrography and whole-rock chemical composition to classify and identify the geochemical affinity and the tectonic environment of the amphibolites and metaultramafic rocks from Itapecerica supracrustal succession.

Geological Setting

The southern part of São Francisco Craton (SFC) (Fig 1A) consists of Archean crust (3.2–2.6 Ga) composed mainly of granite-gneisses (Farina et al. 2015; Teixeira et al. 2017b), greenstone belts (Rio das Velhas Supergroup), Paleoproterozoic clastic-chemical metasedimentary rocks (including the banded iron formations of the Quadrilatero Ferrifero (QF) mining district from Minas Supergroup), and Neoproterozoic pelitic-carbonate sedimentary rocks from Bambuí Group (Teixeira et al. 2017b).

The Archean granite-gneiss basement of the southern SFC is subdivided in distinct metamorphic complexes, named as Divinópolis, Campo Belo/Bonfim and Belo Horizonte (Machado Filho et al. 1983; Teixeira et al. 1996). (Fig 1B). The Minas Supergroup extends to the SW of the QF, as portrayed by the correlative strata along the Jeceaba-Bom Sucesso lineament (Neri et al. 2013). Mafic dykes of several generations crosscut the southern SFC (Chaves 2013).

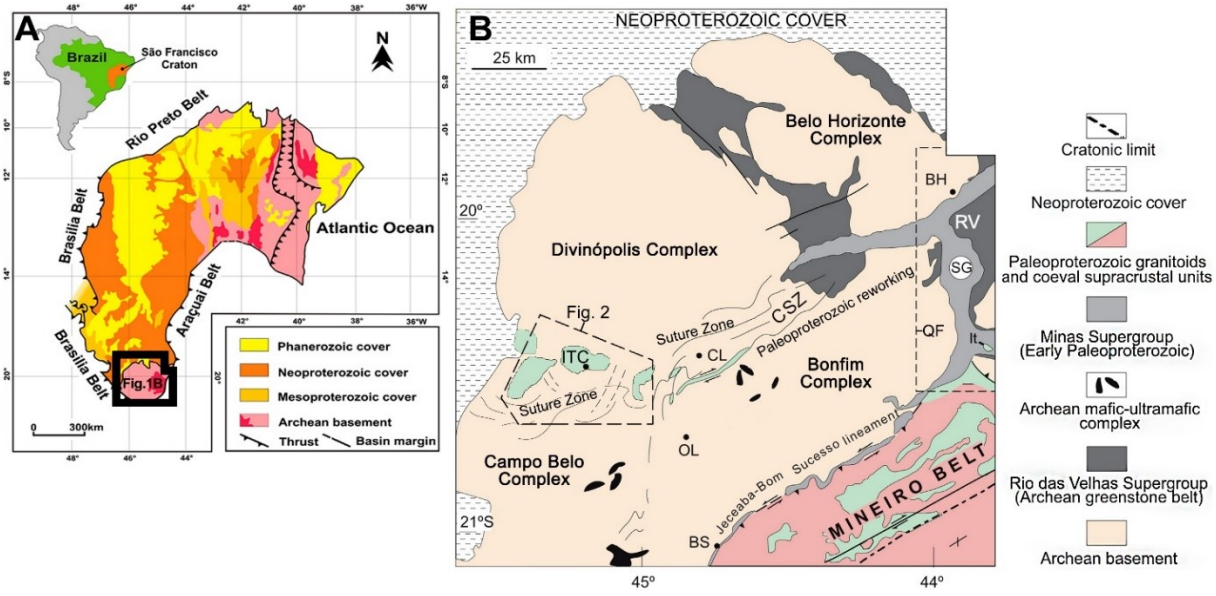

Figure 1. (A) Sao Francisco Craton location. Modified from Drummond et al. (2015). (B) Geological map of the southern portion of the Sao Francisco Craton. Keys: RV = Neoarchean Rio das Velhas Supergroup; SG = Sabará Group (Early Paleoproterozoic Minas Supergroup); It = Itacolomi Group (<1.96 Ga); CSZ = Cláudio Shear Zone; QF = Quadrilátero Ferrifero mining district. Towns: ITC (Itapecerica), CL (Cláudio), OL (Oliveira), BS (Bom Sucesso), BH (Belo Horizonte). Modified from Teixeira et al. (2017a).

The Rhyacian-Orosirian orogeny amalgamated arquean nucleus and different continental to oceanic arcs that collided to form the proto-SFC (Aguilar et al. 2017; Moreira et al. 2018). It is related to the deformation of the Minas Supergroup, to the accretion of juvenile crust that formed the Mineiro Belt to the southeast (Noce et al. 1998; Ávila et al. 2014; Teixeira et al. 2015) and was responsible for extensive reworking of terranes located at the margins of the craton (Noce et al. 2007). In the interior of the southern SFC Archean core, occur the Água Rasa metagranite (1934 ± 74 Ma from zircon U-Pb) and khondalites (monazite U-Th-Pb_T dating of 2090 ± 26 Ma and 1937 ± 32 Ma) from the Itapecerica supracrustal succession (Miranda et al. 2020). In addition, near the Cláudio Shear Zone (CSZ), amphibolites with E-MORB signature have igneous protolith crystallization U-Pb age of 2159 ± 21 Ma and metamorphic recrystallization age between 2.06 Ga and 2.03 Ga (Goulart 2006; Goulart and Carneiro 2010), confirming the existence of a Paleoproterozoic event in the region between the Archean Divinópolis and Campo Belo/Bonfim granite-gneiss metamorphic complexes (Fig. 1B).

The study area is located in the crystalline basement of the Itapecerica region (Fig. 1B). According to Carneiro and Barbosa (2008), the area contains gneisses, metagranitoids, amphibolites, mafic, metaultramafic and metacharnockitic rocks formed in the Mesoarchean

and recrystallized under high amphibolite- to granulite facies conditions (Fernandes and Carneiro 2000). The elliptical geophysical anomalies (Fig. 2A, 2B) hosting the second largest graphite mine in Brazil are located to the west of the CSZ around Itapecerica town. The Água Rasa Metagranite (Miranda et al. 2020) constitutes the perimeter of the elliptical anomalies. The country rocks that surround the Água Rasa Metagranite and the Itapecerica metasedimentary rocks (Fig. 2A) are distinguished as the Neoarchean Candeias (Campo Belo Complex) and Paleoproterozoic Itapecerica gneissic units (Divinopolis Complex). Both units show variable migmatization (Oliveira 2004; Campello et al. 2015).

The Divinópolis complex is composed predominantly of greyish TTG (tonalitic-trondhjemitic-granodioritic) orthogneisses with variable migmatization and Campo Belo/Bonfim complex has tonalitic-granodioritic composition with instrusions of 2790–2610 Ma granitoids and minor occurrence of metaultramafic-mafic rocks (Fernandes and Carneiro 2000; Oliveira 2004; Romano et al. 2013; Campello et al. 2015; Farina et al. 2015). The Archean Candeias Gneiss is part of the Campo Belo complex and is essentially greenish granulitic gneisses with granodioritic (charnoenderbites) to granitic (charnockites) composition and variable migmatization (Oliveira 2004; Carneiro et al. 2007).

The Paleoproterozoic Itapecerica migmatitic gneiss is here interpreted as formed by crustal reworking of the Divinópolis complex and Paleoproterozoic supracrustal sequences during Rhyacian-Orosirian Orogeny. According to Carneiro et al. (2007), it is a locally migmatized pinkish gneiss with peraluminous affinity and shows granitic to granodioritic composition. The 2.04 Ga Kinawa migmatite of the Itapecerica Metamorphic Complex (Carvalho et al. 2017) is an example of reworked crust, in which ~2.7 Ga metagranodiorites of the Campo Belo/Bonfim Metamorphic Complex were partially melted in the Cláudio Shear Zone (CSZ) during the Paleoproterozoic.

The Itapecerica graphite-rich metasedimentary rocks, amphibolite and meta-ultramafic bodies occur together inside the elliptical geophysical anomalies (Fig. 2B; Fig. 3A, 3B). The Itapecerica metasedimentary rocks essentially consist of khondalite paragneiss and minor lenticular graphite schist that is interlayered with quartzite bands (partly ferruginous with laminar graphite) and locally marble rocks (Fig. 3C). In particular, the khondalite exhibits compositional layering and local anatexis and may contain thin graphite films (Carneiro et al. 2007; Campello et al. 2015). The Itapecerica metasedimentary rocks went through of

amphibolite to granulite facies metamorphic conditions during continental collision with crustal thickning followed by tectonic exhumation and a post-peak decompressional stage due to orogen collapse (Miranda et al. 2020), and are strongly deformed (Teixeira et al. 2017a). In the surroundings are reported the occurrence of banded iron formation (Fig. 3D). Teixeira et al. (2017a) conducted isotopic studies on the Itapecerica graphite-rich supracrustal succession and the detrital zircon analyses in paragneiss indicated a maximum deposition age of 2080 Ma and a metamorphic overprint on granulite facies of 2069 ± 84 Ma (Fig. 2). Chaves et al. (2015) previously reported monazite electron microprobe chemical data in the paragneisses that yielded a U-Th-Pb_T mean age of 2010 ± 19 Ma.

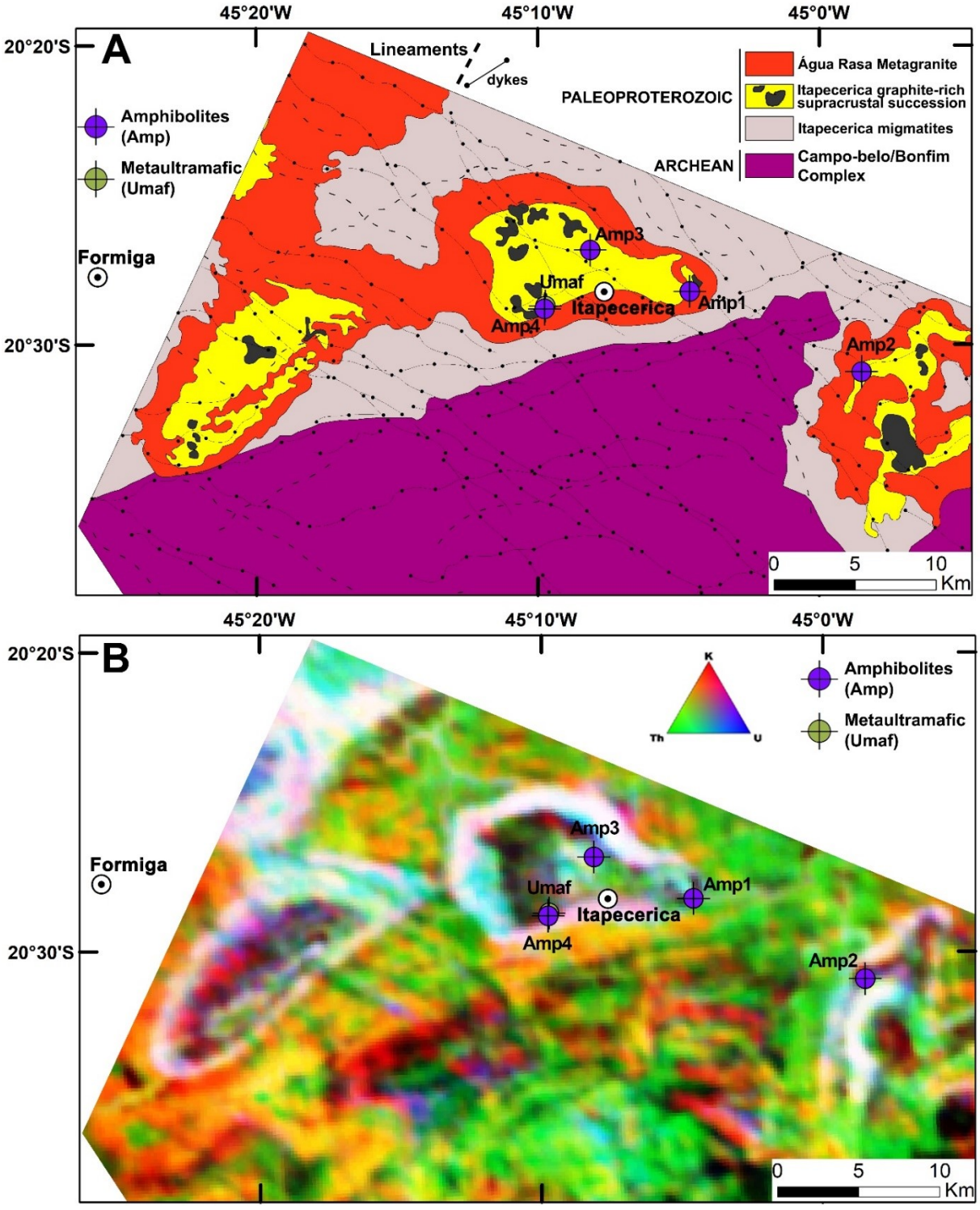

Figure 2. (A) Simplified geological map with samples sites. Amphibolite bodies are shown in black inside Itapecerica graphite-rich supracrustal succession. (B) Gammaespectrometry U-Th-K map. Addapted from Ruy et al. (2006) and Zacchi et al. (2007).

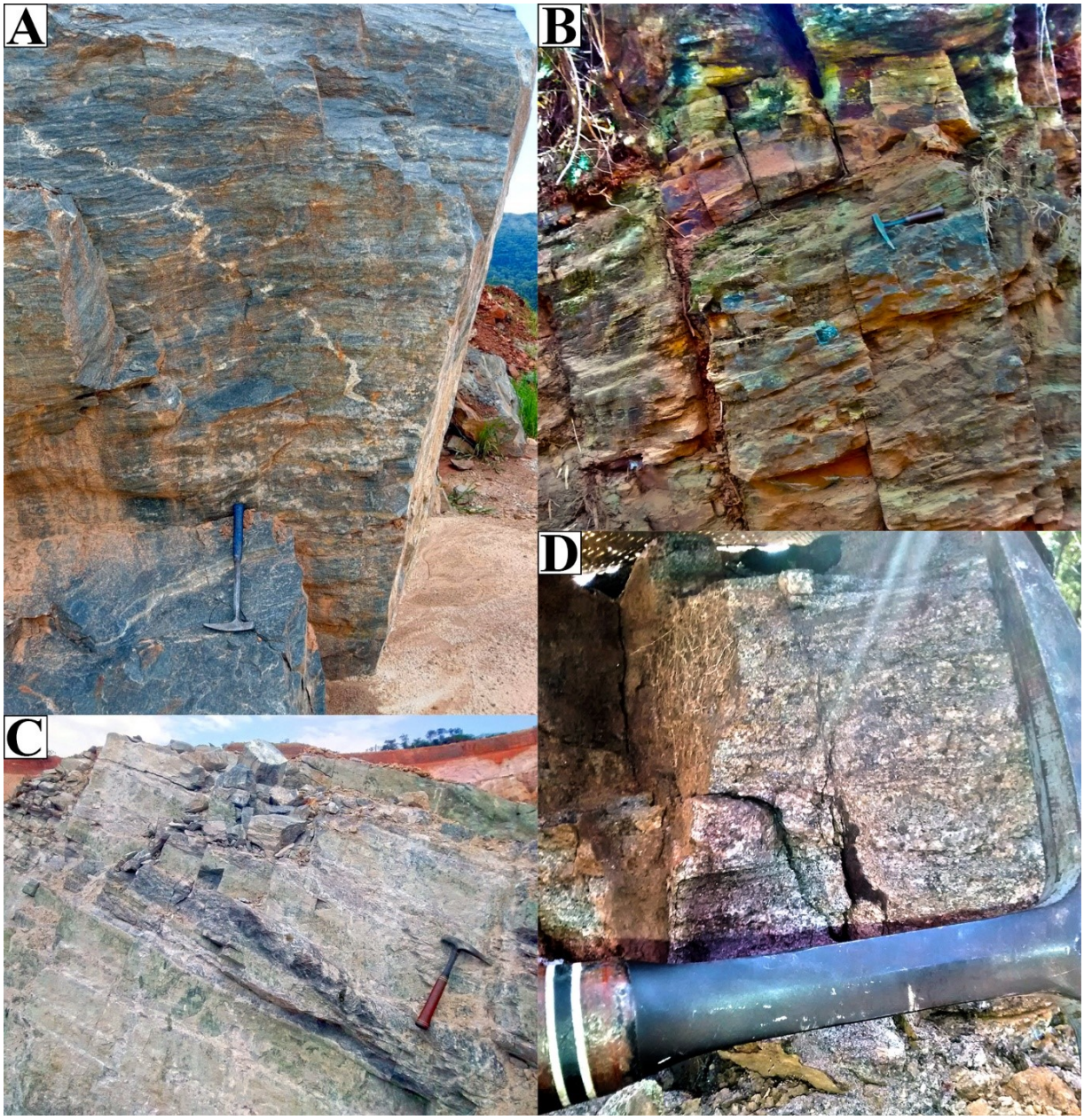

Figure 3. Sampling sites for amphibolite (A) and metaultramafic (B). (C) Occurrence of marble rocks inside a graphite mine. (D) Banded iron formation nearby Itapecerica.

Methods

Four petrographic thin sections from four samples of amphibolites and one of the metautramafic rock were made in the laboratories of the Geosciences Institute at Federal University of Minas Gerais (IGC/UFMG), and the same five samples were sent to the SGS-Geosol Laboratory, where, after tungsten milling, the material was melted with lithium metaborate and dilute nitric digestion. The major elements and five trace elements (Ba, Nb, Sr, Y, Zr) were analyzed by ICP-OES (Optical Emission Spectrometry with Inductively

Coupled Plasma). Other traces, together with fourteen REE, were analyzed by ICP-MS (Inductively Coupled Plasma Mass Spectrometry). Detection limits were generally around 0.01% for the major elements oxides and 1 ppm for trace and REE. The accuracy is in the range of 1-2% from the relative standard deviation. The loss on ignition (LOI) was determined by the mass difference after heating at 1000 °C. Then, to geochemical data treatment, the Geoplot program (Zhou and Li 2006) a supplement for Microsoft Excel, was used.

Mineral abbreviations are after Whitney and Evans (2010), including Cpx – clinopyroxene, Hbl – hornblende, Ol – olivine, Opx – orthopyroxene, Pl – plagioclase, Srp – serpentine, Spl – spinel, and Qz – quartz.

Results and Discussions

Metaultramafic

During field work, only one outcrop of layered metaultramafic rock was found (Fig. 3B), close to amphibolites and rocks of the Itapecerica supracrustal sequence (Fig. 2). In thin section, metaultramafic rock also shows layered structure and cumulate texture composed of serpentine (after olivine) cumulus and clinopyroxene and orthopyroxene intercumulus (Figs. 4A, 4B – white dashed lines). The mineral assemblage is composed of serpentine (after olivine) (~50%), clinopyroxene (~25%), orthopyroxene (~20%), and spinel and opaque minerals are the accessory minerals present in this rock. Olivine is serpentinized but some relict crystals are present (Fig. 4D). Clinopyroxene appears as fine to medium-sized granoblastic aggregates in subhedral shapes. Orthopyroxene appears as coarse to medium-sized grains in subhedral to anhedral shapes. The mineralogy allows to classify the rock protolith as a spinel lherzolite according to Streckeisen (1974). The growth of orthopyroxene to coarse grains would have occurred during the amphibolite to granulite facies metamorphism. During the post-peak decompressional stage due to orogen collapse most of the olivine was serpentinized.

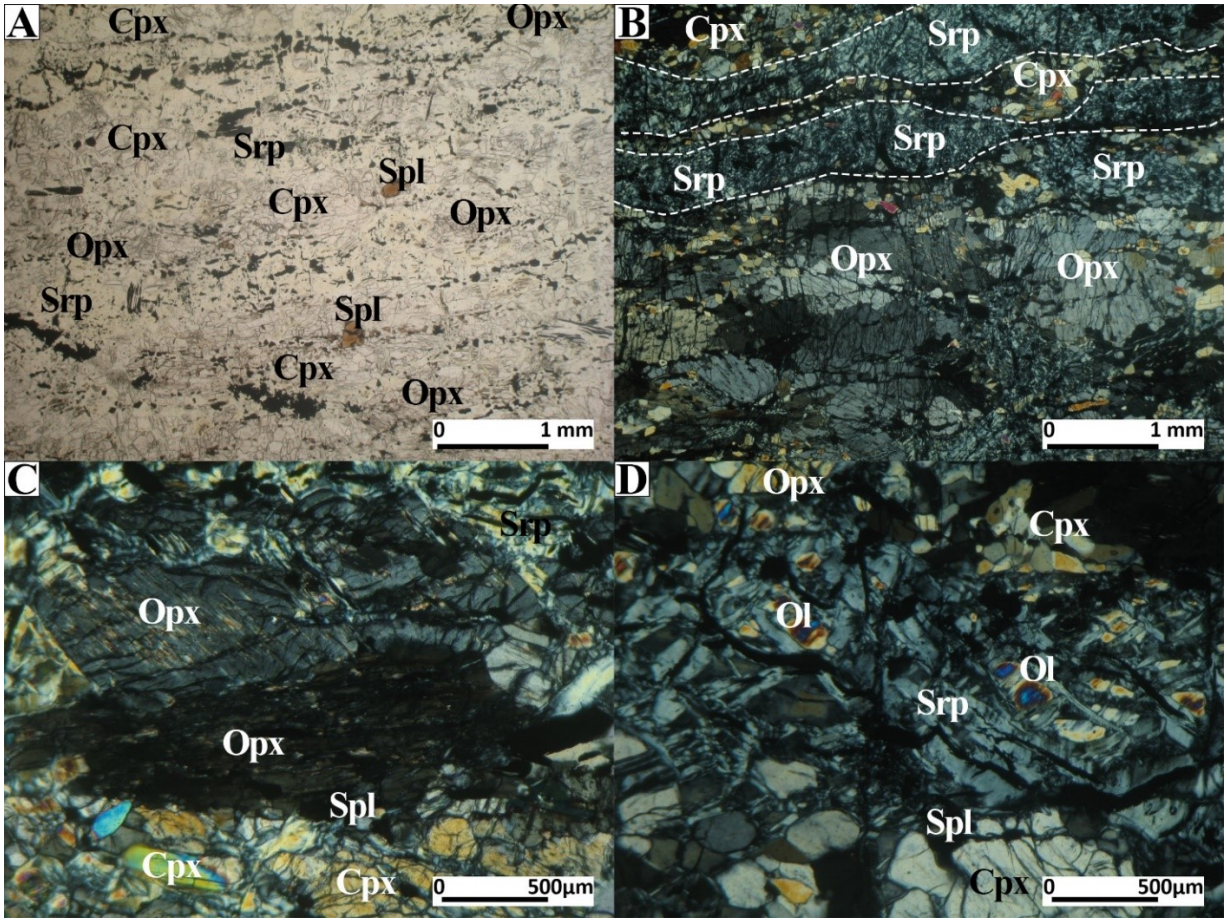

Figure 4. Photomicrographs (plane-polarized light, PPL; cross-polarized light, CPL) of representative mineral assemblages of the metaultramafic rock. (A) Photomicrograph (PPL) and (B) Photomicrograph (CPL) of the layered structure and cumulate texture. (C) Photomicrograph (CPL) of the two pyroxenes. (D) Photomicrograph (CPL) showing serpentine bands with relict olivine crystals.

Amphibolite

Amphibolite outcrops occur dispersed in the area in association to rocks of the Itapecerica supracrustal sequence (Fig. 2). The rock shows continuous centimeter-sized banding (Fig. 3A). The amphibolites are usually fine- to medium-grained rocks of granonematoblastic texture. The mineral assemblage is constituted by plagioclase (~40%), hornblende (~40%), clinopyroxene (~20%), and quartz, orthopyroxene and opaques minerals appear as accessories (Fig. 5). Plagioclase comprises the felsic portions of granoblastic aggregates. Hornblende defines the foliation, has medium-sized grains with polygonal boundaries and substitutes clinopyroxene (Fig. 5), which appears as relict crystal. Orthopyroxene and some quartz occur replacing clinopyroxene.

Mineralogical and textural features points out to a gabbroic protolith that was

metamorphosed in granulite facies conditions, followed by retrometamorphism recorded by the clinopyroxene being replaced by hornblende (Fig 5).

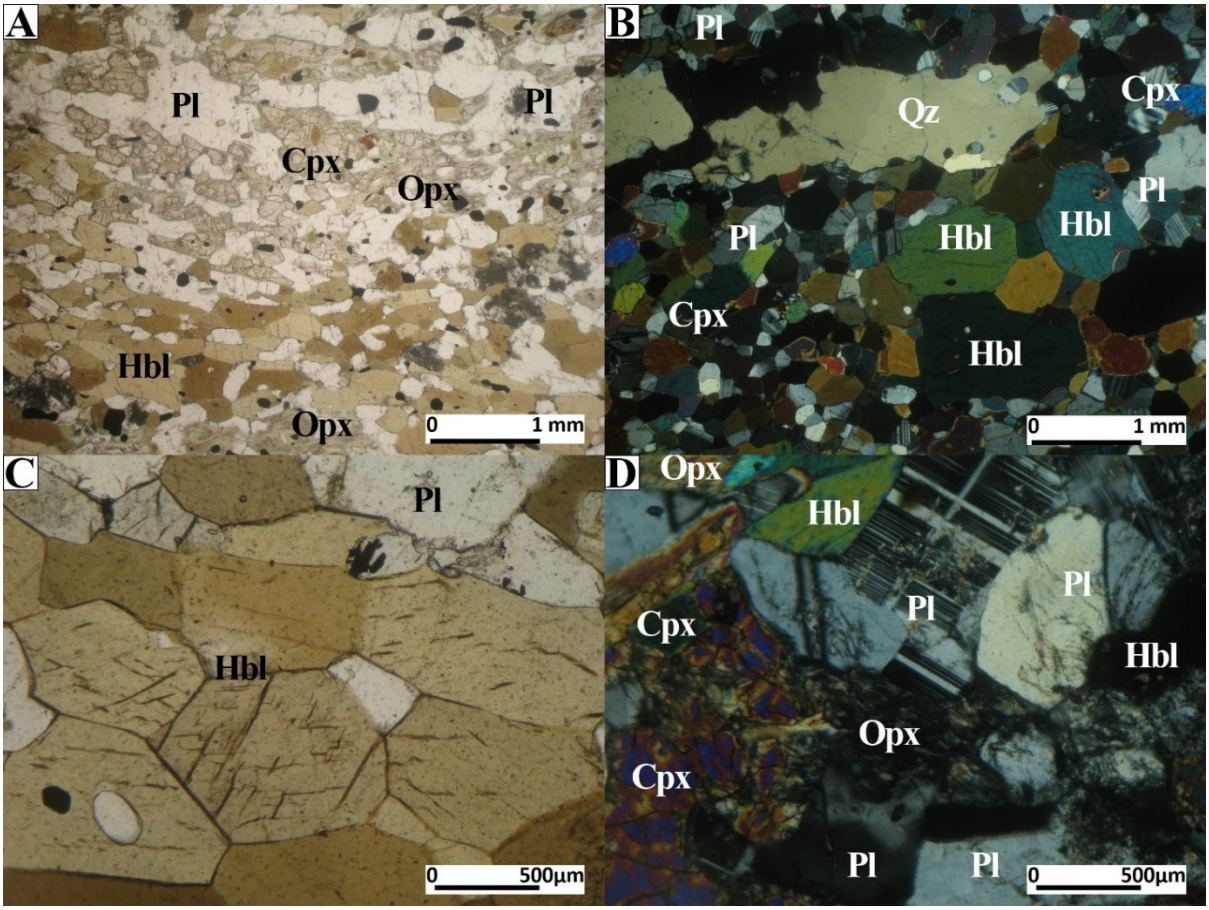

Figure 5. Photomicrographs (plane-polarized light, PPL- A, C, D; cross-polarized light, CPL - B) of representative mineral assemblage of the amphibolite.

Whole-rock geochemistry

The results of whole-rock geochemistry for the amphibolite and metaultramafic samples are listed on the Table 1. In terms of major components for the amphibolites, the SiO_2 concentration range from 50.06 to 51.94 (wt. %), $Na_2O + K_2O$ from 2.34 to 3.07 (wt. %) and Mg# ratios are berween 45.8-59.7, and the metautramafic has Mg# ratio of 88.4.

The amphibolite samples are classified as sub-alkaline tholeiitic basalt using the SiO_2 vs Nb/Y diagram (Xia and Li 2019) and AFM diagram (Irvine and Baragar 1971) (Fig. 6A, 6B). In Jensen diagram (Jensen 1976) (Fig. 6C) amphibolite samples are classified as high-Fe tholeiites and the metaultramafic has komatiitic composition. In V vs Ti/100 diagram (Shervais 1982), log(Sr/V) vs log((Na_2O*100)/Ga) diagram (Zhang et al. 2019) and

log(Nb/Y) vs log((K$_2$O*100)/Cu) diagram (Zhang et al. 2019) shown in Figure 7, amphibolites are classified as mid-ocean ridge basalts (MORB).

Amphibolites show similar to enriched-MORB (E-MORB) pattern in both chondrite-normalized REE and primitive mantle-normalized multi-element diagrams, but with negative anomalies in Nb and Ta (Fig. 8A, 8B). They have $(La/Yb)_N$ between 1.76-2.87 and a poorly fractionated light rare earth elements (LREE) distribution pattern [$(La/Sm)_N$ = 1.58-2.32] and flat heavy rare earth elements (HREE) distribution [$(Gd/Yb)_N$ = 1.16-1.32]. The patterns of the amphibolite are very similar to that of metaultramafic rock.

The amphibolites have Zr concentrations varying of 62 to 143 ppm (113 ppm in average) and 3.66 to 4.66 Zr/Y ratio (3.99 in average), have 1.64 to 5.92 ppm of Nb (3.6 ppm in average) and 0.28 to 0.46 Nb/La ratios (0.35 in average), indicating some crustal contamination of the gabroic protholith according to to Xia (2014) and Xia et al. (2008). In the Y/Nb vs Zr/Nb diagram (Xia and Li 2019), Th/Yb vs Nb/Yb diagram (Pearce 2008) and Th_N vs Nb_N diagram (Saccani 2015) respectively presented in Figs. 9A, 9B, and 9C, show a transitional (T-MORB) to enriched (E-MORB) signature for the amphibolites, and this enrichement could be related to crustal contamination.

Table 1 – Bulk rock compositions for the amphibolite and metaultramafic samples.

Sample	Major Elements (%)												
	SiO_2	TiO_2	Al_2O_3	FeO_T	MnO	MgO	CaO	Na_2O	K_2O	P_2O_5	Cr_2O_3	Lol	Total
	detection limit 0.01 %												
Amp1	51.63	1.89	14.20	12.13	0.30	4.39	11.86	2.84	0.23	0.19	0.03	0.16	99.85
Amp2	51.94	0.80	14.30	10.12	0.17	6.43	11.54	2.32	0.24	0.07	0.07	0.45	98.45
Amp3	51.18	1.09	13.98	10.14	0.20	6.20	11.16	2.21	0.27	0.12	0.04	0.45	97.04
Amp4	50.60	1.98	13.53	15.43	0.33	6.14	8.22	1.95	0.39	0.18	0.01	0.41	99.17
Umaf	45.78	0.20	4.50	9.19	0.14	30.00	3.02	0.08	0.04	0.01	0.36	7.07	100.39
TILL-3 standard	71.94	0.52	12.21	3.76	0.07	1.66	2.57	2.86	2.35	0.12	0.02	-	98.08

	Trace Elements (ppm)														
	Rb	Ba	Sr	Zr	Nb	Y	Ni	Co	Hf	Ta	Th	U	V	Cu	Ga
detection limit (ppm)	**0.20**	**10.00**	**10.00**	**10.00**	**0.05**	**0.05**	**5.00**	**0.50**	**0.05**	**0.05**	**0.10**	**0.05**	**5.00**	**5.00**	**0.10**
Amp1	3.30	72.00	228.00	143.00	5.92	38.84	106.00	42.40	3.65	0.29	0.80	0.24	325.00	55.00	14.00
Amp2	4.20	36.00	171.00	62.00	1.64	15.75	109.00	38.40	1.51	0.05	0.30	0.13	214.00	96.00	9.90
Amp3	6.40	58.00	129.00	117.00	3.20	25.09	77.00	38.50	2.47	0.09	0.60	0.26	243.00	115.00	11.20
Amp4	5.70	27.00	136.00	131.00	3.64	35.77	71.00	47.50	3.06	0.10	0.60	0.20	389.00	41.00	14.20
Umaf	1.60	10.00	48.00	25.00	0.53	5.03	1767.00	96.40	0.45	0.05	0.40	0.05	50.00	5.00	4.10
TILL-3 standard	53.20	459.00	310.00	240.00	6.54	-	47.00	14.30	-	0.42	4.20	1.94	70.00	27.00	13.70

	Rare Earth Elements (ppm)													
	La	Ce	Pr	Nd	Sm	Eu	Gd	Tb	Dy	Ho	Er	Tm	Yb	Lu
detection limit (ppm)	**0.10**	**0.10**	**0.05**	**0.10**	**0.10**	**0.05**	**0.05**	**0.05**	**0.05**	**0.05**	**0.05**	**0.05**	**0.10**	**0.05**
Amp1	12.90	19.20	3.23	16.50	5.00	1.76	6.84	1.13	7.35	1.61	4.59	0.66	4.30	0.65
Amp2	5.80	10.90	1.47	6.80	1.90	0.74	2.53	0.41	2.82	0.63	1.76	0.26	1.80	0.25
Amp3	10.80	16.90	2.31	10.90	3.00	1.03	4.00	0.68	4.53	0.96	2.88	0.41	2.70	0.40
Amp4	9.80	16.60	2.44	12.90	4.00	1.40	5.76	0.99	6.47	1.40	4.07	0.58	4.00	0.58
Umaf	3.10	3.10	0.60	2.40	0.50	0.23	0.87	0.14	0.89	0.17	0.52	0.07	0.50	0.07
TILL-3 standard	19.60	40.50	4.49	17.60	3.20	0.90	2.95	0.44	2.61	0.48	1.46	0.21	1.40	0.21

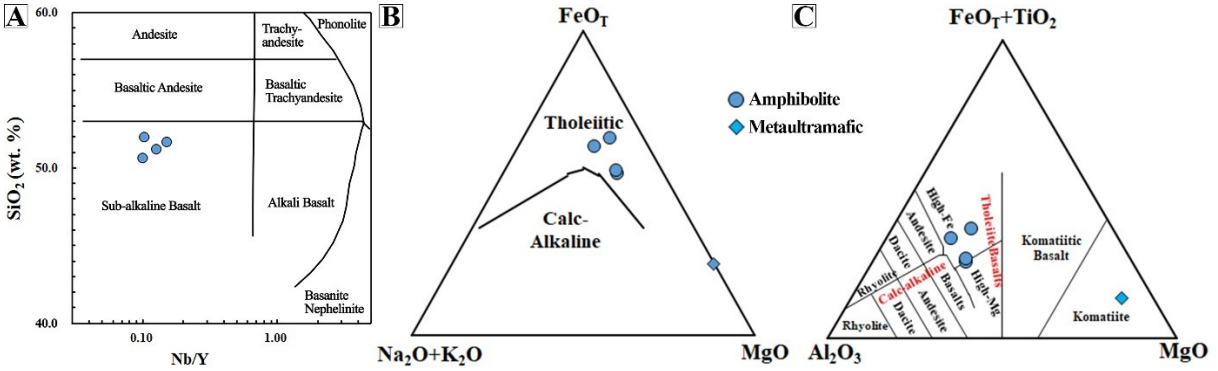

Figure 6. (A) SiO_2 vs Nb/Y diagram (Xia and Li 2019). (B) AFM diagram (Irvine and Baragar 1971). (C) Jensen diagram (1976).

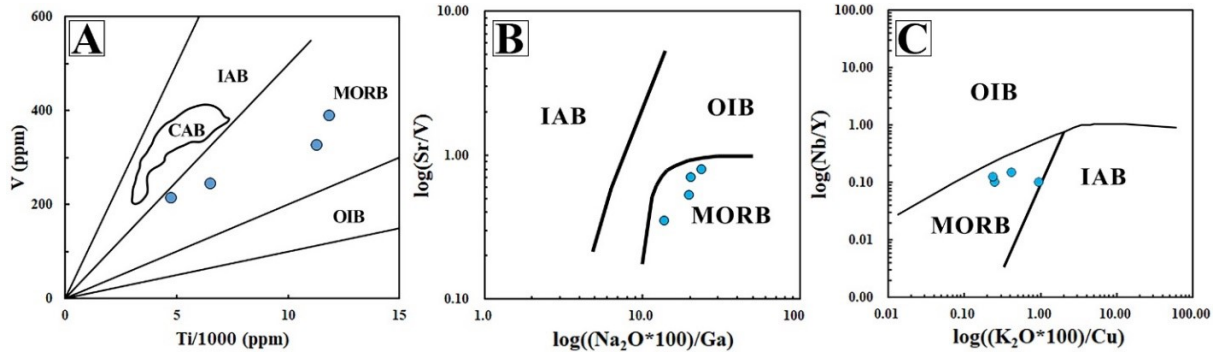

Figure 7. (A) V vs Ti diagram (Shervais 1982). (B) log(Sr/V) vs log((Na_2O*100)/Ga) diagram (Zhang et al. 2019). (C) log(Nb/Y) vs log((K_2O*100)/Cu) diagram (Zhang et al. 2019). CAB – Calc-alkaline basalts, IAB – Island arc basalts, OIB – Ocean island basalts, MORB – Mid-ocean ridge basalts. Only amphibolite samples were ploted.

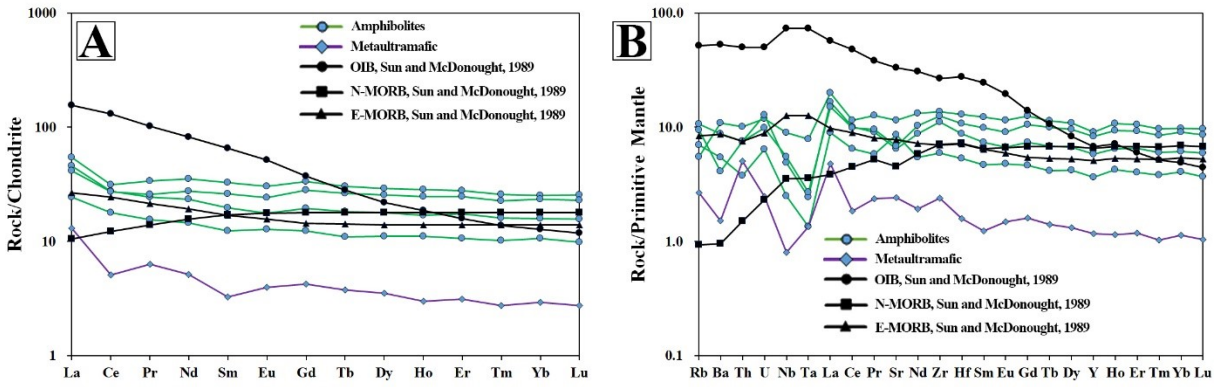

Figure 8. Chondrite-normalized REE (A) and primitive mantle-normalized multi-element (B) patterns for the amphibolite and metaultramafic rock. Chondrite and normal mid-ocean ridge basalt (N-MORB), E-MORB and ocean island basalt (OIB) normalizing values data are after Sun and McDonough (1989). Primitive mantle normalizing values are after McDonough and Sun (1995).

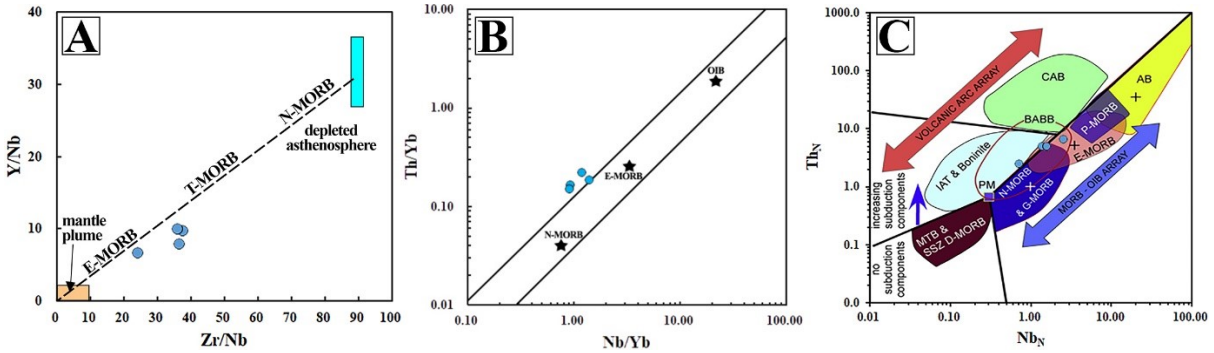

Figure 9. (A) Y/Nb vs Zr/Nb (Xia and Li 2019). (B) Th/Yb vs Nb/Yb (Pearce 2008). (C) Th_N vs Nb_N (Nb and Th are normalized to the N-MORB composition from Sun and McDonough 1989) (Saccani 2015). T – Transitional. N – Normal. E – Enriched. G - garnet-influenced, AB - alkaline basalt, IAT - island arc tholeiite, CAB - calc-alkaline basalt, BABB – back-arc basin basalt. Only amphibolite samples were ploted.

In the Itapecerica region, metaultramafic rock and amphibolites occur near each other, in the same context to the rocks of the Itapecerica supracrustal succession, and nearby banded iron formations, whose protoliths are from oceanic basins and went through metamorphism of granulite facies conditions. The anatexis of the amphibolites contributes to the generation of the Água Rasa Metagranite (Miranda et al. 2020) during the Rhyacian-Orosirian orogeny. Those conditions agree to the mineral paragenesis of the amphibolite, are suitable to crustal contamination from Itapecereica metasedimentary rocks, and the Nb and Ta anomalies can be related to fluid release from protolith during collision-related dehydration and incipient migmatization processes (Dey *et al*. 2018).

Geochemistry reveals high-Fe tholeiitic affinity for the amphibolite protolith with E-MORB signature. The association of amphibolites near metaperidotite in the region of Itapecerica, where rocks are from oceanic setting, suggests that the amphibolites and the metaultramafic could represent the transition of layered gabbros to ultramafic rocks in a typical ophiolite sequence, as shown in Figure 10. Chondrite-normalized REE and primitive mantle-normalized multi-element patterns for the amphibolite are very similar to that of metaultramafic rock (Fig. 8) suggesting a genetic correlation between them. Therefore, it is reasonable to suggest that Itapecerica sequence keeps fragments of an ophiolite (Fig. 10).

In the Tejuco Preto graphite mine (near Amp3 in Fig. 2; Miranda et al. 2019) is possible to observe a morphological pattern thart resembles pillow-like structures that could be from pillow lavas below the metasedimentary sequence (Fig. 11). They are exposed upside down due to the fold character of the rocks in the mine, where layers are overturned.

Unfortunately, due to the extremely weathered character, it was not possible to collect samples for petrography and geochemistry in order to investigate the ophiolitic proposition above.

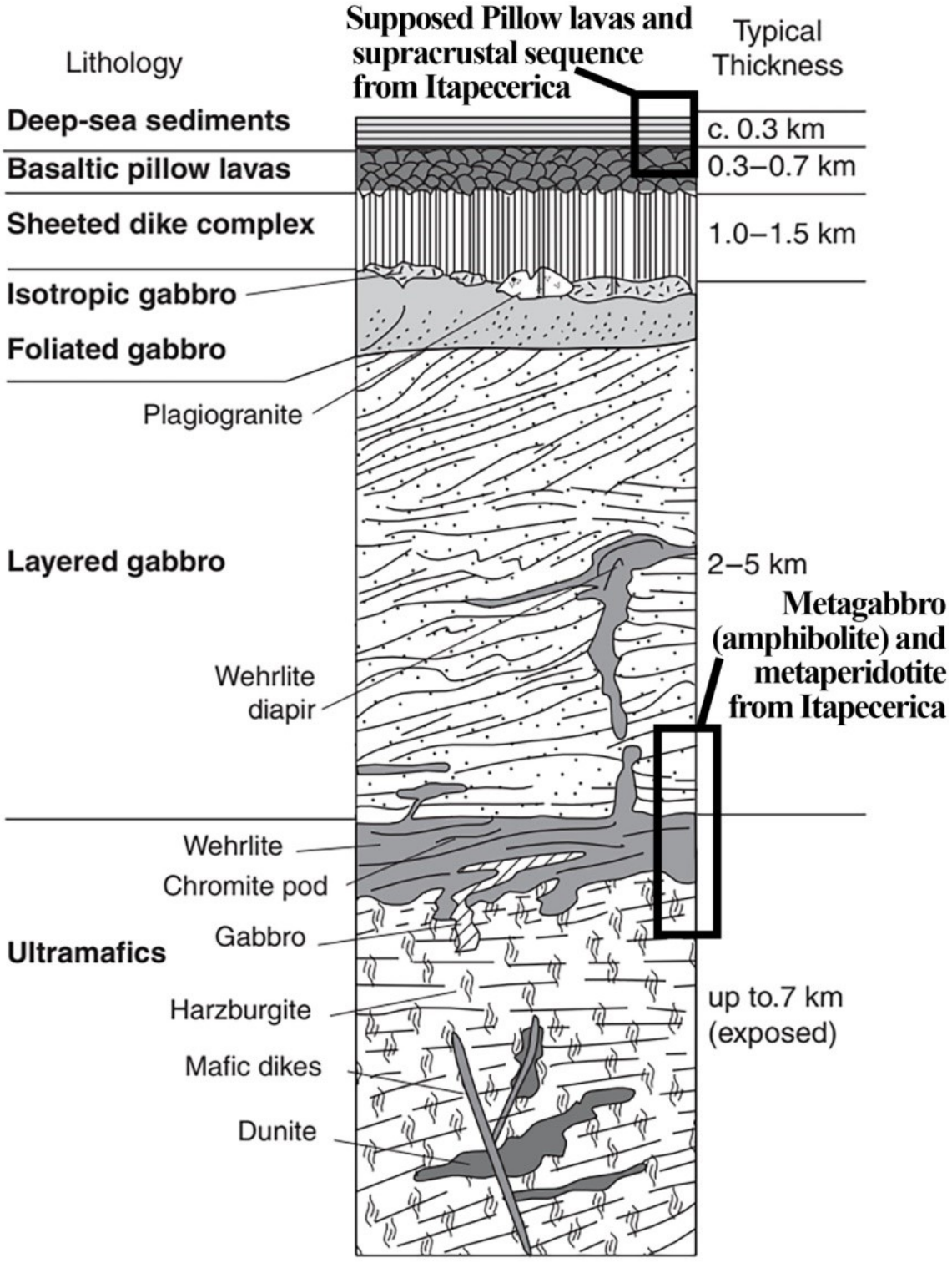

Figure 10. Lithology and thickness of a typical ophiolite sequence (Winter 2014).

Figure 11. Morphological pattern thart resembles pillow-shaped structures from supposed pillow lavas exposure in the Tejuco preto graphite mine from Itapecerica-MG.

Conclusion

The metaultramafic rock and amphibolites with E-MORB signature associated to the Itapecerica supracrustal succession rocks points to an oceanic setting. Adjacent 2.1 Ga amphibolites from the CSZ (Goulart 2006; Goulart and Carneiro 2010) found in the same orogenic context also have E-MORB signature. A possible suture zone in the Itapecerica/Claudio region formed by the collision between Divinopolis and Campo Belo/Bonfim complexes during the Rhyacian-Orosirian orogeny involving the Itapecerica oceanic basin alongside CSZ (Coelho and Chaves 2019) and forward to Minas Basin is a suggestive geological setting of the investigated region. Even if those pillow-like morphological shapes are or not pillow, the association of the metaultramafic and amphibolites can be related to the mantle-oceanic crust transition.

Acknowledgments: To the *Nacional de Grafite* Company, the geologist Lairton de Oliveira and geology supervisor Gilson dos Santos. This study was financed in part by the Coordenação de Aperfeiçoamento de Pessoal de Nível Superior - Brasil (CAPES) - Finance Code 001. The second author thanks to CNPq the research productivity grant and FAPEMIG for research support through the project APQ-00654-16.

References

Aguilar, C., Alkmim, F.F., Lana, C., Farina, F., 2017. Palaeoproterozoic assembly of the São Francisco craton, SE Brazil: new insights from U–Pb titanite and monazite dating. Precambrian Res., v. 289, p. 95-115.

Ávila, C.A., Teixeira, W., Bongiolo, E.M., Dussin, I.A., Vieira, T.A.T., 2014, Rhyacian evolution of subvolcanic and metasedimentary rocks of the southern segment of the Mineiro belt, São Francisco Craton, Brazil. Precambrian Res., v. 243, p. 221-251.

Campello, M.S., Vaz, B.B., Oliveira, M.A.S., Ávila, M.A.C., 2015. Relatório e mapa geológicos 1:100.000 da Folha Formiga SF.23-V-B-III. Projeto Fortaleza de Minas, CODEMIG/UFMG. A.C. Pedrosa Soares (coord.). 62 p.

Carneiro, M.A., Nalini Júnior, H.A., Endo, I., Suita, M.T.F., Castro, P.T.A., Barbosa, M.S.C., Campos, J.C.S., Goulart, L.E.A., Silva, E.F.S., Pereira, A.A., Tavares, T.D., Jiamelaro, F., Carneiro, J.M., Mariano, L.C., Miguel, F.P., Silva Junior, A.C., Barbosa, A.S., Prado, G.E.A., Santos, C., Urbano, E.E.M.C., 2007. Folha Campo Belo- SF.23-V-B-VI, escala 1:100.000: nota explicativa integrada com Oliveira. UFOP/CPRM, Minas Gerais, 114 p.

Carneiro, M.A., Barbosa, M.S.C., 2008. Implicações geológicas e tectônicas da interpretação magnetométrica da região de Oliveira, Minas Gerais. Revista Brasileira de Geofísica, v. 26, n. 1, p. 87-98.

Carvalho, B.B., Janasi, V.A., Sawyer, E.W., 2017. Evidence for Paleoproterozoic anatexis and crustal reworking of Archean crust in the São Francisco Craton, Brazil: a dating and isotopic study of the Kinawa migmatite. Precambrian Res., v. 291, p. 98-118.

Chaves, A.O., 2013. Enxames de diques máficos de Minas Gerais – o estado da arte. Geonomos, v. 21, n. 1, p. 29-33.

Chaves, A.O., Campello, M.S., Soares, A.C.P., 2015. Idade U-Th-PbT de monazitas do sillimanita-cordierita-granada-biotita gnaisse de Itapecerica (MG) e a atuação da orogenia Riaciano-Orosiriana no interior do Cráton São Francisco Meridional. Geociências, v. 34, n. 3, p. 324-334.

Coelho, R.M., Chaves, A.O. 2019. Pressure-temperature-time path of Paleoproterozoic khondalites from Claudio shear zone (southern São Francisco craton, Brazil): Links with khondalite belt of the North China craton. Journal of South American Earth Sciences, 102250.

Dey, A., Hussain, M.F., Barman, M.N., 2018. Geochemical characteristics of mafic and ultramafic rocks from the Naga Hills Ophiolite, India: Implications for petrogenesis. Geoscience Frontiers, v. 9, p. 517-529.

Dilek, Y., Furnes, H., 2011. Ophiolite genesis and global tectonics: geochemical and tectonic fingerprinting of ancient oceanic lithosphere. Geological Society of America Bulletin, v. 123, p. 387-411.

Dutra, L.F., Martins, M., Lana, C., 2019. Sedimentary and U-Pb detrital zircons provenance of the Paleoproterozoic Piracicaba and Sabará groups, Quadrilátero Ferrífero, Southern São Francisco craton, Brazil. Brazilian Journal of Geology, v. 49, n. 2, p. 1-21.

Drummond, J.B.R., Pufahl, P.K., Porto, C.G., Carvalho, M., 2015. Neoproterozoic peritidal phosphorite from the Sete Lagoas Formation (Brazil) and the Precambrian phosphorous cycle. Sedimentology, v. 62, p. 1978-2008.

Farina, F.A., Albert, C., Lana, C., 2015. The Neoarchean transition between medium and high-K granitoids: clues from the Southern São Francisco Craton (Brazil). Precambrian Res., v. 266, p. 375-394.

Fernandes, R.A., Carneiro, M.A.O., 2000. Complexo Metamórfico Campo Belo (Craton São Francisco Meridional): unidades litodêmicas e evolução tectônica. Revista Brasileira de Geociencias, v.30, n. 4, p. 671-678.

Goulart, L.E.A., 2006. O complexo acamadado Itaguara-Rio Manso, MG. Universidade Federal de Ouro Preto, dissertation, 186 p.

Goulart, L.E.A., Carneiro, M.A., 2010. Magmatismo máfico-ultramáfico Paleoproterozóico no cráton São Francisco meridional: a sequência acamadada Itaguara. In: 45º Congresso Brasileiro de Geologia, Sociedade Brasileira de Geologia, Belém, Anais, (abstract PAP212, in portuguese).

Irvine, T., Baragar, W., 1971. A guide to the chemical classification of the common volcanic rocks. Canadian Journal of Earth Sciences, v. 8, n. 5, p. 523-548.

Jensen, L.S., 1976. A new cation plot for classifying subalkaline volcanic rocks. Ontario Division Mines Miscellaneous Paper 66, 22p.

Machado Filho, L., Ribeiro, M.W., Gonzalez, S.R., Schenini, C.A., Santos Neto, A.S., Barros Palmeira, R.C., Pires, J.L., Teixeira, W., Castro, H.E.F., 1983. Geologia. In: Projeto Radam Brasil, Folhas SF 23/24, Rio de Janeiro/Vitória, v. 32, p. 36-45.

McDonough, W.F., Sun, S.S., 1995. The composition of the Earth. Chemical Geology, v. 67, n. 5, p. 1050-1056.

Miranda, D.A., Chaves, A.O., Campello, M.S., and Ramos, S.L.L.M., 2019. Origin and thermometry of graphites from Itapecerica supracrustal succession of the southern Sao Francisco Craton by C isotopes, X-ray diffraction and Raman spectroscopy. International Geology Review, v. 61, n. 15, p. 1864-1875.

Miranda, D.A., Chaves, A.O., Dussin, I.A., Porcher, C.C., 2020. Paleoproterozoic khondalites in Brazil: a case study of metamorphism and anatexis in khondalites from Itapecerica supracrustal succession of the southern São Francisco Craton. International Geology Review, doi:10.1080/00206814.2020.1716273.

Moreira, H., Seixas, L., Storey, C., Fowler, M., Lasalle, S., Stevenson, R., Lana, C., 2018. Evolution of siderian juvenile crust to rhyacian high Ba-Sr magmatism in the Mineiro belt, southern São Francisco craton. Geoscience Frontiers, v. 9, p. 977-995.

Neri, M.E.N.V., Rosière, C.A., Lana, C.C., 2013. Supergrupo Minas na Serra de Bom Sucesso, extremo sudoeste do Quadrilátero Ferrífero – MG: petrografia, geoquímica e isótopos de U-Pb. Revista Geologia USP Série Científica, v. 13, n. 2, p. 117-202.

Noce, C.M., Machado, N., Teixeira, W., 1998. U-Pb Geochronology of gneisses and granitoids in the Quadrilatero Ferrıfero (Southern São Francisco Craton): age constraints for Archean and Paleoproterozoic magmatism and metamorphism. Revista Brasileira de Geociencias, v. 28, p. 95-102.

Noce, C.M., Pedrosa-Soares, A.C., Silva, L.C., Armstrong, R., Piuzana, D., 2007. Evolution of polycyclic basement in the Araçuaí Orogen based on U-Pb SHRIMP data: implications for the Brazil-Africa links in the Paleoproterozoic time. Precambrian Res., v. 159, p. 60-78.

Oliveira, A.H., 2004. Evolução tectônica de um fragmento do Cráton São Francisco Meridional com base em aspectos estruturais, geoquímicos (rocha total) e geocronológicos (Rb-Sr, Sm-Nd, Ar-Ar, U-Pb). Tese de Doutoramento. Universidade Federal de Ouro Preto, Brazil, 92p.

Pearce, J.A. 2008. Geochemical fingerprinting of oceanic basalts with applications to ophiolite classification and the search for Archean oceanic crust. Lithos, v.100, p.14–48.

Ruy, A.C., Silva, A.M., Toledo, C.L.B., Souza Filho, C.R., 2006. Uso de dados aerogeofísicos de alta densidade para mapeamento geológico em terrenos altamente intemperizados: o estudo de caso da região de Cláudio, porção sul do Cráton São Francisco. Revista Brasileira de Geofísica, v. 24, n. 4, p. 535-546.

Saccani, E., 2015. A new method of discriminating different types of post-Archean ophiolitic basalts and their tectonic significance using Th-Nb and Ce-Dy-Yb systematics. Geoscience Frontiers, v. 6, p. 481-501.

Shervais, J.W. 1982. Ti-V plots and the petrogenesis of modern ophiolitic lavas. Earth and Planetary Science Letters, v. 59, n. 1, p. 101–118

Streckeisen, A.L., 1974, Classification and Nomenclature of Plutonic Rocks. Recommendations of the IUGS Subcommission on the Systematics of Igneous Rocks. Geologische Rundschau. Internationale Zeitschrift für Geologie. Stuttgart, v. 63, p. 773-786.

Sun, S.S., McDonough, W.F., 1989. Chemical and isotopic systematics of oceanic basalts, implications for mantle composition and processes. In: Saunders, A. D., Norry, M. J., (Ed.). Magmatism in the ocean basins. Geological Society of London, London, v. 42, p. 313-345.

Teixeira, W., Carneiro, M.A., Noce, C.M., Machado, N., Sato, K., Taylor, P.N., 1996. Pb, Sr and Nd isotope constraints on the Archean evolution of the gneissic-granitoid in the southern São Francisco Craton, Brazil. Precambr. Res., v. 78, p. 151-164.

Teixeira, W., Ávila, C.A., Dussin, I.A., Neto, A.C., Bongiolo, E.M., Santos, J.O., Barbosa, N.S., 2015. A juvenile accretion episode (2.35–2.32 Ga) in the Mineiro belt and its role to the Minas accretionary orogeny: zircon U-Pb-Hf and geochemical evidences. Precambr. Res., v. 256, p. 148-169.

Teixeira, W., Oliveira, E.P., Peng, P., Dantas, E.L., Hollanda, M.H.B.M., 2017a. U-Pb geochronology of the 2.0 Ga Itapecerica graphite-rich supracrustal succession in the São Francisco Craton: Tectonic matches with the North China Craton and paleogeographic inferences. Precambrian Research, v. 293, p. 91-111.

Teixeira, W., Oliveira, E.P., Marques, L.S., 2017b. The nature and evolution of the Archean Crust of the São Francisco Craton, in Heilbron, M., Alkmim, F., Cordani, U.G., eds., São Francisco Craton, Eastern Brasil: tectonic genealogy of a miniature continent, Regional Geology Review Series. Springer-Verlag, p. 29-56.

Winter, J.D., 2014. Principles of Igneous and Metamorphic Petrology. Pearson Education, 2 ed., 744 p.

Whitney, D.L., Evans, B.W., 2010. Abbreviations for names of rock-forming minerals. American Mineralogist, v. 95, n. 1, p.185-187.

Xia, L.Q., Xia, Z.C., Xu, X.Y., Li, X.M., Ma, Z.P., 2008. Relative contributions of crust and mantle to the generation of the Tianshan Carboniferous rifrelated basic lavas, northwestern China. Journal of Asian Earth Sciences, v. 31, n. 4-6, p.357-378.

Xia, L.Q., 2014. The geochemical criteria to distinguish continental basalts from arc related ones. Earth-Science Reviews, v. 139, p. 195-212.

Xia, L., Li, X., 2019. Basalt geochemistry as a diagnostic indicator of tectonic setting. Gondwana Research, v. 65, p. 43-67.

Zacchi, E.N.P., Silva, A.M., Toledo, C.L.B., Souza Filho, C.R., 2007. As três anomalias elípticas da porção sul do Cráton São Francisco: novos alvos para a mineralização de grafita? Revista Brasileira de Geofísica, v. 25, n. 4, p. 421-431.

Zhang, Q., Sun, W., Zhao Y., Yuan, F., Jiao, S., Chen, W., 2019. New discrimination diagrams for basalts based on big data research. Big Earth Data, v. 3, n.1, p. 45-55.

Zhou, J., Li, X., 2006. GeoPlot: an excel VBA program for geochemical data plotting. Computers e Geosciences, v. 32, p. 554-560.

FINAL COMMENTS

The Itapecerica supracrustal succession in the southern São Francisco Craton, around Itapecerica (MG), appear as elliptical geophysical anomalies containing, in their internal portions, sillimanite-cordierite-garnet-biotite gneiss (khondalite) with anatectic record, quartzite, graphite schist and banded iron formation, whose protoliths from oceanic basin

have ages in the context of the Rhyacian-Orosirian orogeny. With mixed pelite to wacke compositions and organic matter accumulation, part of the original sediments comes from the erosion of different sources of an active continental margin setting. Metaultramafic rocks and amphibolites wtih tholeiitic affinity and E-MORB signature occur associated to this succession, suggesting to be meta-ophiolitic fragments.

The organic matter became graphite around 729 ºC and the sediments became sillimanite-cordierite-garnet-biotite gneiss (khondalite) during metamorphic peak of 715–772 ºC and 5.5–7.5 kbar at 2090 ± 26 Ma (monazite U-Th-Pb_T). These conditions represent the transition of amphibolite to granulite facies in which the khondalite and amphibolite underwent anatexis during continental collision with crustal thickning followed by tectonic exgumation to generate the Água Rasa metagranite of the external part of the anomalies at 2077 ± 24 Ma.

The post-collision decompressional stage due to orogen collapse triggered hydrothermal processes with percolation of C-O-H fluids, leading to the graphite recrystallization around 611 ºC. The decompression process sustained generating the Água Rasa metagranite between 1941±23 Ma (monazite U-Th-Pb_T) and 1934±74 Ma (zircon U-Pb). This process is also recorded in the khondalite at 1937 ± 32 Ma (monazite U-Th-Pb_T) from the resetting of the monazite U-Th-Pb system during the orogenic collapse.

The extension of the Cláudio Shear Zone towards the Itapecerica region could be a suggestive geological setting of the investigated region (Figure 3) where a possible suture zone in the Itapecerica/Claudio region was formed by the collision between Divinópolis and Campo Belo/Bonfim complexes during the Rhyacian-Orosirian orogeny, involving the Itapecerica Basin in an oceanic setting alongside and forward to Minas Basin.

Similarities between the khondalite rocks of this study and of the North China suggest that the São Francisco-Congo Craton was near the North China Craton in the supercontinent Columbia for the 2.1–1.9 Ga period.

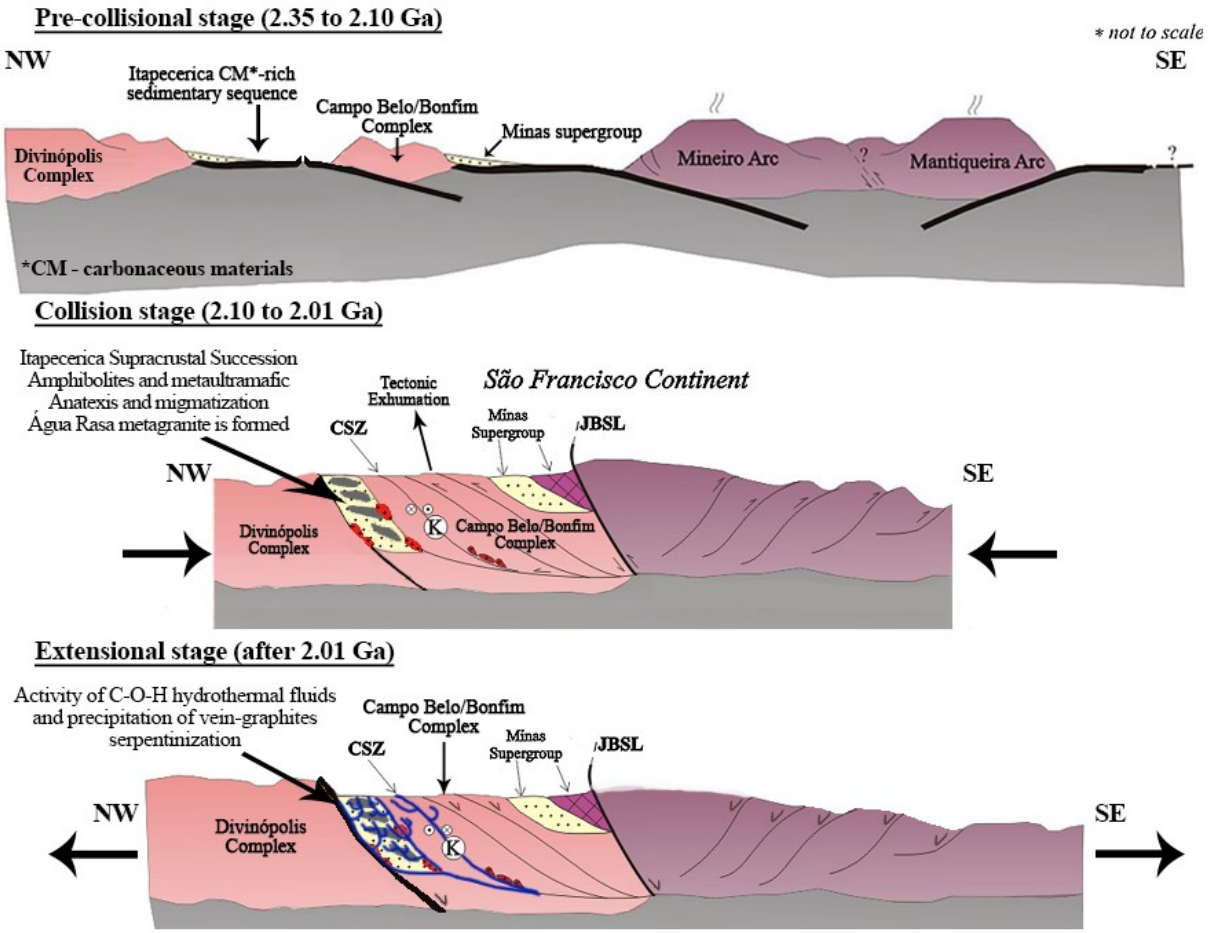

Figure 3. Tectonic model (adapted from Carvalho et al. 2017; Coelho and Chaves 2019) for the formation of the Itapecerica Supracrustal Succession and Água Rasa metagranite by the collision between Divinópolis and Campo Belo/Bonfim complexes during the Rhyacian-Orosirian orogeny. (K) Kinawa migmatite. (CSZ) Claudio Shear Zone. (JBSL) Jeceaba-Bom Sucesso lineament.

REFERENCES

Aguilar, C., Alkmim, F.F., Lana, C., Farina, F., 2017. Palaeoproterozoic assembly of the São Francisco craton, SE Brazil: new insights from U–Pb titanite and monazite dating. Precambrian Res., v. 289, p. 95-115.

Ávila, C.A., Teixeira, W., Bongiolo, E.M., Dussin, I.A., Vieira, T.A.T., 2014, Rhyacian evolution of subvolcanic and metasedimentary rocks of the southern segment of the Mineiro belt, São Francisco Craton, Brazil. Precambrian Res., v. 243, p. 221-251.

Campello, M.S., Vaz, B.B., Oliveira, M.A.S., Ávila, M.A.C., 2015. Relatório e mapa geológicos 1:100.000 da Folha Formiga SF.23-V-B-III. Projeto Fortaleza de Minas, CODEMIG/UFMG. A.C. Pedrosa Soares (coord.). 62 p.

Carneiro, M.A., Nalini Júnior, H.A., Endo, I., Suita, M.T.F., Castro, P.T.A., Barbosa, M.S.C., Campos, J.C.S., Goulart, L.E.A., Silva, E.F.S., Pereira, A.A., Tavares, T.D., Jiamelaro, F., Carneiro, J.M., Mariano, L.C., Miguel, F.P., Silva Junior, A.C., Barbosa, A.S., Prado, G.E.A., Santos, C., Urbano, E.E.M.C., 2007, Folha Campo Belo- SF.23-V-B-VI, escala 1:100.000: nota explicativa integrada com Oliveira. UFOP/CPRM, Minas Gerais, 114 p.

Carvalho, B.B., Janasi, V.A., Sawyer, E.W., 2017. Evidence for Paleoproterozoic anatexis and crustal reworking of Archean crust in the São Francisco Craton, Brazil: a dating and isotopic study of the Kinawa migmatite. Precambrian Res., v. 291, p. 98-118.

Chaves, A.O., Campello, M.S., Soares, A.C.P., 2015, Idade U-Th-Pb_T de monazitas do sillimanita-cordierita-granada-biotita gnaisse de Itapecerica (MG) e a atuação da orogenia Riaciano-Orosiriana no interior do Cráton São Francisco Meridional. Geociências, v. 34, n. 3, p. 324-334.

Farina, F., Albert, C., Lana, C., 2015. The neoarchean transition between medium-and high-K granitoids: clues from the southern São Francisco craton (Brazil). Precambrian Res., v. 266, p. 375-394.

Fernandes, R.A., Carneiro, M.A.O., 2000. Complexo Metamórfico Campo Belo (Craton São Francisco Meridional): unidades litodêmicas e evolução tectônica. Revista Brasileira de Geociencias, v.30, n. 4, p. 671-678.

LASA ENGENHARIA E PROSPECÇÕES S.A. Relatório final do levantamento e processamento dos dados magnetométricos e gamaespectrométricos. Levantamento Aerogeofísico de Minas Gerais, Área 2. Projeto Pitangui – São João Del Rey – Ipatinga. 2001.

Miranda, D.A., Chaves, A.O., Dussin, I.A., Porcher, C.C., 2020. Paleoproterozoic khondalites in Brazil: a case study of metamorphism and anatexis in khondalites from Itapecerica supracrustal succession of the southern São Francisco Craton. International Geology Review, doi:10.1080/00206814.2020.1716273.

Moreira, H., Seixas, L., Storey, C., Fowler, M., Lasalle, S., Stevenson, R., Lana, C., 2018. Evolution of siderian juvenile crust to rhyacian high Ba-Sr magmatism in the Mineiro belt, southern São Francisco craton. Geoscience Frontiers, v. 9, p. 977-995.

Noce, C.M., Machado, N., Teixeira, W., 1998. U-Pb Geochronology of gneisses and granitoids in the Quadrilatero Ferrıfero (Southern São Francisco Craton): age constraints for Archean and Paleoproterozoic magmatism and metamorphism. Revista Brasileira de Geociencias, v. 28, p. 95-102.

Noce, C.M., Pedrosa-Soares, A.C., Silva, L.C., Armstrong, R., Piuzana, D., 2007. Evolution of polycyclic basement in the Araçuaí Orogen based on U-Pb SHRIMP data: implications for the Brazil-Africa links in the Paleoproterozoic time. Precambrian Res., v. 159, p. 60-78.

Oliveira, A.H., 2004, Evolução tectônica de um fragmento do Cráton São Francisco Meridional com base em aspectos estruturais, geoquímicos (rocha total) e geocronológicos (Rb-Sr, Sm-Nd, Ar-Ar, U-Pb). Tese de Doutoramento. Universidade Federal de Ouro Preto, Brazil, 92p.

Romano, R., Lana, C., Alkmim, F.F., Stevens, G., Armstrong, R., 2013. Stabilization of the southern portion of the São Francisco craton, SE Brazil, through a long-lived period of potassic magmatism. Precambrian Res., v. 224, p. 143-159.

Ruy, A.C., Silva, A.M., Toledo, C.L.B., Souza Filho, C.R., 2006. Uso de dados aerogeofísicos de alta densidade para mapeamento geológico em terrenos altamente intemperizados: o estudo de caso da região de Cláudio, porção sul do Cráton São Francisco. Revista Brasileira de Geofísica, v. 24, n. 4, p. 535-546.

Teixeira, W., Ávila, C.A., Dussin, I.A., Neto, A.C., Bongiolo, E.M., Santos, J.O., Barbosa, N.S., 2015. A juvenile accretion episode (2.35–2.32 Ga) in the Mineiro belt and its role to the Minas accretionary orogeny: zircon U-Pb-Hf and geochemical evidences. Precambr. Res., v. 256, p. 148-169.

Teixeira, W., Oliveira, E.P., Peng, P., Dantas, E.L., Hollanda, M.H.B.M., 2017. U-Pb geochronology of the 2.0 Ga Itapecerica graphite-rich supracrustal succession in the São Francisco Craton: Tectonic matches with the North China Craton and paleogeographic inferences. Precambrian Research, v. 293, p. 91-111.

Zacchi, E.N.P., Silva, A.M., Toledo, C.L.B., Souza Filho, C.R., 2007. As três anomalias elípticas da porção sul do Cráton São Francisco: novos alvos para a mineralização de grafita? Revista Brasileira de Geofísica, v. 25, n. 4, p. 421-431.